POLITECNICO
MILANO 1863

SCUOLA DI INGEGNERIA INDUSTRIALE
E DELL'INFORMAZIONE

EXECUTIVE SUMMARY OF THE THESIS

Catalytic partial oxidation and Steam reforming of methane and ethanol on Rh catalysts: Effect of the support

TESI MAGISTRALE IN ENERGY ENGINEERING – INGEGNERIA ENERGETICA

AUTHOR: FILIPPO LANCINI

ADVISORS: ALESSANDRA BERETTA; GIANPIERO GROPPI.

CO-ADVISORS: ABDELRAHMAN MOSTAFA; VERONICA PIAZZA.

ACADEMIC YEAR: 2020-2021

1. Introduction

The need to solve the future energy demand requested by our society, taking the environmental impact into consideration, is one of the critical issues that needs to be solved. The ideal scenario from the future is represented by the possibility of achieving a green energy production, based on the exploitation of renewable sources. However, before reaching this ideal future, a transition phase is needed, in which renewable sources and fossil fuels systems can be coupled. For this reason, the priority is to focus on the development of existing technologies to increase their efficiency and decrease their emissions. From a point of view of carbon emissions from fossil fuels, bio-refineries play an important role. The production of some type of biofuels, however, requires the exploitation of large quantities of hydrogen. Hydrogen is becoming more relevant also as an energy carrier, both for mobile and stationary applications. Thanks to its environmentally friendly nature, to its large number on ways to be produced, and to its possibility to be directly converted in different types of energy, it can be exploited for a variety of applications. For example, it can be used as a fuel in industrial sector or blended with other fuels for the energy production. In the domestic sector can be used as a fuel for heating or as a fuel cell supply to produce domestic power. Our interest is on the small-scale distributed application (on-board hydrogen and fuel processes for hydrogen uses). In this context, one attractive option is to supply auxiliary power to vehicles from fuel cells fed from syngas produced on-board through catalytic partial oxidation. Regarding the fuel choice, the ethanol seems to be promising, also as a substitute of the fossil-based fuels, due to its properties (easy storing and handling, low toxicity, and volatility) and due to the growing market of bioethanol.

2. Objective of the study

In this thesis, the catalytic partial oxidation of methane and ethanol have been studied for small scale applications. The main goal of this study was to investigate the effect of the catalyst supports on these processes. This thesis work can be divided

into two main parts. Firstly, the small scale H_2 production was studied experimentally in the lab scale adiabatic reactor using ceramic monolith coated with Rh/α-Al_2O_3-La wash-coat. In this plant, the gas and solid phases temperatures have been measured along the axis of the reactor along with the axial concentration profiles in situ using the spatially resolved sampling technique. The results of these tests were compared with tests performed in previous studies using monoliths coated with Rh/α-Al_2O_3 and Rh/$MgAl_2O_4$. Furthermore, the catalyst stability and their tendency towards coke formation were studied to evaluate the most suitable catalyst formulation for the commercial applications.

Based on the results obtained in the adiabatic reactor, in the second part of this study Rh/$MgAl_2O_4$ was selected for a dedicated kinetic study of CPO and SR of methane and Ethanol. Experiments were performed on an annular isothermal reactor, a suitable setup to study the reactions kinetics, and the results were compared with the kinetic model developed previously for Rh/α-Al_2O_3 catalyst. Finally, an experiment was performed on both Rh/α-Al_2O_3 and Rh/$MgAl_2O_4$ to evaluate the role of the support on coke formation. Both catalysts were subjected to ageing under the same conditions for the same time on stream and temperature programmed oxidation (TPO) was performed on the aged catalysts

3. Procedure

During this thesis work, two types of catalyst were prepared: Rh/α-Al_2O_3-La and Rh/Mg-Al_2O_4. They were made by impregnating the powder of both supports with a rhodium nitrate solution, which is the precursor of the active phase. A slurry was then prepared from these catalytic powders and was used to coat ceramic monolith or tubes, depending on the experimental campaign in which it has to be used. For the autothermal tests, ceramic monoliths were coated using the percolate-spin-coating technique, where the slurry was poured on the monolith and the excess one was eliminated by rotating the monolith using the spin-coating machine. Liquid fuels are fed using a peristaltic pump and an evaporator. The adiabatic reactor is schematically represented in Figure 1. Herein the catalyst is placed between inert monoliths, to ensure a proper mixing and approach to adiabaticity. The autothermal reactor is equipped with the spatially resolved sampling technique. The axial profiles of the reactor were collected under real working conditions via the spatially resolved sampling technique; a capillary tube was inserted inside the reactor carrying a thermocouple to measure the gas phase temperature, or an optical fiber connected to a pyrometer, to collect the solid phase temperature of the reactor. the collection of concentration profiles was done using a capillary tube with an open end to collect localized samples along the axis of the reactor, that can be sent to the gas chromatograph to evaluate the concentrations of the different components in the reactors.

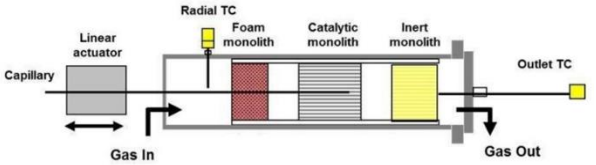

Figure 1: Reactor configuration

The catalyst deactivation was monitored by means of the standard methane CPO test..

The tubes instead were tested in the isothermal microreactor (Figure 2). The liquid fuels in this case were fed in the system as vapor, using a saturator, while for the water co-feed, a small packed-bed reactor containing a platinum-based catalyst is used. For the temperature measurement, two K-type thermocouples are made to slide inside the alumina tube place next to the reactor and inside the oven environment, to measure temperature profiles along the axial axis of catalytic bed and the corresponding internal oven environment.

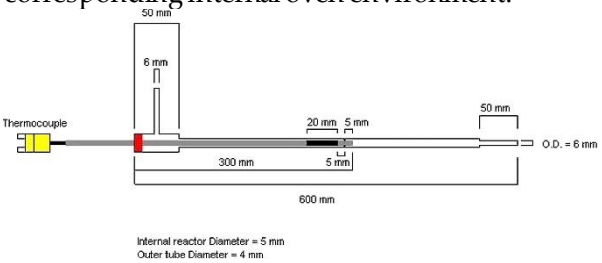

Figure 2: Sketch of the annular reactor[1]

The concentration measurements are obtained using a micro gas chromatograph.

4. Tests in adiabatic conditions

A commercial mixed-oxide support, based on La-promoted alumina with 2% wt. Rh., was used to study the effect of the support on the stability and performance of the reactor.

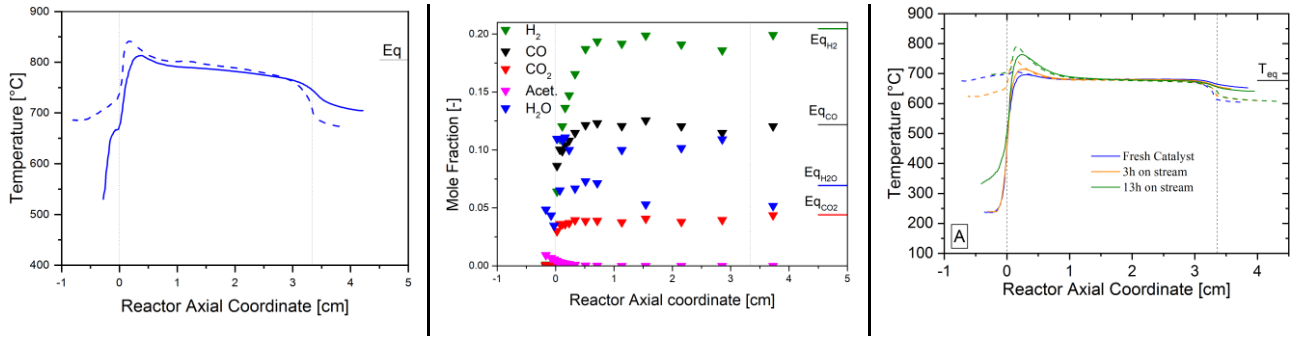

(a) (b) (c)

Figure 3: a) Temperature profile for EtOH CPO; b) Concentration profiles of the major species for EtOH CPO; c) growth of the hotspot in CH_4 CPO temperature tests

The catalyst was tested in CPO conditions with methane and ethanol. Temperature and concentration profiles were collected for the La-doped-alumina catalyst using the spatially resolved sampling technique (Figure 3a and Figure 3b). The productivity of the syngas is completely analogue to the one resulted in the past using different supports (Mg-aluminate and α-alumina). The same can be said for the temperature profiles, where the support has a minor effect on the temperature profiles and on the thermal behavior of the reactor, with comparable intensity of the hotspot. However, monitoring over time and periodically repeating CPO CH_4 tests (which is particularly sensitive to the loss of superficial activity). We observed a progressive growth in the hotspot at the entrance (Figure 3c), index of a loss of activity in the reforming. So, La-alumina, in the same way of α-alumina, give rise to the formation of species during the CPO with EtOH, responsible for the progressive deactivation (such as ethylene). This was not observed with the Mg-aluminate, and moreover, comparing the ethylene production, the one of Mg-aluminate was much lower compared to the one of the other two supports. This can be due to the use of a less acidic support that limits the formation of those species. To support this hypothesis, the results of temperature programmed oxidations performed on aged catalysts, highlight that for the Mg-aluminate support the CO_2 released was lowest between the three supports, index of a lower quantity of carbon deposits on the surface of the catalyst.

5. Kinetic investigation on Rh/MgAl2O4 in isothermal conditions

Once identified the Rh/MgAl2O4 as the most suitable formulation for the CPO of ethanol in adiabatic conditions, we have addressed a deeper kinetic investigation of the catalytic process by using a microreactor with annular configuration, where isothermal tests can be performed.

The role of the active phase has been discussed, performing experiments of methane and ethanol CPO and SR on a Rh/Mg-Al_2O_4 catalyst.

In particular, CPO of methane tests have been performed varying the space velocity and the oxygen to carbon ratio. In order to highlight some differences caused by the different support, the results have been compared, in a qualitative way, with results obtained with Rh/Al_2O_3 catalysts[3]. In both cases, the decrease of the space velocity is found to be effective for initiating the process at lower temperature. A higher space velocity, and thus a lower residence time, cause a lower conversion of the fuel. Considering the effect of the support, the Rh/Al_2O_3 catalysts shows a stronger effect of the space velocity on the water and CO_2 distribution, while it has a lower effect on the oxygen conversion, compared to the Mg-aluminate case. However, the conversions and products distribution in the low space velocity case, using Rh/Mg-Al_2O_4, are very close to the equilibrium lines. In order to make a more precise evaluation, the experimental results regarding the effect of the space velocity over a Rh/Mg-aluminate support have been compared to the prediction of a kinetic model [1][3][4][5]. This model was developed in previous works, for CPO and SR of methane and ethanol for annular reactor.

In the case of low space velocity, the model simulations are very close to the experimental data, with some small differences in the case of water and CO_2. In the case of high space velocity, some differences show up at high temperatures. For example, the methane conversion that from the model simulation should be a complete conversion, in the experiments results to be around 90. This is the region where mass transfer resistance can assume a role and influence the reactivity. Regarding the oxygen to carbon ratio, it doesn't influence much the methane conversion at low temperatures. Its reduction (maintaining constant the methane feed concentration) affects the production of CO and H_2, because the high concentration of oxygen favors the combustion by increasing selectivity toward water and CO_2, while decreasing the one of hydrogen and carbon monoxide. The SR of methane didn't show any significant effect caused by the different support, except a shift in the CO_2 distribution.

The experimental campaign with methane has substantially confirmed that no significant change on the reaction was associated to the nature of the support.

However, the experiments in the adiabatic reactor reveal that EtOH CPO is a more critical process, and the reactor performance depends not only on the rate of major reaction involved in the conversion of ethanol and oxygen, but also on the extent of secondary reactions responsible for the formation of C-surface species which can negative affect the stable operation. For this reason, the investigation was extended to EtOH CPO and SR on the isothermal reactor. The qualitative comparison of CPO of EtOH the two supports, shows a higher conversion of EtOH with Mg-aluminate (Figure 4), together with higher concentration of syngas and lower of water and carbon dioxide. The acetaldehyde, in the case of Mg-aluminate, presents a second peak at around 500 °C. SR experiments with ethanol have been performed, showing that apparently the Mg-aluminate, in the 350 to 600 °C range, produces more acetaldehyde, consistently with the dehydrogenation contribution observed also in the CPO test in the same range of temperatures. A production of ethylene is shown, as a product of ethanol dehydration, and similarly to what we have seen in the adiabatic reactor, the $Rh/Mg\text{-}Al_2O_4$ catalyst gave rise to less ethylene formation. It can be observed a substantially satisfactory comparison with the model. It is however observed that the simulation, thus the performance of the Rh/Al_2O_4 catalyst, reflect a steeper temperature dependence. In fact, the model tends to underestimate the conversion below 600 °C and overestimate the observed conversion at higher temperatures.

Temperature programmed oxidations were performed after selected ageing over the Mg-aluminate supported catalyst, and then the results have been compared to the ones of alumina. Mg-aluminate reports only 1 predominant species, with a peak at 300 °C, that is reactive. Instead, in the alumina case, multiple peaks can be distinguished, a pair with peaks between 200 and 300 °C, representing the most reactive species, and

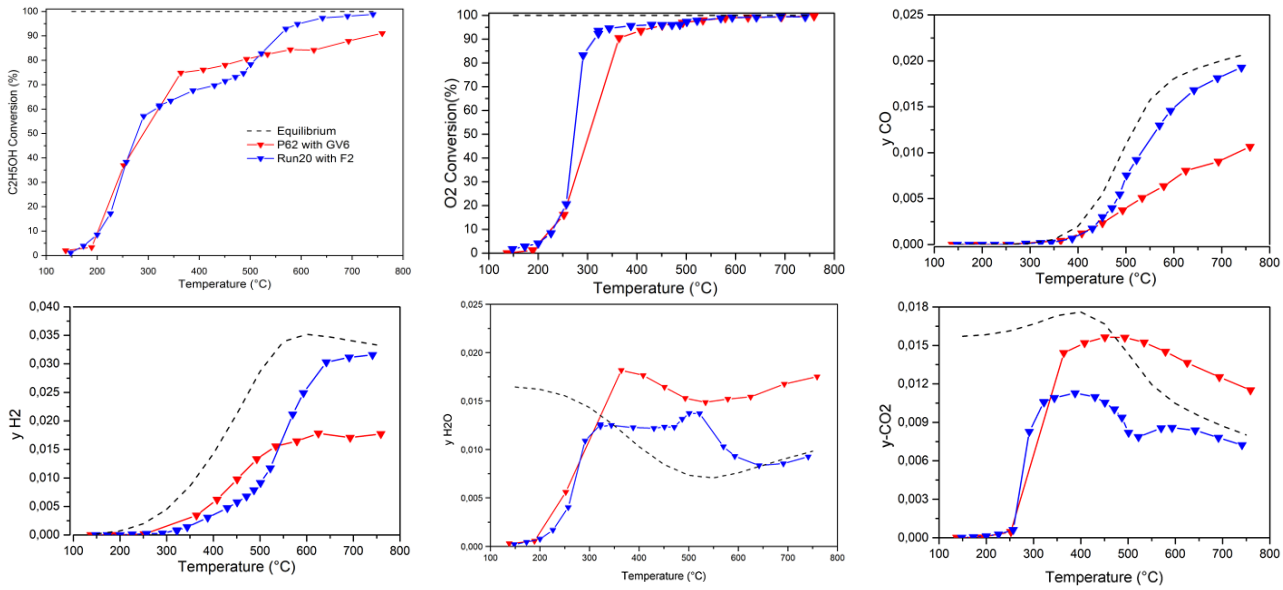

Figure 4: Comparison between the concentration profiles of a α-alumina catalyst (red lines) and a Mg-aluminate catalyst (blue lines) for the CPO of EtOH

another pair with peaks around 400 and 500 °C, less reactive.

6. Conclusions

Rh/α-Al_2O_3 has been identified in the literature and from our studies as a reference formulation for the autothermal conversion of light hydrocarbons to H_2/CO mixtures. The conversion of C_1-C_3 hydrocarbon fuels into syngas is a very fast process that approaches thermodynamic equilibrium at few milliseconds contact times; the operation of the autothermal reactor is stable and not hindered by coking phenomena. The use of oxygenates fuels, instead, gives rise to a more complex product distribution and the formation of coke precursor, such as ethylene and acetaldehyde, cannot be avoided and negatively affect the stable operation of the reactor. In this thesis work different commercial supports are used in performance and kinetic investigations. Results from experiments performed in an adiabatic reactor highlight how the studied supports have a minor effect on the performance, especially on the syngas production. However, the support influences the production of species that negatively affect the performance of the reactor. The one that shows a lower tendency to form those species is the Mg-aluminate. From this result, a deeper kinetic investigation of Mg-aluminate catalysts was addressed on an annular microreactor. Here, CPO and SR of ethanol and methane were investigated, varying the conditions of the experiment. The experimental campaign has been compared qualitatively with the results of analogue investigations having α-alumina as reference. Besides, a more quantitative comparison between the two supports was obtained by comparing the present results with prediction of a model developed to describe the processes on Rh/Al_2O_3. No major differences were found, especially when looking at the major reactions (oxidations and steam reforming). However, the kinetic investigation in the microreactor confirmed the lower tendency of Mg-aluminate to strongly adsorb ethanol and to promote the formation of surface C species. The causes of this behavior can be the morphological properties (Mg-Al_2O_3 has a higher surface area and a higher dispersion) and the lower acidity of Mg-, that apparently are the favorable features that provide superior performance to this support, especially the control of coking phenomena.

7. References

[1] A. Donazzi, A. Beretta, G. Groppi, and P. Forzatti, "Catalytic partial oxidation of methane over a 4% Rh/α-Al2O3 catalyst: Part I: Kinetic study in annular reactor," *J. Catal.*, vol. 255, no. 2, pp. 241–258, Apr. 2008, doi: 10.1016/J.JCAT.2008.02.009.

[2] M. Bressan, "Catalytic partial oxidation of ethanol on Rh coated monoliths: advanced catalyst formulation and coating techniques," 2021.

[3] A. G. Bayram and V. Piazza, "Syngas Production from Ethanol and Formic Acid over Rh / Al 2 O 3 : a Kinetic Study in Annular Reactor," 2019, [Online]. Available: https://www.politesi.polimi.it/bitstream/10589/150149/3/2019_10_Bayram_Piazza.pdf.

[4] D. Pagani, "Catalytic Partial Oxidation of light and liquid hydrocarbons: experimental and kinetic study on Rh based catalyst."

[5] A. Beretta, P. Baiardi, D. Prina, and P. Forzatti, "Analysis of a catalytic annular reactor for very short contact times," *Chem. Eng. Sci.*, vol. 54, no. 6, pp. 765–773, 1999, doi: 10.1016/S0009-2509(98)00261-9.

8. Acknowledgements

First, I would like to thank Professors Alessandra Beretta and Gianpiero Groppi for the opportunity to work on this project and for the help received during this period. I would also like to thank my co-supervisors, Abdelrahman Mostafa and Veronica Piazza, for the support and the patience they showed me. Finally, I would say thanks to all the people who share time with me during this period, such as Alessandro, Andrea, Angelo, Maria, Matteo, Michele, Michela, Paolo, Vittoria, and Yi.

POLITECNICO
MILANO 1863

SCUOLA DI INGEGNERIA INDUSTRIALE
E DELL'INFORMAZIONE

Catalytic partial oxidation and Steam Reforming of methane and ethanol on Rh catalysts: Effect of the support

TESI DI LAUREA MAGISTRALE IN
INGEGNERIA ENERGETICA

Author: **Filippo Lancini**

Student ID:	952941
Advisors:	Prof. Alessandra Beretta
	Prof. Gianpiero Groppi
Co-advisor:	Eng. Abdelrahman Mostafa
	Eng. Veronica Piazza
Academic Year:	2020-2021

Abstract

The catalytic partial oxidation (CPO), along with steam reforming (SR), is one of the most important processes to produce hydrogen from fossil and renewable sources. As the CPO is proven to be suitable for small scale hydrogen production and due to its flexibility towards the feedstock, it is expected to play a key role for reaching the European goals in the energy transition. In this work, the CPO of methane and ethanol on Rh based catalysts was studied, investigating the effect of the catalyst support on the performance of the process both in the terms of syngas production and the catalyst stability. The study was divided into two parts. Firstly, the small scale H_2 production was studied experimentally in the lab scale adiabatic reactor using ceramic monolith coated with Rh/α-Al_2O_3-La wash-coat. In this plant, the gas and solid phases temperatures have been measured along the axis of the reactor along with the axial concentration profiles in situ using the spatially resolved sampling technique. The results of these tests were compared with tests performed in previous studies using monoliths coated with Rh/α-Al_2O_3 and Rh/$MgAl_2O_4$. Furthermore, the catalyst stability and their tendency towards coke formation were studied to evaluate the most suitable catalyst formulation for the commercial applications. Results show that Rh/$MgAl_2O_4$ catalysts has superior performance in terms of stability, being the least prone to deactivation both by sintering and coke formation. Based on these results, in the second part of this study Rh/$MgAl_2O_4$ was selected for a dedicated kinetic study of CPO and SR of methane and Ethanol. Experiments were performed on an annular isothermal reactor, a suitable setup to study the reactions kinetics, and the results were compared with the kinetic model developed previously for Rh/α-Al_2O_3 catalyst. This comparison showed that the catalyst support has negligible effect on the kinetic parameters of both methane and ethanol CPO. Finally, an experiment was performed on both Rh/α-Al_2O_3 and Rh/$MgAl_2O_4$ to evaluate the role of the support on coke formation. Both catalysts were subjected to ageing under the same CPO of EtOH conditions ($yEtOH$ = 1.5%, yO_2 = 1.68%, GHSV = 1500000 NL/h/kg) for 2 hours, and temperature programmed oxidation was performed on the aged catalysts. Results of this investigation showed that the $MgAl_2O_4$ supported catalyst trapped more reactive C-species on the surface which may explain its lower tendency to deactivation by coking.

Key-words: Catalytic partial oxidation; Steam reforming; Syngas; Ethanol; Methane.

Abstract in lingua italiana

L'ossidazione parziale catalitica (CPO), insieme allo steam reforming (SR), è uno dei processi più importanti per la produzione di idrogeno a partire da fonti fossili e rinnovabili. La CPO risulta essere adatta alla produzione su piccola scala di idrogeno, e grazie alla sua flessibilità sulla miscela reagente, ricopre un ruolo chiave nel raggiungimento degli obiettivi prefissati in Europa sulla transizione energetica. In questo In questo lavoro la CPO è stata studiata usando come combustibili metano ed etanolo, su catalizzatori a base di rodio, indagando l'effetto del supporto sulle prestazioni del processo, sia in termine di produzione di syngas e di stabilità del catalizzatore. Il lavoro è stato diviso in due parti. Inizialmente la produzione di idrogeno su piccola scala è stata studiata sperimentalmente nel reattore adiabatico in scala di laboratorio, usando monoliti ceramici ricoperti con un washcoat di Rh/α-Al_2O_3-La. In questo impianto le temperature della fase solida e gassosa sono state misurate lungo l'asse del reattore, insieme ai profili di composizione assiale usando una misurazione in situ usando un capillare. I risultati di questi test sono stati comparati con test svolti durante precedenti studi usando Rh/α-Al_2O_3 e Rh/$MgAl_2O_4$. Inoltre, sono state studiate la stabilità dei catalizzatori e la loro tendenza alla formazione di depositi carboniosi, in modo da trovare la formulazione più adatta per applicazioni commerciali. I risultati hanno mostrato che il catalizzatore con Rh/$MgAl_2O_4$ ha prestazioni migliori per quanto riguarda la stabilità, essendo meno propenso a disattivarsi per colpa dei depositi carboniosi e del sintering. Basandosi su questi risultati, nella seconda parte del lavoro, il Rh/$MgAl_2O_4$ è stato selezionato per uno studio cinetico della CPO e dello SR di metano ed etanolo. Gli esperimenti sono statis volti su un reattore anulare isotermo, adatto allo studio delle cinetiche di reazioni, e i risultati sono stati confrontati con un modello cinetico sviluppato precedentemente per i catalizzatori con Rh/α-Al_2O_3. Questo confront ha mostrato che il support ha un effetto trascurabile sui parametri cinetici della CPO, sia per il metano che per l'etanolo. Infine, un esperimento è stato svolto sia su Rh/α-Al_2O_3 e Rh/$MgAl_2O_4$, per valutare il ruolo del supporto sulla formazione di depositi carboniosi. Entrambi i catalizzatori sono stati sottoposti a prove di invecchiamento nelle condizioni di CPO di etanolo ($yEtOH$ = 1.5%, yO_2 = 1.68%, GHSV = 1500000 NL/h/kg) per due ore, e in seguito a una ossidazione a temperature programmata. I risultati di questo studio hanno mostrato che il catalizzatore supportato con $MgAl_2O_4$ specie a base di carbonio più reattive sulla sua superficie, che possono spiegare la sua minore tendenza alla disattivazione.

Parole chiave: Ossidazione parziale catalitica; Steam reforming; Gas di sintesi; Etanolo; Metano.

Contents

Introduction

One of the critical issues of this period is to satisfy the future energy demand by our society, taking into considerations the environmental aspects, such as greenhouse gasses and pollutant emissions. The ideal scenario for the future is represented by the possibility of achieving a green energy production, based completely on the exploitation of renewable sources. However before reaching this ideal future, a transition phase is needed, in which the renewable production can be coupled with traditional systems, based on fossil fuels. For this reason, the priority at the moment is to focus on the development of existing technologies to increase their efficiency and decrease their emissions, especially in the mid-short term. One of the first process to focus is the production of hydrogen which is largely used, for example, in chemical refinery. Recently, the role of hydrogen also as energy carrier is becoming more relevant, both for mobile and stationary applications. The hydrogen, thanks to its environmentally friendly nature, to the large number of ways in which can be produced, and to its possibility to be directly converted in thermal, mechanical or electrical energy, can be exploited for a wide variety of applications. For example, it can be used as fuel in industrial sector or blended with other fuels for the energy production. Also, in the domestic sector, it can be used as a fuel for heating or as a fuel cell supply to produce domestic power. Our interest is on the small-scale distributed application, for example on-board H_2 and fuel processing for hydrogen uses. In this context, one of the most attractive options is to supply auxiliary power to vehicles from fuel cells, fed from syngas produced on-board by means of the catalytic partial oxidation (CPO). Focusing on environmental problems, the use of biofuels such as methane and ethanol can contribute to the decrease of greenhouse gas emissions. Ethanol has been chosen as an alternative fuel, due to its properties (easy storing and handling, low toxicity, and volatility) and due to the growing market of bioethanol. To enhance the CPO reaction and its selectivity towards syngas, catalysts are necessary. In this context, the objective of this thesis is the study of the performance of catalysts obtained from different commercial supports. In particular, the performance and the stability of the catalyst have been tested in an autothermal adiabatic reactor which simulates the final process. Then, studies on the coking tendency and on the kinetics of the reactions have been conducted on an isothermal annular microreactor. Three

commercial supports have been considered in this thesis: Mg-aluminate, α-alumina and La-doped-alumina, which have been applied to different ceramic structure, such as monoliths and tubes, depending on which rig has been used.

This report is divided in four chapters. The first chapter studies the state-of-the-art technology of the process and reviews the most relevant research papers published and previous experimental activities performed by the laboratory of catalysis and catalytic processes (LCCP) at Politecnico di Milano.

The second chapter describes the experimental set-up and methods, with a section dedicated to the description of the preparation of catalysts and one dedicated to the description of a kinetic model for CPO and SR of ethanol and methane. It illustrates the rig layout of two different plants, one adiabatic lab scale rig for process demonstration/investigation and one isothermal lab scale rig for fundamental kinetic investigation . This chapter focus on the description of the characteristics of the components of each rig, together with the description of the procedures followed during the experiments. Regarding the first rig, a detailed description of the temperature and concentration profiles sampling technique is presented. In the section regarding the catalyst preparation, all the steps of the preparation are described.

Chapter three reports the experimental results obtained in the adiabatic rig, including the startup procedure of the catalytic partial oxidation and the obtained temperature and concentration profiles for the different conditions. Each temperature and concentration profile has been compared to the one obtained in previous thesis work, to study the effect of the support on the reaction and considering also the effect on the stability. At the end of the chapter, the results of temperature programmed oxidation on the spent catalyst are discussed, focusing on the quantity of carbon deposits on the surface of the catalyst and comparing it to other catalysts previously studied and with the same experimental history.

In chapter four the kinetic investigation with methane and ethanol in an isothermal microreactor are presented and analyzed. This chapter reports both experimental and modelling results, exploring different conditions (variation of space velocity, oxygen to carbon ratio). At the end of the chapter, a study of the carbon deposits is performed. Each experiment performed in this chapter has been compared with results obtained in previous thesis works with a different support. At the end of the experimental campaign, a fresh catalyst has been subjected to ageing and temperature programmed oxidation to investigate the coke formation on its surface after a certain stream time at a certain temperature.

1. State of the art

1.1 Importance of the synthesis gas and hydrogen

Synthesis gas or syngas is a term that represents mixtures of carbon mono-oxide and hydrogen in various ratios depending on the feedstock and on the process used to produce it.

These mixtures can be used both as a source of carbon mono-oxide and hydrogen and as a feedstock for downstream processes[1]. It has a lot of application as shown in Figure 1.1: can be used for many chemicals production (ammonia, aldehydes, methanol and higher alcohols) or as a source of hydrogen in the refinery or as an energy carrier.

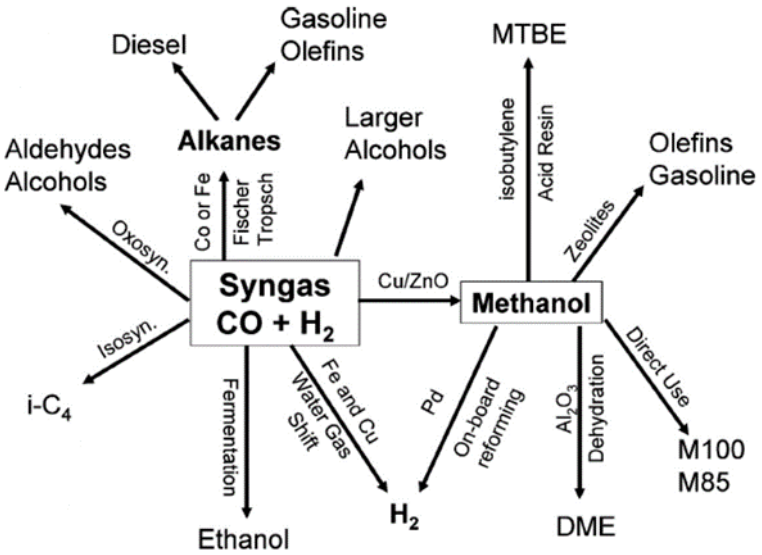

Figure 1.1: Syngas applications in refinery, in chemical process industry and in fuel production

The production of syngas can occur through different processes and raw materials (from natural gas to coal). The choice of the material depends on the downstream use of the syngas and on the cost and on the availability of the feedstock [1].

With the energy consumption that is always increasing, considering also the more and stricter environmental regulation, a higher level of fuel processing is required. This

will lead to a higher consumption of hydrogen in the refinery to increase the quality of the final products (hydro-treating and hydro-desulfurization)[2]. We can see the forecast of this higher hydrogen consumption from Figure 1.2, where it is represented the global hydrogen demand by sector in the Net Zero Scenario presented in the IEA Energy outlook (2020-2030)[3].

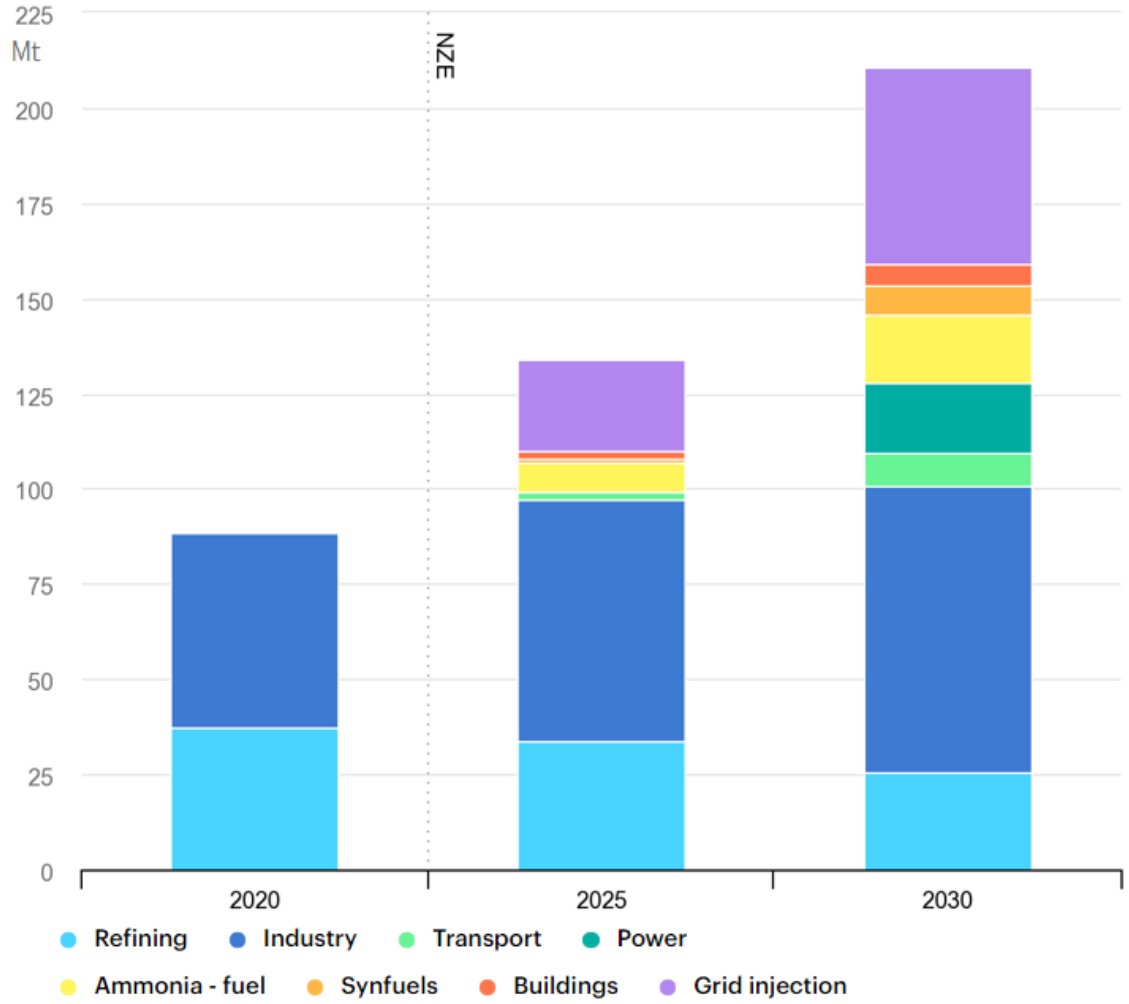

Figure 1.2: Global hydrogen demand by sector in the Net Zero Scenario, 2020-2030

From the point of view of the carbon emission reduction, bio-refineries play an important role. Their products, such as green diesel, requires a large amount of hydrogen to transform vegetable oils into paraffinic hydrocarbons with a carbon content in the gasoil range [4]. Additionally, hydrogen will play an important role as energy carrier both for small scale stationary applications and mobile applications facing the challenge of the local on demand delivery of H_2 for such applications. Hydrogen distribution and storage is very inconvenient compared to the fossil fuels one, especially in gaseous and liquid form. The storage of hydrogen in liquid form requires low temperature (20 K) and the cooling process requires time and energy.

Storage of gaseous is limited due to the large volumes required even at high pressure, due to the hydrogen low density, and this results into a high cost for the materials.

An interesting and feasible way to store the hydrogen is the use of metal hydride, using the intermetallic phase of various metals that can absorb and hold large amounts of hydrogen by chemical bonding. However, this solution is still in R&D phase [5] and requires years for development before reaching the point of commercialization.

In this respect, the distributed and on-board hydrogen production has gained attention for conversion of hydrogen into electric energy through fuel cells [6][5], to cover the expected demand of the transport and the power sectors of 25 Mt by 2030 as presented in Figure 1.2. The onboard presence of hydrogen serves a range of applications: electric power production through fuel cells, reduction of the catalytic after treatment systems, and direct injection in the internal combustion engine in the form of a mixture of the hydrogen produced on the vehicle with a conventional hydrocarbon fuel increasing the engine's efficiency. This procedure is called hydrogen enrichment and leads to an increase of pressure and combustion rate. Although, even if the pressure is higher, the overall power output is lower because the filling coefficient is lower due to the higher specific volume of hydrogen with respect to the one of gasoline and ethanol. Therefore, the quantity of air that can enter inside the combustion chamber is lower. This can be partially compensated thanks to the use of the turbocharger. All of this is associated with a lower BSFC (brake specific fuel consumption) and at the end a greater efficiency. Regarding the emissions, a decrease on the emission of CO and unburned hydrocarbons (HC) is observed, but there is a little increase in the NOx emitted due to the higher temperature reached. These advantages are possible thanks to the hydrogen properties such as its low ignition energy that makes combustion easier with the formation of stable and self-sustaining flame cores. Hydrogen has also a short quenching distance, that minimize the flame quenching near the combustion chamber walls, reducing heat losses, and has also a high auto-ignition temperature that contributes to knock resistance [6].

1.2 Production of synthesis gas

The large-scale production of green hydrogen can be obtained through different path. Among which water electrolysis, an energy intensive process in which the water splitting takes place, producing oxygen and hydrogen using electrical energy, has been gaining significant attention in recent years. However, due to the large amount of energy required, it is a viable path only if renewable electric energy can be supplied at low cost. An interesting route for the production of green hydrogen is presented through gasification and pyrolysis of biomass. However, the economically feasible gasification reactor requires a continuous and massive amount of feed to be supplied limiting this solution to certain geographical locations characterized by the availability of low-cost biomass. The strong consolidated supply chain of fossil-based hydrocarbons significantly reduces the cost of large-scale hydrogen production keeping it from the economic point of view the most suitable option. This requires great efforts on the development of green technologies with not only environmental benefit, but also economic advantage compared to the fossil-based processes.

Focusing on existing syngas production processes, the main commercial processes based on fossil hydrocarbons are [7]:

- Steam reforming (SR)

$$CH_4 + H_2O \rightarrow CO + 3H_2 \qquad \Delta H_r^0 = +206\ kJ/mol \tag{1.1}$$

The predominant process for the syngas production is the steam reforming of natural gas or light hydrocarbons up to naphtha.

Equation 1.1 shows the main chemical reaction involved in this process. This reaction is endothermic ($\Delta H > 0$) and so requires to be led at high temperature (>1000K) and it is necessary to supply heat from an external source. The reformate obtained from steam reforming has a high H_2/ CO ratio (near 3:1). Despite the high temperature, a catalyst is introduced in order to accelerate the reaction towards the products desired [1].

The presence of the catalyst makes necessary to purify the stream from sulfur and other compounds that can deactivate or poison the catalyst.
In Figure 1.3 a multi-tubular reactor is shown, in which the SR is performed to improve the heat transfer which is the real constriction of this process.

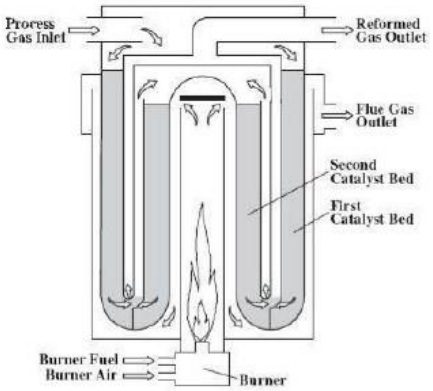

Figure 1.3: Steam reforming reactor

Nickel based catalysts are usually adopted in large scale reformers due to their low cost and good steam reforming kinetics. The catalyst is contained inside the tubes, placed inside a furnace that is heated from the fuel combustion. The conversion of methane is typically around 90-92%, with a syngas composition rich in hydrogen.

Nickel is not used in small scale reformers for safety reasons, due to the high exothermicity of Ni oxidation and it manages the formation of coke worse than noble metals. For these applications, rhodium is the best option because of its high specific activity. To minimize the coke formation could be helpful to introduce alkaline components such as potassium or magnesia [7][8]. Main issues related to this kind of process are high costs of material, high percentage of CO_2 in the products, and the high energy requirement.

- Non-catalytic partial oxidation (POX)

$$CH_4 + \frac{1}{2}\,O_2 \rightarrow CO + 2H_2 \qquad \Delta H_r^0 = -37\ kJ/mol \tag{1.2}$$

The formation of soot particulate is unavoidable due to the carbon content in hydrocarbon fuels, which will lead to the catalyst deactivation, and this represent the main issue of catalytic reforming processes. To challenge this soot formation, it can be useful the development of non-catalytic reforming processes. The equation 1.2 represents a non-catalytic partial oxidation which is a sub-stoichiometric combustion without the inclusion of a catalyst [9]. This process is slightly exothermic, so to guarantee a complete conversion and minimize soot and coke formation, it is necessary to reach a flame temperature of 1300 – 1500 °C inside the reactor. Here, the syngas obtained has a H_2/CO ratio of about 2:1 which makes it suitable for feeding hydrocarbons synthesis reactors such as Fischer-Tropsch. The non-catalytic partial oxidation is carried out at

pressures ranging from 30 to 100 bar, using pure oxygen as oxidizer, making the overall process costly and inadequate for small application [7].

- Auto-thermal reforming (ATR)

$$CH_4 + 2O_2 \rightarrow CO_2 + 2\,H_2O \qquad \Delta H_r^0 = -802\ kJ/mol \qquad (1.3)$$

$$CH_4 + \frac{3}{2}O_2 \rightarrow CO + 2\,H_2O \qquad \Delta H_r^0 = -520\ kJ/mol \qquad (1.4)$$

$$CH_4 + H_2O \rightarrow CO + 3\,H_2 \qquad \Delta H_r^0 = +206\ kJ/mol \qquad (1.5)$$

$$CO + H_2O \rightarrow CO_2 + H_2 \qquad \Delta H_r^0 = -41\ kJ/mol \qquad (1.6)$$

Auto-thermal reforming is a combination of partial and total oxidation with stream reforming reactions. The reactor (Figure 1.4) is divided in two zone: a thermal zone where occurs the oxidation of a part of the feed that provides the heat to the downstream steam reforming reaction in the catalytic zone. The output syngas temperature range is between 850 to 1100 °C.

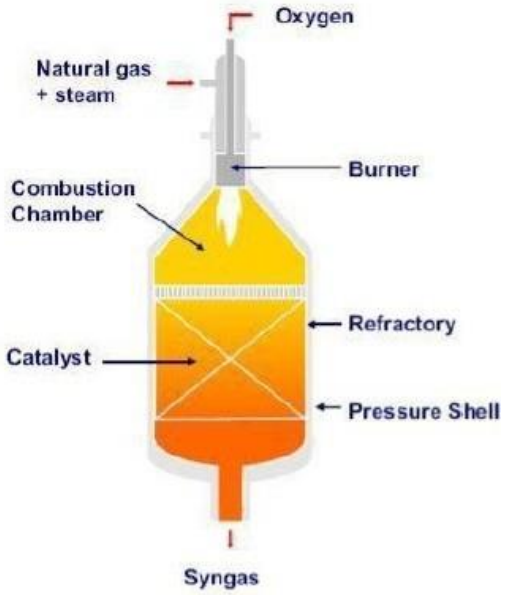

Figure 1.4: Auto-thermal reforming reactor

Autothermal reforming of light hydrocarbons and natural gas is not usually applied because of high operating costs and investment costs. These costs are mostly attributed to the cryogenic air separation unit needed for the oxygen production. The problem related to the catalyst deactivation due to carbon

deposits remains [1][7].

1.3 Catalytic Partial Oxidation (CPO)

Catalytic partial oxidation process has been proposed for both large scale and small-scale applications. It includes a sequence of exothermic and endothermic steps, where the fuel is first oxidized (partially or completely) and then converted into syngas through endothermic steam reforming. In the catalytic partial oxidation processes extremely active catalysts, like rhodium, guarantees almost complete conversion of the fuel and very high selectivity to syngas up to 90% [10] with milliseconds contact time. In this way, it is possible to design small-scale units, with lower capital and operative costs. CPO represents an optimal solution to convert hydrocarbon fuels into synthesis gas and presents the following advantages with respect to the other processes described before [10][11].

- CPO is mildly exothermic, while steam reforming is highly endothermic. For this reason, its reactor is cheaper and provides higher energy efficiency.
- The H_2/CO ratio in CPO is around 2 making it ideal for many downstream processes.
- The fast dynamic response and the milliseconds contact times allows the realization of the process in small reactors implying lower investment costs and simpler and more compact reactor [12] suitable for small scale applications.
- The process can take place using air instead of pure O_2 and so the cryogenic equipment for the separation of oxygen is avoidable. In addition, the presence of nitrogen, acting as a diluent, limits the excessive temperatures that could lead to catalyst deactivation.

On the other hand, there are some drawbacks that need to be taken into consideration:

- Sharp gradients of temperature and concentration in the catalyst volume due to the reaction mechanism resulting into the formation of hot spots on the catalyst surface that my lead to catalyst deactivation by sintering. This issue is particularly important when the reactor feed is composed by heavy hydrocarbons [13]
- Using air instead of pure O_2 to avoid the air separation unit reduces the cost

however leads to the production of diluted streams of syngas that may require nitrogen separation.

- The fuel oxidation taking place in the process contaminates the products stream with CO_2 even though in low concentrations.
- Coke formation, especially if hydrocarbons other than methane are fed, lead to catalyst deactivation.

Despite these drawbacks, catalytic partial oxidation technology is especially suitable for small-scale processes, in which crucial points are rapid dynamic response, energy efficiency and stringent volume constraints. This is valid both for fuel processors for stationary application (fuel cells or combined heat and power systems) and on-board syngas generators which serves a variety of uses such as H_2 injection in the combustion chamber, fueling of auxiliary power units and reduction of catalytic after-treatments units [14].

1.3.1 Catalytic partial oxidation of methane

The first results from the study of CPO were published in 1929 by Liander [15], in 1933 by Padovani and Franchetti [16] and in 1946 by Prettre et al. [17]. These show that a nearly complete methane conversion was only obtained for temperature around 850 °C. Following studies show that below this temperature value there was a non-equilibrium product distribution. Then also a problem of carbon formation over the supported nickel catalyst was pointed out. Due to these factors and the success of steam reforming, partial oxidation was abandoned for many years. At the beginning of the 90s, Schmidt and others demonstrated that the reaction could be carried out without soot formation, replacing nickel with noble metals, obtaining a conversion close to thermodynamic equilibrium[18][19].

Later, in 1995 most of the previous studies about the syngas production through CPO were collected by Bharadwaj and Schmid [20]. For relatively short contact times (in the order of 10^{-2} and 10^{-4} s), by choosing a rhodium-based catalyst, it was possible to achieve an almost complete conversion of methane with high selectivity of syngas (>90%). Finally, in 2004, Bizzi et al. [21] proposed an indirect-consecutive mechanism for the formation of syngas.

Reaction mechanism of methane CPO

The reaction mechanism of methane CPO consists of two indirect-consecutive steps [12][22] as presented in equations (1.7-1.11):

- Methane total oxidation, with the formation of H_2O and CO_2.
- Steam reforming of unreacted methane with the formation of synthesis gas.

$CH_4 + 2O_2 \rightarrow CO_2 + 2\,H_2O$	$\Delta H_r^0 = -802\ kJ/mol$	Methane total oxidation (1.7)
$CH_4 + H_2O \rightleftarrows CO + 3H_2$	$\Delta H_r^0 = +206kJ/mol$	Methane steam reforming (1.8)
$CO + H_2O \rightleftarrows CO_2 + H_2$	$\Delta H_r^0 = -41\ kJ/mol$	Water gas shift (1.9)
$H_2 + \frac{1}{2}O_2 \rightarrow H_2O$	$\Delta H_r^0 = -241.6kJ/mol$	Hydrogen oxidation (1.10)
$CO + \frac{1}{2}O_2 \rightarrow CO_2$	$\Delta H_r^0 = -283.2kJ/mol$	CO oxidation (1.11)

According to the presented reaction scheme, methane is totally oxidized forming CO_2 and H_2O (equation 1.7). This reaction is exothermic and provides heat to the following steam reforming reaction (equation 1.8), in which unreacted methane reacts with water giving as products hydrogen and carbon monoxide. From thermodynamic calculation results by York [10], to help the methane conversion and selectivity to CO and H_2, high temperature and low pressure are needed.

In 2009, Michael at al. [23] studied the effects of CO_2 and H_2O addition in methane CPO on different Rh-based catalyst coated on honeycomb ceramic monolith, over a wide range of inlet C/O ratios. The capillary sampling technique was used, which allows the analysis of integral reactor data with direct knowledge of the trends in temperature and species profiles within the catalyst bed. The data collected revealed the presence of two reaction zones: the oxy-reforming zone and the reforming zone: in the first one, O_2 mass transfer limits the rate of reaction, which is unaffected by H_2O and CO_2 addition. Downstream, the reforming zone of the reactor is primarily affected by co-feed through WGS chemistry: in H_2O-rich condition, the production of H_2 and CO_2 increased at the expense of H_2O and CO, while the opposite was observed in CO_2-rich tests. Moreover, CPO experiments with a simultaneous feed of H_2O and CO_2 provided direct evidence that H_2O is the preferential co-reactant of CH_4 in reforming and that CO_2 reforming is absent.

1.3.2 Catalytic partial oxidation of ethanol

Ethanol can be produced directly from biomass by fermentation, thus being a renewable fuel generates far less greenhouse gases than conventional fuels such as gasoline or natural gas [24]. Furthermore, the infrastructure needed for ethanol production and distribution is already established in countries like Brazil and the United States, since ethanol is currently distributed and used as an octane enhancer if blended with gasoline or used as a fuel itself [24][25]. By converting ethanol into hydrogen-rich gas, it can be used as a hydrogen source for various

fuel cells. There are essentially three ways to perform this conversion [26]: the first is steam reforming (Equation 1.12) which, although it is a very efficient process to produce hydrogen- rich streams, has the great disadvantage of being a highly endothermic process. Consequently, a big amount of thermal energy must be added to the process in order to achieve high conversion. The second is the partial oxidation (Equation 1.13) in which the reactor is more compact because the amount of heat to be supplied through a heat exchanger is less. The last is the Autothermal reforming which combines SR, partial and total oxidation in one reactor. Unlike other hydrocarbons, such as methane, the partial oxidation of ethanol is slightly endothermic, thus part of the fuel must be completely oxidized (Equation 1.14) to generate the heat required to perform the process in autothermal way. For this purpose, a small excess of oxygen with respect to the stoichiometry of the partial oxidation is feed to the reactor.

$$C_2H_5OH + H_2O \rightarrow 2CO + 4H_2 \qquad \Delta H_r^0 = +256\ kJ/mol \qquad (1.12)$$

$$C_2H_5OH + \frac{1}{2}O_2 \rightarrow 2CO + 3H_2 \qquad \Delta H_r^0 = +14\ kJ/mol \qquad (1.13)$$

$$C_2H_5OH + 3O_2 \rightarrow 2CO_2 + 3H_2O \qquad \Delta H_r^0 = -1277\ kJ/mol \qquad (1.14)$$

From the late 90s and early 2000s CPO and autothermal reforming of ethanol was an area of great research interest: In 1999, Marinov [25]presented a kinetic model for the homogeneous oxidation reactions of ethanol at high temperature.

Cheekatamarla and Finnerty [27] analyzed the performance of the CPO of different fuels such as ethanol, n-hexadecane, synthetic JP8, desulfurized kerosene and desulfurized diesel. Higher hydrogen concentration was noticed from ethanol CPO compared to other liquid fuels. More recently, Diehm at al. [28] examined the catalytic partial oxidation of ethanol/iso-octane blends over rhodium/alumina catalysts. In this paper, mixtures with ethanol concentrations varying from 5 to 85 vol. % are studied for several operating conditions ranging from fuel lean to fuel rich conditions. In the blends, the conversion of ethanol is almost complete for lean operation as well as the conversion of iso-octane. For all mixtures a hydrogen yield of over 80% in millisecond contact times is shown, with the highest yield for a blend with 10 vol. % ethanol. Nevertheless, for a high ethanol, generally a high by-product formation is observed already at fuel lean conditions. Finally, they compared the behavior of ethanol/iso-octane blends with commercial ethanol-blended fuels: in particular, a blend containing 5 vol.% ethanol is selected as model system for 95 RON gasoline while for commercial E85, gasoline blended with 85 vol.% ethanol, the model system is an ethanol / iso-octane blend with 85% by

volume of ethanol. A good agreement between the performance of the commercial fuels and the corresponding ethanol/iso-octane mixtures is observed. Thus, the two-component blend can be used as a model system for a complex mixture as the one of commercial fuel that is composed of several hundred different hydrocarbon species.

Liguras at al. [29] tested Ru catalysts supported on cordierite monoliths, ceramic foams and $\gamma - Al2O3$ pellets. They concluded that Ru supported on a cordierite monolith, exhibited excellent catalytic performance for a wide variety of process conditions and excellent long-term stability with low amounts of coke deposition. Significant effects were observed for changes in the feed oxygen-to-ethanol ratio. However, all the three supports were able to completely convert ethanol with high selectivity towards the desired products. The effect of the support has been also studied by Chen at al. [30]: in their paper they analyzed different support such as La_2O_3, Al_2O_3, CeO_2 and ZrO_2 and for different active phases; they concluded that Ir/La_2O_3 may be used as a promising catalyst for hydrogen production via autothermal reforming reaction of ethanol.

Some studies concerning the active phase were conducted by Rodrigues at al. [31][32] in these papers they analyzed the behavior of the process using first $CuO/\gamma - Al_2O_3$ than $Co_3O_4/\gamma–Al_2O_3$ catalyst in a cordierite honeycomb monolith.

Salge at al.[33], in 2005, investigated the catalytic partial oxidation of ethanol and ethanol-water over noble metal and metal plus ceria-coated alumina foams at catalyst contact times lower than 10 ms: feeding only ethanol they saw that Rh–Ce is the more stable and active catalyst and the selectivity to H2 peaks at about 80% at a C/O ratio of about 0.7, perhaps due to the redox capabilities of Ce. Less H_2 and more by-products were produced over Rh, Rh–Ru, Pt, and Pd catalysts. Finally, Under the conditions used, all reactions appear to occur on the surface, except for the formation of some by-products such as acetaldehyde and ethylene. The addition of water to the Rh–Ce catalyzed reactor, increased H_2 selectivity to values higher than 100%, this, because both ethanol and water contribute to the formation of H2. Due to increased WGS and steam reforming activity, CO selectivity decreased to < 50% and the selectivity towards by-product was < 3%.

The main obstacle of Ethanol CPO is mainly related to its flammability limits: ethanol–air mixtures are flammable over a wider composition range than gasoline-air mixtures. Flames are intolerable because they lead to unsteady operation and form coke and soot, which deactivate the catalyst [33]. Figure 1.5 shows a representation of the flammability range of $EtOH/N_2/Air$ mixture as the concentrations of the species vary.

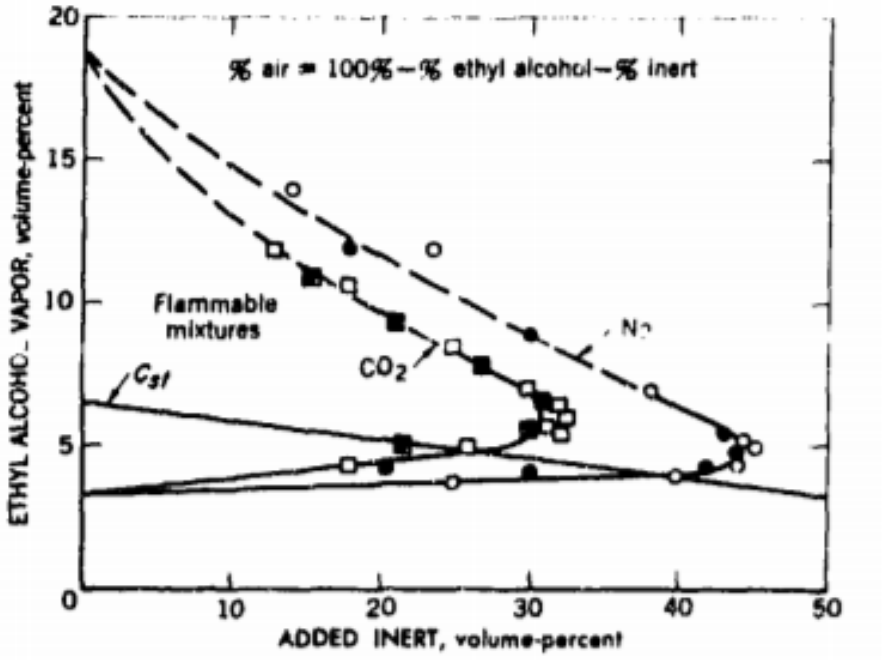

Figure 1.5: Flammability range of a EtOH/N_2/Air at 25°C and Atmospheric Pressure [28]

1.3.3 Catalytic partial oxidation at Politecnico di Milano

Catalytic partial oxidation has been intensively studied by the Laboratory of Catalysis and Catalytic Processes (LCCP) at the Politecnico di Milano.

Donazzi et al. [12][22], studied the kinetic of CH_4 CPO over 4%Rh/$\alpha - Al_2O_3$ catalyst in an isothermal annular duct reactor externally heated. They found that CPO proceeds through an exo-endothermic indirect consecutive reaction mechanism, consisting in a first step of total oxidation (Equation 1.7), followed steam reforming (Equation 1.8); the final composition can be also affected by WGS (Equation 1.9), H_2 (Equation 1.10) and CO (Equation 1.11) oxidation. An intense study was also carried out by the same group on different types of feedstocks, other than methane, such as propane (C_3H_8) [34] and propylene (C_3H_6) [35] over a 2%Rh/$\alpha - Al_2O_3$ catalyst, to understand the kinetic reaction mechanism. The results showed that, in line with CH_4, the CPO of C_3H_8 and C_3H_6 proceeds according to an indirect route which entails total oxidation, followed by steam reforming. In both cases the two reactions were consecutive because of an evident inhibiting effect of O_2 on steam reforming. More recently, da Silva et al. analyzed the CPO of acetic acid reaching similar conclusions with respect to the CPO of hydrocarbons [36].

In order to have better comprehension of the process the spatially resolved sampling technique was developed and applied. This method allows for an in-depth knowledge both gases and surface temperature, which provides key

information for understanding the interaction between among gas phase chemistry, surface chemistry and heat and mass transfer processes, and the gas composition. The accurate acquaintance of all these data is important not only for reactor design and optimization strategies of operating conditions, but also, they allow to know the temperature of the hot spot, thus optimizing it, is possible to achieve good compromise between the duration of the catalyst and the adequate reaction rate. In this respect in situ sampling technique provided information on the spatial evolution of temperature and concentration. If, from one side, the temperature profiles give information on the temperature trend in the catalyst, on the other side, the concentration profiles reveal the existence of two reaction zones: an oxy-reforming zone where oxygen is still available in the gas phase and a reforming zone starting after the complete depletion of oxygen. In the oxy-reforming zone both exothermic oxidation reactions and endothermic reforming reactions take place explaining the presence of the hot spot before mentioned [13]. This sampling technique is exploited by several works reported in literature[13][14][37][38][39]: the temperature probes consisted of a thin K- type thermocouple and a VIS-IR optical fiber connected to an infrared narrow band. The IR detector was an Indium–Gallium–Arsenic photodiode with a spectral range of 1.45–1.8 m. The tip of the optical fiber was industrially polished at an angle of 45° in order to guarantee the local measurement of the temperature. Noteworthy, the temperature measured by thermocouple and the optical fiber represent the temperature of the gas phase and the surface, respectively. Both temperature probes were inserted into a deactivated fused silica capillary, which served as a protection sheath. The end of the capillary was sealed by melting to isolate the temperature probe from the reacting system. The capillary was inserted in a central channel of the reactor and could slide along the axial coordinate by means of a linear actuator, which has very high spatial resolution. An analogous system was used to measure the axial profile of the gas composition. The capillary used in this case was open at the tip and smaller in diameter, in order to minimize the disturbances of the probe on the flow field inside the channel. For the same reason, the gas samples were withdrawn starting from the reactor outlet, moving towards the inlet, counter currently to the reacting flow, from the capillary tip, at a low sucking rate. At each axial position three samples were analyzed, and mass balances typically closed within 5% error. The sampled gases were examined with an Inficon MicroGC Fusion chromatograph. The instrument was equipped with two fused silica columns: Rt -Molsieve 5A, which uses argon as carrier gas, and Rt -Q-Bond which uses helium. The used analysis method includes a temperature ramp which allows optimal separation of the species.

The spatially resolved sampling technique has been applied several times for the

study of the CPO in adiabatic reactors: in 2011, Donazzi et al. [40] investigated the effect of dilution by N_2 at first and then CO_2 to CH4/air mixtures: they found that in both cases at increasing dilution the conversion of CH_4 and the gas temperatures decreased, but the effect of carbon dioxide is exhibited more important than the one of nitrogen; however, at increasing N_2 dilution, the H_2/CO ratio slightly increased, instead at increasing CO_2 dilution, the H_2/CO ratio showed more significantly decrease. The same group performed other researches concerning the same field: they analyzed the effect of pressure at which the CPO of propane and methane is carried out, coming to the conclusion that the pressure affects the heterogeneous process thermodynamically but not kinetically [41]. Furthermore, the effects of different geometrical configurations of the optical fiber probe were examined, showing that the expected surface temperatures are closely captured with a 45◦ angled device [13]. They also explored the influence of the reactor configuration, in particular the effect of the position of the front heat shield (FHS) [39]. From their results they concluded that: by locating the FHS at distance from the catalytic monolith, at the expense of a small loss of thermal efficiency and a very moderate loss of performance in terms of conversion and selectivity, a decrease of over 100 ◦C for the hot spot temperature was obtained, which can in principle greatly enhance the catalyst lifetime.

Based on the obtained results, the CPO of iso-octane (i−C8H18) over 2%Rh/α − Al_2O_3 catalyst, was studied[42] as a liquid fuel. They discovered that, similarly to the CPO of light hydrocarbons, the iso-octane CPO process follows a reaction pathway which mainly consists of the exothermic combustion reaction and the endothermic steam reforming. This consecutive reaction mechanism results in the formation of a hot spot of temperature at the catalyst inlet. However, the lower diffusion coefficient of iso-octane, compared to light hydrocarbons, is responsible for the important impact of mass transfer limitations on the global rate of steam reforming reaction. This results in a hot spot of temperature close to 1000 C, which is detrimental for the catalytic activity. In fact, at temperatures above 900 C sintering leading to loss of catalytic activity is expected.

In 2013, Livo et al.[37] focused on the catalytic partial oxidation of ethanol over a Rh/α−Al2O3 coated monolith. Using a spatially resolved sampling technique they collected axial concentration profiles, as well as surface and gas phase temperature profiles. At first different C/O ratio were studied: the investigations clearly showed two zones inside the catalytic channel, an oxy-reforming zone, as long as oxygen is present, with total oxidation and steam reforming as prevalent reactions, and a reforming zone, with steam reforming as the dominating reaction. Moreover, homogeneous gas-phase reactions, leading mainly to acetaldehyde and water, were observed in front of the catalyst. Depending on the C/O ratio, the by-

products may be consumed in steam reforming by the end of the catalytic channel. From the profiles obtained it can be clearly seen that CPO of ethanol is highly sensitive to the composition of the feeding mixture. In this respect, very fuel-lean conditions need to be employed in order to achieve high syngas productivity. Additionally, axial profiles were collected at a fixed C/O ratio in three catalytic channels, which were differently located across the monolith. A radial heat loss from the center to the outer channels of the monolith was observed, which led to variations in the axial concentration profiles across the honeycomb, especially for the channel close to the edge of the monolith, in which steam reforming proceeded to a lesser extent due to the lower temperatures.

More recently, Batista et al [43] studied the effect of the flow rate on the catalyst life, discovering that the increase of the inlet flow rate promotes the adiabaticity of the reactor, but it leads to a higher catalyst hot spot temperature, due to the higher inlet enthalpic flux worsening the catalyst stability. The optimal inlet flow rate has been set to 10 NL/min, this setting guarantees the best compromise between the adiabaticity of the reactor and the stability of the catalyst. Finally, Mostafa et al. [13] studied the effect of water co-feed in the CPO of Ethanol over $Rh/\alpha - Al2O3$ catalyst deposited on cordierite honeycomb monolith. For this purpose, they exploited a spatially resolved sampling technique to obtain the axial temperature and concentration profiles. The effect of steam co-feed was examined at fixed C/O ratio equal to 0.65, varying the H2O molar concentration in the feed from 0% to 10%. They noted that, at increasing H2O feed content, ethanol conversion grew close to 100%. The water gas shift reaction was promoted, which resulted in increased H2 yield and H2/CO ratio, moreover, a significant drop of the concentration of cracking products such as CH4, and C2H4 in the initial part of the reactor was observed. Globally, thermal effects of the water co-feed were negligible. Finally, less pronounced increase of the temperature profile in CH4-CPO, used as a reference reacting system, was detected, it means that water co-feed produces less coke. This is also confirmed by the TPO test.

Bressan et al [44]studied the effect of using a Mg-alumina supported catalyst and concluded that feasibility of developing structured catalysts with high catalytic activity using the Mg-alumina spinel. The catalysts supported on $MgAl_2O_4$ reported higher stability which may be explained by the reduced tendency towards coke formation. A better understanding of the role of the active phase support through a dedicated kinetic study is required.

1.3.4 Catalyst for catalytic partial oxidation

Several catalysts have been studied in the literature among which noble metals

present the highest activity allowing the use smaller catalyst use and faster dynamic response. Additionally, such catalysts reduce the risk of coke formation with respect to non-precious metals as Ni and Fe [43]. Among the noble metals, rhodium has been mostly studied for the partial oxidation of natural gas and liquid hydrocarbons and was demonstrated that is the best catalyst both in terms of activity and selectivity towards hydrogen, moreover it has low tendency to carbon formation[46][47][47]. Such evidence makes the Rh based catalysts the best candidate for the development of reactors suitable for small scale applications.

Liguras et al [29] studied the effect of different structures, such as ceramic foams, cordierite monoliths and $\gamma - Al2O3$ pellets on the ethanol CPO. The cordierite is a ceramic material in form of $2MgO \bullet 2Al2O3 \bullet 5SiO2$. Comparing the same active phase on all these different structures, the catalyst deposited on all three supports was able to completely convert ethanol with high selectivity to the products desired. The catalyst supported on alumina pellets showed very good catalytic behavior, but due to high pressure drop they might be not suitable for mobile applications. In comparison, catalysts supported on a ceramic foam provided better performance, probably due to smaller pore size and higher tortuosity of this support. However, the one supported on cordierite monolith, shown excellent catalytic performance for a large variety of process conditions. Also, cordierite does not interact with the wash-coat, manifests a low thermal expansion coefficient and had high stability at high temperatures ($T_{melting} = 1450°C$). Other relevant features were the homogeneous distribution of the reactants and the compactness. Because of all these positive features cordierite honeycomb monoliths 400/7 CPSI (channels per square inch), are used in the present thesis.

The Autothermal operation of the CPO is characterized by extremely high temperatures which can compromise long-term catalytic performances, due to thermal sintering of the metal clusters. So, the thermal stability of the catalyst and its support are key features [45]. The addition of wash coat not only tends to increase CO and H_2 yields [48], but also guarantee a good dispersion of the active phase and thermal resistance in extreme conditions. Several supports have been studied by Aupr´etre at al.[47] for the ethanol CPO, such as $\gamma - Al2O3$, 12%; $CeO2$; $Ce0.63Zr0.37O2$. Among the supports investigated, Rh on $\gamma - Al2O3$ catalyst clearly appeared as the most active and selective catalyst. More recently, by the research group of Politecnico di Milano it has been shown that using $\alpha - Al2O3$ as a support, there is an improvement in performance. The major drawback of this support is related to its acidity. Since acidity promote ethylene production, which is a coke precursor, most of the acidic sites should be neutralized. For this purpose, is useful to replace $\alpha - Al2O3$ support with $MgAl_2O_4$[49][50]. Magnesium aluminate spinel ($MgAl2O4$) is a non-acidic and moderately basic support that

owns a unique combination of desirable properties: high melting point (2135 °C), high resistance against chemical attack, good mechanical strength both at room and high temperature[51], and finally, improves the stability of the rhodium particle upon reaction.

1.4 Catalyst deactivation mechanism

1.4.1 Coking (Fouling)

Coking is the chemical deposition of carbonaceous species on the catalyst surface. The phenomenon is common to all process involving hydrocarbons. Coking leads to covering of the active sites and blockage of the catalyst pores. Formation of carbonaceous deposits progresses from the external surface up to the core of the catalytic grain. Coke deposits partially obstruct the pores and slows down the diffusion of the reactants inside the catalyst before blocking the pores[52]

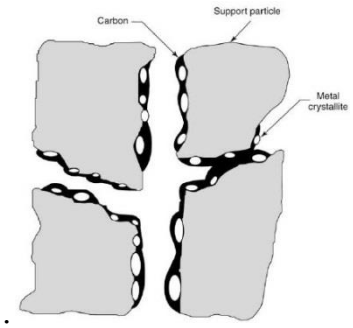

Figure 1.6: Conceptual model of coking

Several types of carbonaceous species exist. The nature of the carbonaceous deposits (coke) depends on the process conditions, the feed composition, the catalyst formulation. Deposits are usually made of high molecular weight polyaromatic structures C/H ratio between 1 and 2. Metal carbides can be also formed, or carbon can be deposited on the active phase. Carbon is formed via disproportionation of CO while coke is formed via dehydrogenation with polymerization, olefin cyclization or cracking of organic molecules [52].

Coking phenomenon can be limited by:

- optimizing the catalyst composition (addition of alkali to poison acid sites of the catalyst and to promote the carbon gasification reactions
- optimizing the pore structure
- using high partial pressure of H_2, O_2 or H_2O to promote gasification

reactions

- minimizing the presence of the coke precursors in the feed

1.4.2 Sintering

Sintering is the loss of superficial area caused by the growth of the active phase crystallites. Sintering processes generally occurs at high temperatures and have high activation energy: the process temperature is the most important parameter.

Sintering of supported metals occurs via:

- migration of crystallites on the support, collision and coalescence
- migration of the particle on the surface, coalescence with bigger crystals

Factors affecting the sintering of supported metals: presence of oxidizing or reducing agents, nature of support, metal loading, form and size of the crystallites, presence of impurities [52].

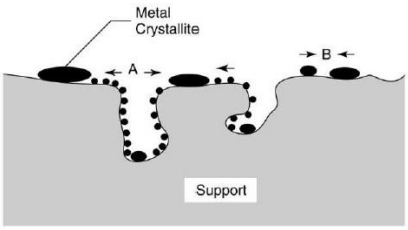

Figure 1.7: Two conceptual model of sintering

Sintering phenomena can be limited by:

- lowering the process temperature
- limiting the catalyst exposure to atmospheres favoring sintering
- adding sintering inhibitors

Moreover, there are other concepts such as poisoning, masking, phase transformation and attrition that result in catalyst deactivation; however, these concepts are not applicable for the catalysts and the working conditions that are used in this study since pure ethanol is used as feed, and nonvolatile compounds are not seen in the system.

2. Materials and methods

In this chapter the preparation of catalyst will be described step by step from the preparation of the catalytic powders to the different coating techniques. Different commercial supports will be used during this preparation and their effect will be tested in different rigs, depending on the investigation that has to be carried out. Depending on the rig, the coated structures can be ceramic monoliths or tubes. Following the catalysts preparation part, a brief description of the two rigs will be carried out. At the end, the kinetic model for SR and CPO of methane and ethanol will be introduced.

2.1 Preparation of the catalytic powders

In this thesis work, washcoat catalysts have been used. Precisely 10 tubes and 1 monolith support were coated by slurries with different recipes. The steps that have to be followed can vary depending on the support and on the slurry that has to be used for covering them. The procedures for the preparation of tubes catalysts and monolith one were developed and tested in previous works [57][58][59][44] and described in this paragraph.

2.1.1 Calcination

The first step is the same for all the catalysts prepared in this work. The preparation of the washcoat is based on preparing slurries of the active phase supported on metal oxide powders. The supporting powders used in this work are commercially available products. Three types of supports were used, α-Al_2O_3 (Puralox SCFa-140), Mg-Al_2O_4 (Puralox 28-100) and La-Al_2O_3 (Puralox SCFa-140-L3), and all of them were calcinated following these steps:

- controlled heating form T_{amb} to T = 1100°C with a rate of 1°C/min
- permanence at 1100°C for 10 hours
- controlled cooling from T = 1100°C to T_{amb} with a rate of 2°C/min.

2.1.2 Impregnation

Once the powders are ready, rhodium, the active element, must be added. The technique employed is the dry impregnation (or incipient wetness impregnation): this consists in impregnating drop by drop the powders of the support with an amount of solution equal to the pore volume of the support itself. In this way, any loss of active

element is prevented and the exact amount of Rh deposited on the catalyst is known[60]. A solution of rhodium nitrate ($Rh(NO_3)_3$) in water (16.65% w/w) was used.

First, the mass of rhodium (m_{Rh}) necessary to reach the desired percentage y_{Rh}=2% w/w is calculated:

$$m_{Rh} = \frac{m_{\alpha-Al_2O_3} * y_{Rh}}{1 - y_{Rh}} \tag{2.1}$$

where $m_{\alpha-Al_2O_3}$ is the mass of support subjected to impregnation. Then, the required mass of nitrate solution (m_{sol}) is evaluated, using the mass fraction of rhodium in the solution $\omega_{Rh_{sol}}$:

$$m_{sol} = \frac{m_{Rh}}{\omega_{Rh_{sol}}} \tag{2.2}$$

From the mercury intrusion measurements, it is possible to evaluate the pore volume $V_{porous\_specific}$ of the supports. The amount of impregnating solution m_{sol} must be diluted up to reach a volume (V_{pores}) equal to pore volume, according to dry impregnation procedure.

$$V_{pores} = m_{\alpha-Al_2O_3} V_{porous\_specific} \tag{2.3}$$

However, since a flask with a fixed volume is available (5 mL), the impregnating solution had to be furtherly diluted up to reaching this volume (V_flask). In conclusion, the mass of Rh nitrate solution that has to be used is:

$$m_{sol\ final} = \frac{V_{flask}}{V_{sol}} m_{sol} \tag{2.4}$$

The impregnation procedure consists in a slow dripping of the solution onto alumina powders by periodically mixing the sample with a spatula so that all the liquid is absorbed by the powders. The dripping is stopped when the dropped volume is equal to pore volume, hence when:

$$V_{dropped} = V_{pores} \tag{2.5}$$

For the dripping procedure, a graduated burette was used on a support, while the powders were contained in a crystallizer. After the impregnation, the catalytic powders are placed in an oven at 120°C for at least 3 hours to dry, so that only the rhodium nitrate remains on the powders. This thermal treatment also makes the

solution supersaturated (for the evaporation of the solvent) and makes the active element crystalize, fixing onto the surface of the support.

Also in this case, this procedure was followed for each slurry prepared.

Figure 2.1, Figure 2.2 and Figure 2.3 show the equipment used for the impregnation process.

Figure 2.1: Flask containing diluted rhodium nitrate solution

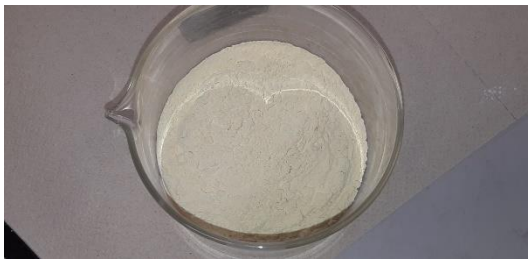

Figure 2.2: Impregnated $\alpha - Al_2O_3$ powders before removing the excess water

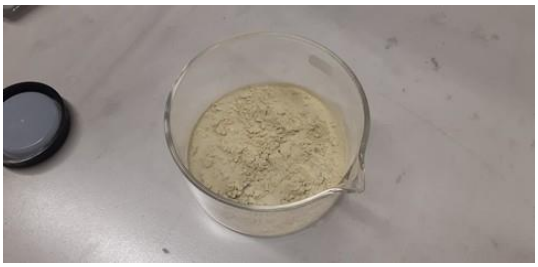

Figure 2.3: Impregnated $\alpha - Al_2O_3$ powders after drying at 110°C

2.1.3 Preparation of the slurry

Rheological properties of the slurry are fundamental for the efficacy of the subsequent deposition step. In particular, its viscosity should be properly tuned by regulating its composition.

This step differs depending on the slurry that has to be prepared.

HNO_3-based slurry

A stable suspension is prepared, dispersing impregnated alumina and magnesium-alumina powders in water, using a monoprotic acid (HNO_3) as dispersant. The latter is responsible for the stabilization of the suspension, by charging the surface of the powder [61].

Both the ratios H_2O/powder and HNO_3/powder influence final properties of the slurry, because "external" water (i.e. water not adsorbed inside the pores) and powder surface acidity affects viscosity. Hence, powders pore volume regulates the H_2O/powder ratio, while the amount of acid that must be used depends on powders maximum surface charging[61].

To create a slurry with the desired characteristics, it is advisable to use a quantity of distilled water equal to 1.4 mL/g_{powder} and of nitric acid equal to 1.7 $mmol/g_{powder}$.

The amount of nitric acid is hence calculated as follows:

$$m_{HNO_3} = \frac{m_{powder} * 1.7 * PM_{HNO_3}}{1000} \tag{2.6}$$

Knowing nitric acid concentration in the starting solution (65% w/w), the mass of required solution is easily calculated. The amount of water that has to be added is calculated by difference:

$$m_{H_2O} = 1.4 * \rho_{H_2O} * m_{powder} - \frac{m_{HNO_3}(1 - 0.65)}{0.65} \tag{2.7}$$

This is the procedure followed in this work to obtain the F_series catalysts, both with Mg-alumina and α-alumina.

Glycerol-based slurry

This recipe was determined during Bressan thesis [44] starting from previous studies led at Politecnico di Milano [62][63][64].

Liquid medium composed of glycerol (G) (Purity: 99.9 %, Thermo Fisher Scientific), distilled water (H2O), and polyvinyl alcohol (PVA). These three compounds were used as dispersant, solvent / diluent and binder, respectively.

PVA was dissolved in water at 85°C under continuous stirring. The solution, cooled down to room temperature and continuously stirred, was then mixed with glycerol and stirred again to enhance the mixing process. This method was used for the La-alumina monolith catalyst and for MB1, an alumina tube.

After the preparation, the slurry is put in a plastic container and subjected to ball milling, a controlled mixing procedure that aims to homogenize the dispersion and to decrease powder particle size (Figure 2.4, Figure 2.5). To this purpose, zirconia balls are put inside the slurry in an amount equal to 8 times the initial mass of powder. Smaller particles favour the adhesion capability of the coating material, but, however, viscosity also increases[60]. The plastic container in inserted in a ceramic closed cylinder and placed on the ball milling machine where rotating rollers driven by an adjustable electric motor sustain a constant rotational speed of 90 rpm for 24 hours as shown in Figure 2.5. For the glycerol recipe, ethanol was added after the milling to reduce foaming as explained by Ambrosetti et al. [64]

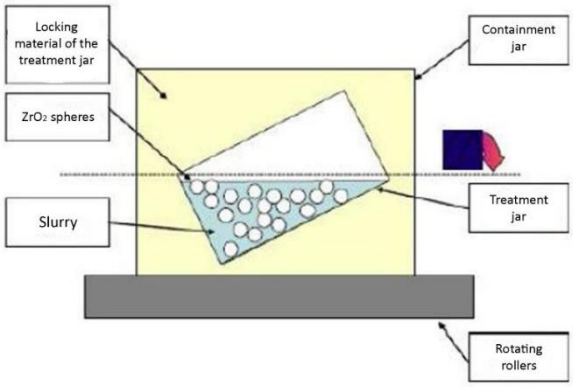

Figure 2.4: Representation of ball milling

Figure 2.5: Ball milling process

2.2 Preparation of the catalyst coated structures

As said at the beginning of the chapter, different structures are coated in this thesis work. The coating procedure differs depending on the structure that has to be covered. For the coating of tubes, a dip coating technique is used, while for the coating of monolith, a percolate spin-coating technique has to be used.

2.2.1 Coating of ceramic tubes: Dip coating technique

A dip coating procedure is performed to deposit the slurry on the tubes. An electrically driven vertical slide is employed and the tube, attached to it (Figure 2.6, Figure 2.7), is immersed in a graduated cylinder containing the slurry. To optimize this step, it is necessary to keep a slow and controlled speed of withdrawal of the tube. The faster is the extraction of the tube from the cylinder, the higher is the coating load [65]. It is recommended to maintain a withdrawn speed higher than 3 cm/min [65]. Good properties of the slurry are also important (in particular, viscosity and homogeneity) for the success of this step of preparation. The higher is the viscosity of the slurry, the higher is the coating load per immersion, but, consequently, the adhesion diminishes[60]. The major goal is to deposit a uniform layer, well adherent to the alumina tube. In order to cover only the desired length of the tube, Teflon is used to cover the limiting zones.

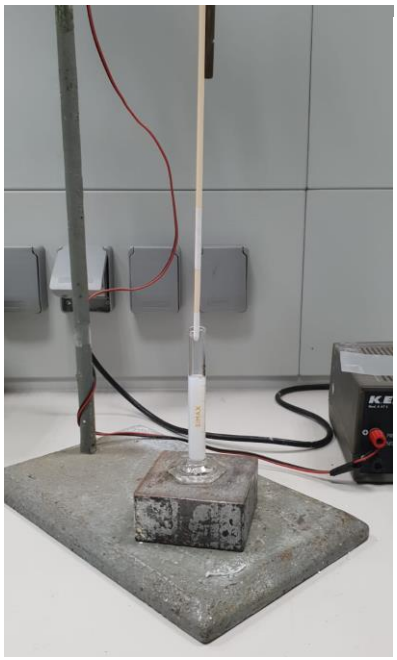

Figure 2.6: Picture of dip-coating for primer deposition

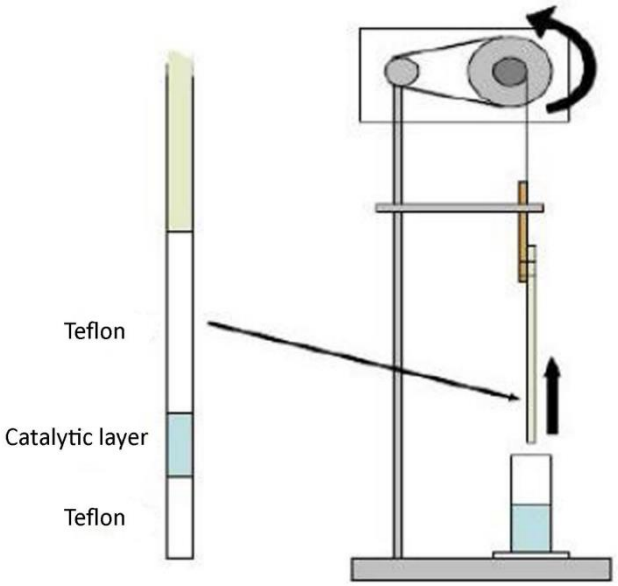

Figure 2.7: Representation of dip-coating procedure

After this step the coated tube must be dried in order eliminate the solvent from the pores. This phase is delicate, since drying can generate strong capillary forces that can origin cracks, thus affecting the adhesivity. For this reason, a controlled thermal treatment must be adopted[60]. In particular, the alumina tubes prepared in this thesis work, once extracted, were subjected to a flash drying in oven at 280°C for about 10 minutes. This procedure limits shrinkage effect and permits a good fixation of the layer

on the tube [60]. Before the deposition of the catalytic slurry, a primer layer is deposited on the alumina tube in order to increase the adherence of the washcoat layer on the tube. A boehmite primer was used, prepared by dispersing 10% v/v of a commercial aluminium hydroxide powder (Disperal®, Condea Chemie) in a 0.4% w/w water solution of HNO_3[65]. This layer leads to an increase of surface roughness, hence favouring the adhesion of the catalytic layer. The methods of deposition of the primer are similar to those of dip coating, with the only difference that drying takes place leaving the tube for about 30 minutes at ambient temperature.

At each stage of the process the tubes were weighed (before the primer, after the primer, after the dip coating) and the weight of the deposited catalytic layer was therefore calculated by difference. For each weighing, the measurement was repeated at least three times and the average value was taken as the final measure.

2.2.2 Coating of ceramic monoliths: Percolate spin-coating technique

Also in this case, the monolith is covered with a primer in order to improve the adhesion of the washcoat layer.

The monolith in this work was prepared through percolate-spin coating technique, where the percolate coating substitutes the dip-coating. The bottom side of the monolith was placed on a small quartz tube, instead the top side was inserted in a long quartz tube. The idea was to drop the slurry into the upper quartz tube and wait for it to move through the monoliths' channels (Figure 2.8). To reduce at minimum the slurry waste, parafilm slices are placed below the small quartz tube and also the monolith was wrapped with it so that the only available paths for the slurry are the monolith channels.

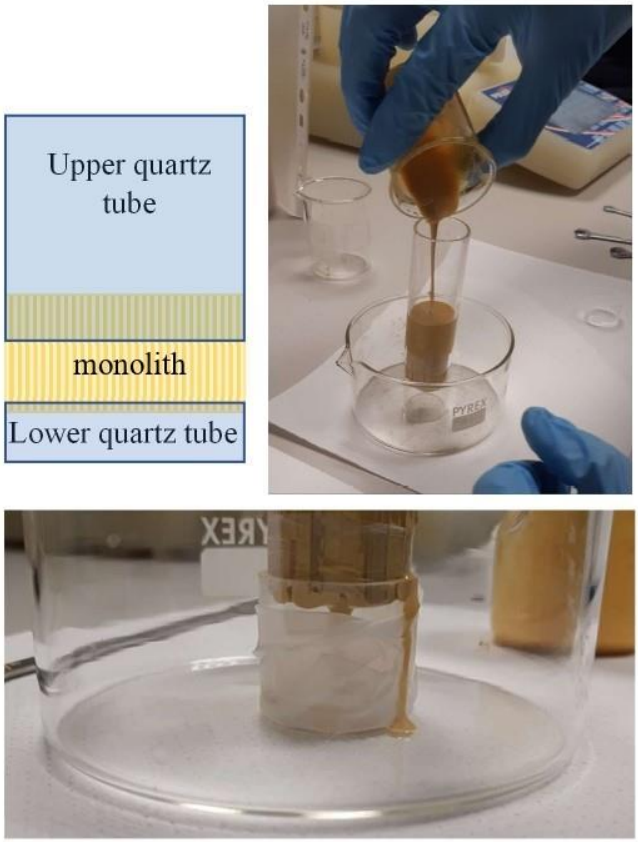

Figure 2.8: Percolate coating procedure

To eliminate the excess slurry from the channels, a spin-coating machine was used (APT Automation, SPIN150i), showed in Figure 2.9. This machine, rotating the monolith, applies a centrifugal force able to push the slurry out of the support. During Bressan thesis work [44] a new sample holder (Figure 2.10) was developed and 3D printed to keep the monolith in position during the spinning. As reported by Balzarotti et al.[62], spin acceleration was held constant at 1000 rpm/s for 20s. Then, the monolith was flash dried at 350°C for 6 minutes in an oven and at the end calcinated for 10h at 600°C with a heating ramp of 2°C/min as well as the cooling one, with the aim of eliminating the carbon deposits formed in the monolith surface.

Figure 2.9: Spin-coating machine

Figure 2.10: New spin-coating sample holder

2.2.3 List of catalysts prepared

During this thesis work, both tubes and monolith were prepared, using different kinds of slurries as said before. Lengths and mass of the catalytic layers deposited on each tube are listed in Table 2.1 and Table 2.2, together with the slurry used for their preparation.

Tube	Slurry	Length [cm]	Mass of the catalyst [mg]
F1	α-alumina	3	19.83
F2	Mg-aluminate	3	19.93
F3	α-alumina	3	19.61
F4	Mg-aluminate	3	16.59
F5	Mg-aluminate	3	26.80
F6	Mg-aluminate	3	21.88
F7	Mg-aluminate	3	20.58
F8	Mg-aluminate	3	24.27
F9	Mg-aluminate	3	13.87
MB1	α-alumina with Glycerol	3	15.00

Table 2.1: List of catalytic tubes prepared during this thesis work

Monolith	Slurry	Length [cm]	Mass of the catalyst [mg]
MarkLaI	La doped alumina	3.34	849.00

Table 2.2: List of catalytic tubes prepared in this thesis work.

2.2.4 Catalyst analysis

In this section the methods and the results in the characterization of the washcoat and the synthesized catalytic powders are briefly illustrated.

BET analysis

The BET (Brunauer, Emmet and Teller) theory is commonly used to evaluate the gas adsorption data and generate a specific surface area result expressed in units of area per mass of sample (m^2/g). The specific surface area of a material is then determined by the physical adsorption of a gas (typically nitrogen, krypton, or argon) onto the surface of the sample at cryogenic temperatures (typically liquid nitrogen orliquid argon temperatures). In a previous work[44], the surface area of the powders has been determined by means of a TriStar Micrometrics analyzer, employing the BET technique. Nitrogen, used at liquid temperature (77.35 K), can physically adsorb on the powders surface where the adsorbed nitrogen moles increase proportionally to the pressure of the liquid and the link between these two quantities constitutes the adsorption isotherm. Table 2.3 shows the BET analysis results obtained on $\alpha - Al_2O_3$ and $MgAl_2O_4$ and samples.

Washcoat	$T_{calcination}$[°C]	BET area $[m^2/g]$
$\alpha - Al_2O_3$	1100	8
$MgAl_2O_4$	1100	31.68

Table 2.3: BET surface area results

Porosimetry

The specific porous volume of the powders, fundamental information during the impregnation process, in a previous thesis work[44], has been determined by means of two fluids: mercury and water.

As for the mercury porosimetry, the measurement was carried out using an Auto-Pore Micrometrics porosimeter performing two pressurizations: with the first the mercury enters the intraparticle spaces and it breaks up the aggregates, while with the second it only penetrates the pores. The pressure necessary to push the mercury into a pore is inversely proportional to the radius of the pore via the following relationship:

$$p = 63000 / r_p \tag{2.8}$$

Where $r_p[\dot{A}]$ is the pore radius and p [atm] is the pressure. The experimental conditions adopted during the analysis were the following:

- Pre-treatment: void till 5 psi (5 psi/min) and 5 minutes hold at ambient temperature
- Low pressure analysis: 50 – 900 μmHg
- High pressure analysis: 2-3300 psia (alumina powders), 0.51-21000 psia (magnesium aluminate powders)

Regarding the water porosimetry, a certain amount of powders was chosen and then proceeded as a normal dry impregnation: as much water as necessary was added drop by drop to fill all the pores, but still leaving everything dry. At the end of the process knowing the initial amount of powder and the volume of water added the pore volume was determined through the following equation:

$$\hat{V}_{p,sup} = \frac{V_{H_2O}}{m_{sup}} \tag{2.9}$$

Where $\hat{V}_{p,sup}[ml/g]$ is the pore volume per gram of support, $V_{H_2O}[ml]$ is the volume of the added water and $m_{sup}[g]$ is the initial mass of the powder. The following table summarized the obtained results.

Powders	$T_{calcination}[°C]$	$\hat{V}_{p,sup}[ml/g]$	Porosimetry fluid
$\alpha - Al_2O_3$	1100	0.22	Mercury
$MgAl_2O_4$	1100	0.33	Water
$Al_2O_3 - La$	1100	0.46	Water

Table 2.4: Porosimetry results

Chemisorption

The chemisorption has the aim of find how much rhodium is exposed with respect to the total rhodium. To do this, a calculation of the dispersion is done. Since, following our procedures, this step is done after the calcination, we don't know in which form the rhodium is present in the powder (for example in a nitrate). So to perform this chemisorption, some preliminary steps are needed:

First, a reduction with a stream of hydrogen diluted with an inert (argon) is needed, with a temperature ramp of 7 °C/min starting from ambient temperature to 500 °C, with 60 minutes hold at this temperature. In this way, we are sure that the rhodium is present in its metallic form. However, reaching 500 °C, the hydrogen is chemically bounded to the rhodium now. So, before starting with the chemisorption, we need a desorption with an hot purge, with a flow of inert at 500 °C. The next step is to cool

down the system to the temperature need for the chemisorption (in our case 40 °C). In this condition, there is only Rh on the support.

Now the chemisorption can start. The dispersion is calculated as:

$$\frac{n_{Rh,exposed}}{n_{Rh,total}} \cdot 100 \qquad (2.10)$$

Where $n_{Rh,exposed}$ are the moles of rhodium in the powder, exposed at the surface, while $n_{Rh,total}$ are the total number of moles of rhodium in the powder.

To do this, we need hydrogen pulses (a fixed volume is sent). The hydrogen, also in this case, is diluted in argon. If no hydrogen reacts with the rhodium, all the hydrogen will be seen as a product. If all the hydrogen reacts, no hydrogen will be seen in the products. So consecutive pulses give rise to an increasing trend of hydrogen in the products, since the Rh is becoming saturated. We continue to send pulses until all the hydrogen is found in the product. In this way we know that the Rh is fully saturated. From this signal, through calibration factors, we can found the moles of hydrogen that interacted with the rhodium (from literature we know that we have dissociative adsorption, with one rhodium interacting with only one H from H_2).

In particular, we maintain low temperature during the chemisorption to react only with the Rh in surface, otherwise with high temperatures, the hydrogen will react also with the not exposed rhodium.

Support	Dispersion
Mg-Al_2O_4	67.98%
A-Al_2O_3	23%

Table 2.5: chemisorption results

2.3 Testing

2.3.1 Laboratory scale rig with autothermal reactor

The catalytic partial oxidation experiments were performed in this CPO lab-scale testing rig (Figure 2.11), which for safety reasons is located under fume hood, able to process high flow rate. From the P&ID (Figure 2.12), the rig can be divided into three different sections:

- Feed section
- Reaction section
- Analysis section

The feed section is connected to the reaction one through stainless steel piping system, having a nominal diameter of 1/4 inch, while to reduce dead volumes, the piping of the analysis section has a nominal diameter of 1/16 inch.

Figure 2.11: CPO lab scale rig

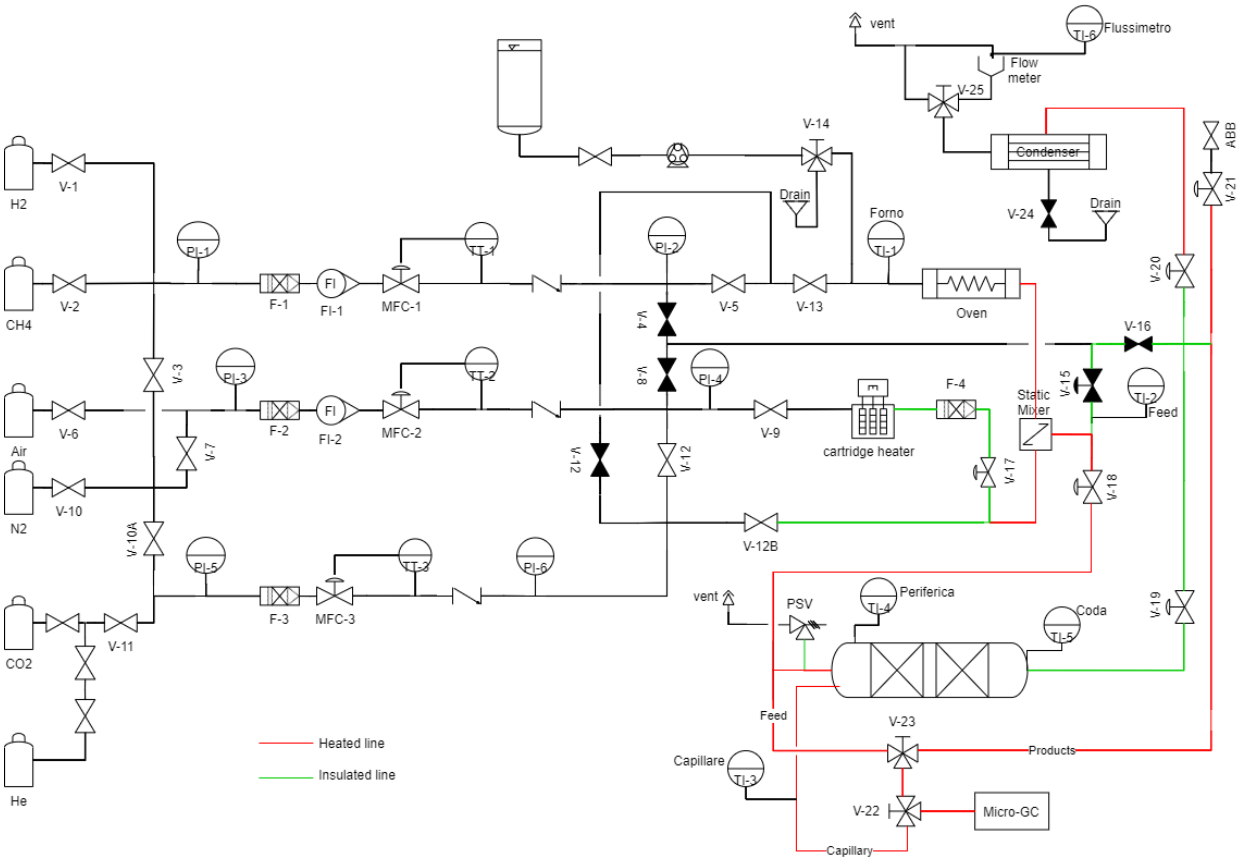

Figure 2.12: P&ID diagram of the system

2.3.1.1 Feed section

The section is composed by four feed lines, through which the reactor can be fed by the following reactants:

- The first line carries hydrogen or compressed methane (purity 99.995%), stored in cylinders outside the laboratory.
- The second line carries air SP (purity 99.5%), stored in cylinders outside the laboratory.
- The third line carries nitrogen, stored in liquid state, in tanks, outside the building or carbon dioxide stored in cylinders outside the laboratory.
- The fourth line carries ethanol (purity 99.5%), stored in liquid state in a burette located under fume hood.

Cylinders are equipped with pressure reducers through which the pressure reduction from the cylinders value (up to 200 bar) to a medium value (5 bar) is realized.

On each gas carrying line, the following elements can be found:

- Shut-off valve of the low-pressure line coming from the cylinders (placed at the beginning of the feeding line).
- Bourdon spring pressure gauge (full scale 6 bar).
- Metal mesh filter (2 μm), to protect the equipment from gas flow impurities.
- Rotameter (only for the first and second lines), which allows a real time evaluation of the flow rate.
- Regulator and flow meter.
- Non-return valve.

Feed streams are regulated by Mass Flow Controllers (MFCs) type 5850S, which are produced by Brooks. MFCs are characterized by the following full scale:

- 15 Nl/min, for MFC1
- 30 Nl/min, for MFC2
- 15 Nl/min, or 1 Nl/min for MFC3.

The first and the second MFC are controlled by PC through the software Brooks Smart Control. As for the last mass flow controller, the 15 Nl/min one is controlled by an analogical knob, while the 1 Nl/min one is controlled with a stand-alone control unit.

For each MFC a calibration line is required: the gas flow rate passing through the MFC can be measured by a bubble flow meter for different openings, thus by performing a linear regression of the data, it is possible to plot the calibration line for each MFC. The openings of the different MFC, that guarantee the desired flow rate is computed starting from the calibration line of each one. Figure 2.13 shows the calibration line obtained for the MFC2 when the processed gas is air.

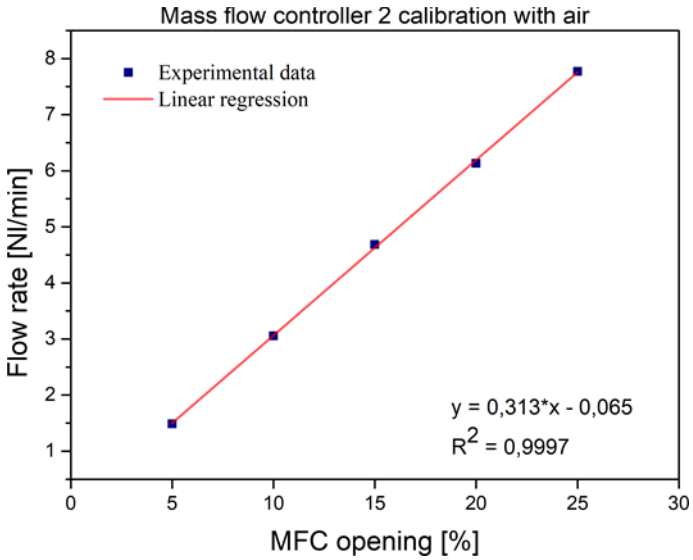

Figure 2.13: Calibration of MFC2 with air: experimental data (dotted blue point) vs. calibration curve (red line)

Liquid fuels are fed from a 250 ml burette, located under hood. The container is connected via Teflon tube (PTFE) to a Gilson MINIPLUS 3 peristaltic pump that conveys the liquids to the reactor. Similarly to the case of MFC, a calibration line is obtained also for the pump in previous thesis work [8], measuring the liquid flow rate corresponding to different values of the pump rotational speed (Figure 2.14).

In each experiment the volumetric flow rate, $\dot{n}_{i,liq}[ml_{liq}/min]$ of the liquids delivered by the pump to the reactor is computed starting from the knowledge of the desired molar flow rate of fuel in gaseous state, $\dot{n}_{i,gas}[Nl_{gas}/min]$, applying the following expression, where MW_i is the molecular mass fuel, $k_{norm} = 22.414\ Nl/mol$, $\rho_i[g/ml]$ is the fuel density and Ƥ is the purity of the fuel.

$$\dot{V}_{i,liq} = \frac{\dot{n}_{i,gas} \cdot MW_i}{k_{norm} \cdot \rho_i \cdot Ƥ} \tag{2.11}$$

Evaluated the required flow rate, the rotational speed of the peristaltic pump is set, starting from the calibration line of the instrument (Figure 2.14).

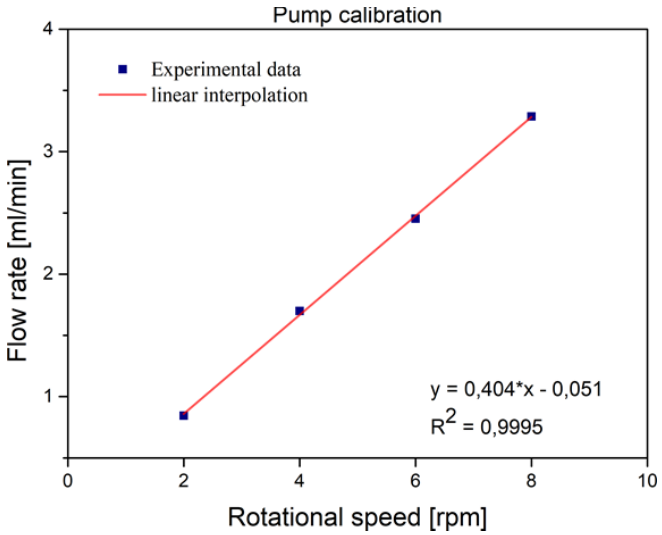

Figure 2.14: Pump calibration curve

During the experiments, the fuel liquid stream is flowing from the peristaltic pump towards a three-way valve (named "V-14" in Figure 2.12) through a 1/16-inch stainless steel line. By means of this valve, it is possible to deliver fuel to the reactor, or, in case of necessity, to a drain point. In order to feed the reactor with required feeding conditions, the liquid fuel is evaporated in an evaporator composed by three independent heating sections. The evaporation process is optimized by the passage inside a 1/2-inch pipe filled by quartz spheres (3 mm diameter) mounted inside the oven. A FeCrAlloy® foam, located at the exit of the furnace prevents the slip of these filling spheres downstream, ensuring at the same time negligible pressure losses. A K-type thermocouple, inserted into a protective sheath, provides the temperature measurement inside the evaporator. The evaporated fuel is then mixed inside the evaporator with a constant stream of 1 NL/min of nitrogen acting as a carrier gas guaranteeing a homogeneous flow. Combustion air and the remaining part of the dilution nitrogen are first pre-heated by a cartridge heater (Watlow Starflow®), whose resistance can be set at maximum temperature of 650 °C, and then joined to the fuel flow in Sulzer® static mixer. It is fundamental to pre-heat the reactant flows before the CPO reactor, in order to ensure the complete vaporization of the liquid feed and avoid any possible condensation along the system lines T^{EtOH} = 78.37 °C. To ensure compliance with these conditions and to avoid any homogeneous reactions before the reactor, during a previous thesis work [8], the following set of temperatures was proposed:

- Heating tape: T = 85 C.
- Heating oven: T = 220 C (for all three different sections).
- Heating cartridge was shut down for this study.

In addition, all the lines downstream the pre-heating system are thermally insulated with a thin ceramic layer of fiberglass and wrapped in a fiberglass tape to minimize heat dispersion. At these conditions, the temperature of the feed, measured by a thermocouple placed between the static mixer and the CPO reactor, is about 100°C. It is important to highlight that in case of methane CPO experiments, both the heating oven and the cartridge are turned off, and this guarantees fully autothermic conditions (T_{feed} = 25 °C).

2.3.1.2 Reaction section

The reaction section is made of an adiabatic reactor, able to process high flow rate. Figure 2.15 shows the reactor assemblage where the catalyst was first loaded in a quartz tube (ID = 25 mm, length = 12 cm) in between two inert monoliths. The front monolith (15 ppi open-cell foam monolith, 1 cm length) was placed 1 cm upstream the catalyst, to promote the reactant mixing. The back monolith (400 CPSI inert cordierite monolith, 3 cm length) was located downstream the end of the catalyst and was used to reduce the axial heat loss. The quartz pipe was then loaded in an AISI 316L stainless steel tube (the vessel of the reactor), equipped with inlet Swagelok fittings and an outlet flange for the connection of the gas lines. Quartz-fiber tape was used to wrap the monolith and prevent any gas leakage in between the monoliths and the quartz tube. External insulation was obtained by a thick layer of wrapped quartz wool. The catalyst loaded in the quartz tube is made of a solid support covered by a wash coat, on which the active phase is dispersed. During this thesis work, 400/7 and 400/9 cordierite honeycomb monoliths, have been used as a support. Rhodium was adopted as an active phase, due to its optimal properties, and was dispersed either on $\alpha-Al_2O_3$, or $MgAl_2O_4$, as it shows better resistance to coke formation [53]. Two K-type thermocouples are present, in order to monitor the inlet and outlet of the flow:

- A peripheral thermocouple, inserted in a position radial to the metal casing, measures the temperature 7 cm before the reactor inlet
- A rear thermocouple measures the temperature of the gases downstream the quartz reactor.

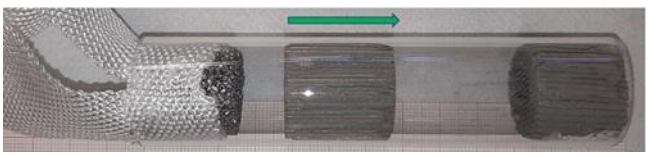

Figure 2.15: Quartz tube reactor assembly

To perform temperature and composition measurements along the axial

coordinate of the reactor, a quartz capillary (Agilent Technology®) coated with polyimide, to confer elasticity and mechanical resistance, is introduced in one of the central channels of the catalyst. The use of fused silica capillary tubes is related to the low catalytic activity of the material, small superficial area to minimize heat losses, and it is essentially transparent to radiation which allow to use a pyrometer to measure the solid phase temperature. This ensures that the function of the capillary is just the protection of the instruments (Thermocouple and Optical fibers) with a negligible impact on the process itself. The temperature capillary (ID 530 μm, OD 670 μm) is sealed at one end through oxyacetylene torch (Kemper® 55H200), to prevent leakages of gas from the reactor. The final part of the capillary is oxidized with butane gas (RS® 513-657) to obtain the desired optical properties and avoid any possible further oxidation during the experiments. While the concentration capillary (ID 200 μm, OD 340 μm) is not sealed at the end, allowing the micro-GC to suck a gas sample from a determined axial coordinate. Figure 2.16 provides an illustration of the system layout.

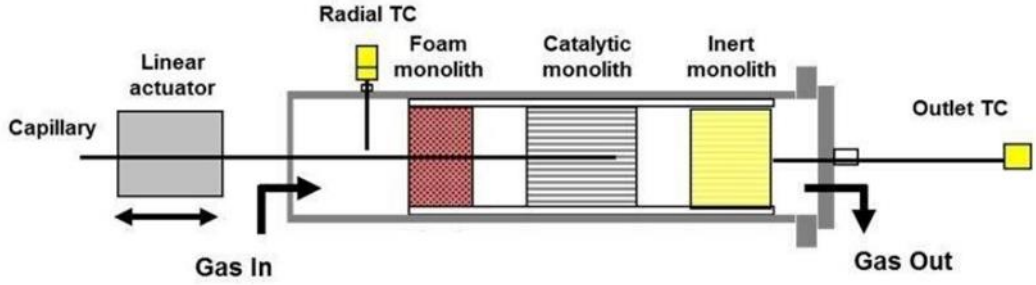

Figure 2.16 : Reactor configuration

2.3.1.3 Analysis section: Spatially resolved sampling technique

In this thesis work, the spatially resolved sampling technique, introduced by Horn et al. [54], has been employed, in order to measure temperature and composition along the reactor axial coordinate, maintaining at the same time adiabatic conditions. A silica capillary, inserted in a channel of the monolith, is fixed on a linear actuator (Zaber® TLA-16) controlled by the computer, with sub- millimetric accuracy. The actuator and the capillary are joined together, allowing the collection of axial temperature profiles of the gas and solid phases by inserting a thermocouple or an optical fiber, respectively, inside the temperature capillary. Alternatively, it is possible to obtain the axial composition profile of the gas flow, connecting the concentration capillary to the micro-GC through 1/16-inch stainless steel line. The importance of this powerful method is emphasized considering that spatial data are much more important than integral steady-state data measured at the outlet, since it is possible to obtain information about the high gradients

located few millimeters after the catalyst inlet, where kinetic phenomena are important.

Solid phase temperature measurement

The acquisition of solid phase temperatures profile has been possible using a pyrometer-optical fiber system, which consist of LumaSense Technologies® IMPAC IGA5 pyrometer which is a digital, compact, and fast infrared measuring instruments for non-contact temperature measurement on metals, ceramics, or graphite. The pyrometer is connected via a digital interface to a computer and data collection is performed with InfraWin® acquisition software. A Polymicro Technologies® optical fiber, with an outer diameter of 370 ±7 μm, is attached to the pyrometer acting as probe allowing the transmission of the radiation emitted by the catalyst surface to the pyrometer. The cone of light that the fiber collects and transmits strictly depends on the shape of the optical fiber's tip (Figure 2.17) where, as reported by Donazzi et al. [13], fibers whose head is 45 ground are preferred for sampling measures, due to their ability of capturing the radiation coming from a specific point of the surface. On the contrary, the use of square tipped optical fibers leads to the underestimation of surface temperature, as an average axial measurement is obtained.

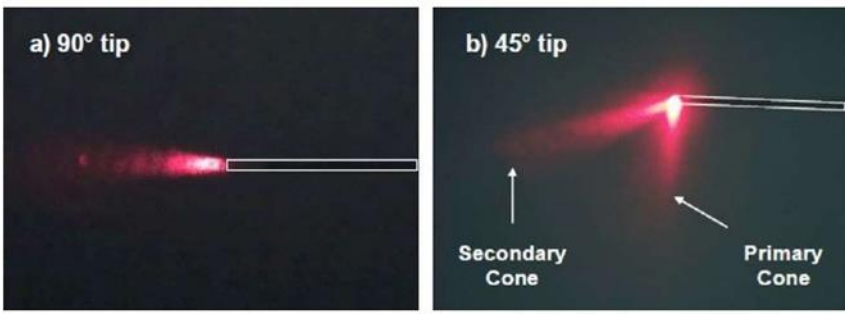

Figure 2.17: Difference between 90 and 45 acceptance cones

The photons detector converts IR radiation into voltage difference, through photovoltaic effect, and acts as an electron counter. Photons coming from the optical fiber impact the surface of the detector, causing a voltage difference proportional to the number of photons involved in the process. According to the following equation, the voltage difference is proportional to the Temperature, elevated to a function that depend again on the temperature, through a constant K, which is function of the pyrometer type, and the surface emissivity:

$$V(T) = \varepsilon_S \cdot K \cdot T^N \tag{2.12}$$

Optical fiber calibration

As the surface emissivity ε_S is an intrinsic characteristic of the target material (the catalyst, in the present case), which depends not only on its roughness but also the geometry of the catalyst support (the honeycomb channel) a calibration is required whenever a new material or a new fiber is tested. The pyrometer was already calibrated against an artificial blackbody source ($\varepsilon_S = 1$) by using the same 45° angled optical fiber that was chosen for the present experimentation and the calibration was in principle needed to determine the emissivity of the supported catalyst. The standard procedure suggests measuring the temperature of the target surface and compare it with that of a reference blackbody source maintained at the same, known, temperature. If a lower temperature than that of the reference is found, the emissivity of the target surface is less than 1 and the emissivity parameter of the pyrometer is adjusted so that the two measurements match. Previous calibrations performed on similar honeycomb monoliths indicated that the geometry of the catalyst support largely determines the radiative behavior of the surface where they performed measurements comparing honeycomb monoliths of different channel dimensions using monoliths that were coated with dull black paint and uncoated monoliths and verified that the honeycomb channel size is the main affecting factor [13]. As reported in this study, a blackbody radiation can be achieved within an isothermal enclosure also in the case of a non-blackbody emitter ($\varepsilon_S < 1$) if proper geometrical conditions are realized: a local apparent surface emissivity ε_A is defined, which is a function of ε_S, of the diameter D of the enclosure and of the distance x of the target from the end section. For cylindrical holes with a surface emissivity larger than 0.6, the apparent emissivity approaches 1 when the ratio between x and D is larger than 6. In practice, unless ε_S is very small, a cavity more than only a few diameters deep emits the same amount of radiation of an infinitely deep cavity and can be approximated as a blackbody. The channels of the honeycomb used in this work (30 mm long and 1.2mm x 1.2mm) guaranteed that a blackbody emissivity could be obtained sufficiently far off the exit section. Following the same calibration procedure used in this study, the pyrometer output was calibrated by Bressan[44] by comparison with thermocouple measurements between 450 and 850 °C, in stagnant air. An inert 400 CPSI cordierite honeycomb (same dimensions of the generally used catalysts in experimental work) was placed in a stainless-steel reactor, externally heated by a tubular furnace. The temperature profiles inside the cordierite channel were collected by inserting both with the optical pyrometer and with the thermocouple alternately in a quartz capillary and by sliding quartz capillary in a central channel of the honeycomb. The capillary was moved exclusively within the channel and strictly isothermal temperature profiles were obtained (±1°C). Indeed,

when setting the input emissivity parameter of the pyrometer at 1, the following linear correlation was derived (valid between 500 and 850 °C):

$$T_{actual} = 0.919 \cdot T_{measured} + 16.61 \quad (2.13)$$

Gas phase temperature measurement

Gas phase temperature profiles are determined thanks to the use of a thermocouple; data are acquired by means of a software from Pico Technology®. A thermocouple consists of a pair of electrical wires of different material contained in a protective sheath. The two conductors are joined together at one end, called the hot junction. When the thermocouple is inserted in the temperature capillary, the cold junction, i.e., the other end of the instrument, is connected to a porcelain terminal block, contained inside a protective head on the linear actuator. When there is a temperature difference between junctions, a voltage difference is detected between the two free ends of the cold junction (Seebeck effect) according to Equation 2.14, where ΔT [K] is the temperature difference between the junctions, V [V] is the electric potential, an [K/V_n] is a parameter depending on the materials used and N [−] is a parameter depending on the desired accuracy. Table 2.6 shows the specification of the thermocouple.

$$\Delta T = \sum_{n=0}^{N} a_n \cdot V^n \quad (2.14)$$

Type	Material	T_{min} [°C]	T_{max} [°C]	Sensibility [μV/°C]	OD [μm]
K	Ni-Cr/Ni-Al	-200	1200	41	250

Table 2.6: Thermocouple properties

Composition measurement

For the analysis of the concentrations, a micro gas chromatograph (Micro GC Fusion® Inficon) is connected via two three-way valves to the feeding, the outlet line of the reactor and to the concentration capillary inserted inside the reactor during concentration tests. This arrangement allows the GC to analyze samples taken upstream, downstream, and localized samples from inside the catalyst channel. To obtain the localized measurements, the capillary is fixed on a linear actuator (Zaber® TLA-16), by knowing the initial position of the capillary, it is possible to construct the composition profile by taking a sample at different points

along the axis of the catalyst.

The Micro GC Fusion® is equipped with two fused silica columns (specifications reported in Table 2.7): Rt®-Molesieve 5A, which uses argon as carrier gas, and Rt®-Q-Bond which uses helium. The use of two different columns in the GC is related to the fact that each column has a limitation towards the species that it can separate. The Rt®-Molesieve 5A is capable of separating H_2, O_2, N_2, CH_4, CO, while the Rt®-Q-Bond is capable of separating CH_4, CO_2, C_2H_x, C_3H_x, H_2O, C_2H_5OH and one peak composed of air, H_2 and CO.

	Rt®-Molesieve 5A	Rt®-Q-Bond
Column Type	Capillary (PLOT)	Capillary (PLOT)
Length [m]	10	12
Diameter [mm]	0.25	0.25

Table 2.7: Inficon MicroGC Fusion Columns specifications

Components separation of a sample injected onto a column is achieved through the interaction between the sample and the column coating. The less retentive the column coating is to a specific compound, the faster compound travels through the column. The two columns installed in the Micro GC are Porous layer open tubular (PLOT) where they have small particles coated on the inner surface of the column and separation is based on gas-solid partitioning. The choice of the type of coating and the length of the columns is particularly important. The coating affects the column's ability to detect certain elements, while the length affects the programming of the temperature ramps. The longer the length of the column, lower is the increase of °C/min.

A thermal conductivity detector (TCD) analyzes the species separated by the micro GC columns. A Wheatstone bridge, Figure 2.18, constitutes this component with two opposite branches lapped by the reference gas and the other two by the stream leaving the columns. When a sample of gas is sent to the TCD, due to the different thermal conductivity of the analyzed species with respect to the reference gas, the temperature of the lapped filaments changes, causing an alteration of the electrical resistance. Equal resistance changes, on two opposite sides, unbalance the bridge, generating an electrical signal that allows the detection of the component leaving the column. Carrier gas must not contain impurities; otherwise, the analysis would be altered. That is why a filter (2 μm) and an O2 trap have been installed on Helium and Argon transportation lines. Carrier gases are available at 4 bar, as suggested

by the manufacturer, to guarantee the exact functioning of the gas chromatograph.

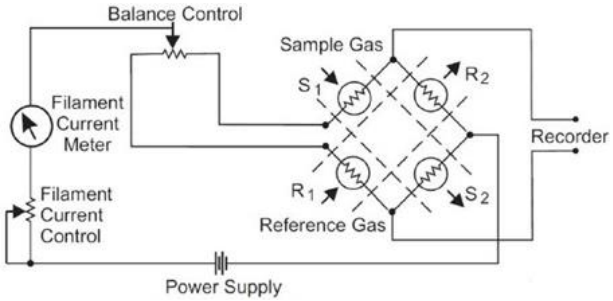

Figure 2.18 : TCD scheme

Gas chromatograph analysis gives as a result a chromatogram, which shows the voltage signal (expressed in μV) provided by the TCD as a function of time. Each voltage peak is caused by the detection of a species, characterized by a certain retention time, dependent just on the physical properties of the considered species. The separated sample elutes from the GC column and enters the detection subsystem, where an electrical signal is generated based on compound type concentration. A data system controls the GC and processes the detector signal output for the sample being analyzed. As compounds elute from the GC column and are detected, a chromatogram is displayed with the detector response on the y axis and retention time on x axis.

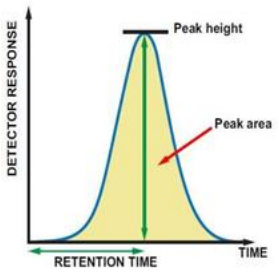

Figure 2.19: Micro gas chromatograph response

The area under each peak is proportional to the amount of species detected. It is possible to convert the areas into species concentrations, introducing the response factors. The response factor relative to a generic i-species is defined as follows:

$$\alpha_i = \frac{\dot{n}_i}{\dot{n}_{N_2}} \cdot \frac{A_{N_2}}{A_i} \tag{2.15}$$

For a correct evaluation of α, the following procedure has to be followed: the flow analyzed by the Micro GC is composed by a diluent phase of a reference gas and

species whose inlet and outlet molar flows are known (internal standard method). Nitrogen has been chosen to be the reference gas. For each αi the mixture analyzed has a different concentration of the species of interest to create a calibration curve of the response factor. To create the different concentration the volumetric flow of the reference gas is varied, and the flow rates of the other species are maintained constant. This because the interference of the reference gas on the measurement is lower. The evaluation of the flow rate is done with the use of a bubble flow meter. The Micro GC response factors used in this study can be found in Table 2.8.

Species	Column	Carrier	α_i
H_2	Rt®-Molesieve 5A	Ar	0.09
O_2			0.867
N_2			1
CH_4			0.477
CO			1.075
Air + CO + H_2	Rt®-Q-Bond	He	-
CH_4			0.915
CO_2			0.719
C_2H_4			0.6232
C_2H_6			0.581
H_2O			1.420
C_3H_6			0.432
C_2H_4O			0.409
C_2H_5OH			0.378

Table 2.8: Inficon Micro GC Fusion® response factors

As previously mentioned, Rt®-Q-Bond column does not separate nitrogen. One peak is identified, associated to air, H_2, CH_4 and CO. On the other hand, the Molecular sieve column is able to separate these species, so it is possible to

compute the relative ratios between the considered species and identify the fraction of the peak area of the Rt®-Q-Bond column associated to nitrogen (Equation 2.16). The response factors of the species separated by Rt®-Q-Bond column are referred to that fraction of the pseudo-peak associated to nitrogen.

$$A_{N_2}^{U} = \frac{A_{Pseudo}^{U}}{1 + \frac{A_{CO}^{S} \cdot \alpha_{CO}^{Ar}}{A_{N_2}^{S} \cdot \alpha_{CO}^{He}} + \frac{A_{O_2}^{S} \cdot \alpha_{O_2}^{Ar}}{A_{N_2}^{S} \cdot \alpha_{O_2}^{He}} + \frac{A_{H_2}^{S} \cdot \alpha_{H_2}^{Ar}}{A_{N_2}^{S} \cdot \alpha_{H_2}^{He}}} \tag{2.16}$$

Each analysis produces two chromatographs, one from each column. Qualitative results are converted in quantitative ones, knowing the response factors of each species, the flow of nitrogen and the value of every area detected:

$$\dot{n}_i = \frac{\alpha_i \cdot \dot{n}_{N_2} \cdot A_i}{A_{N_2}} \tag{2.17}$$

Then, the molar flow rate in mol/min of each species is computed according to the following equation:

$$F_i = \frac{\dot{n}_i}{k_{norm}} \tag{2.18}$$

Consequently, it is possible to evaluate the molar fraction of each species in the mixture at the outlet of the reactor:

$$y_i = \frac{F_i}{\sum F_i} \tag{2.19}$$

Eventually, reactant conversion and selectivity of each species referred to C-molar flow and H-molar flow are calculated:

$$\chi_{fuel} = 1 - \frac{F_{fuel,out}}{F_{fuel,in}} \tag{2.20}$$

$$\chi_{O_2} = 1 - \frac{F_{O_2,out}}{F_{O_2,in}} \tag{2.21}$$

$$S_{i,C} = F_{i,out} \cdot \frac{nC_i}{F_{C,unconverted}} \tag{2.22}$$

$$S_{i,H} = F_{i,out} \cdot \frac{nH_i}{F_{H,unconverted}} \tag{2.23}$$

To verify the quality of each analysis, atomic balances, referred to carbon, hydrogen and oxygen are defined, they should be as much as possible close to unity:

$$B_C = \frac{\sum F_{i,out} \cdot nC_i}{F_{C,unconverted}} \tag{2.24}$$

$$B_H = \frac{\sum F_{i,out} \cdot nH_i}{F_{H,unconverted}} \tag{2.25}$$

$$B_O = \frac{\sum F_{i,out} \cdot nO_i}{F_{O,unconverted}} \tag{2.26}$$

Analysis methods and the output chromatogram

Table 2.9 shows the used analysis method parameters for column A (Rt®-Molesieve 5A) and for column B (Rt®-Q-Bond) exploited both for the ethanol and methane tests. As shown from Figure 2.20, the ethanol method also includes a temperature ramp which allows better identification of the species.

Method	Ethanol chain		Methane chain	
Column	A	B	A	B
T_{column} [°C]	70	ramp	70	60
$T_{injector}$ [°C]	100	100	100	100
Pressure [psi]	25	25	25	25
Injection time [ms]	160	100	160	80
Sample pump [s]	60	60	60	60
Analysis time [s]	180		150	

Table 2.9: Micro GC method parameters EtOH and CH_4 CPO test

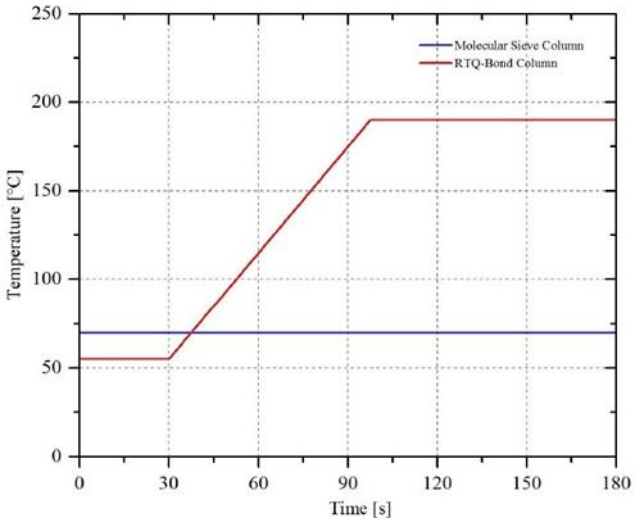

Figure 2.20: Micro GC columns temperatures during ethanol analysis method

The output chromatogram of a methane characterization test, as shown in Figure 2.21 and Figure 2.22, identify the different peaks related to the different components:

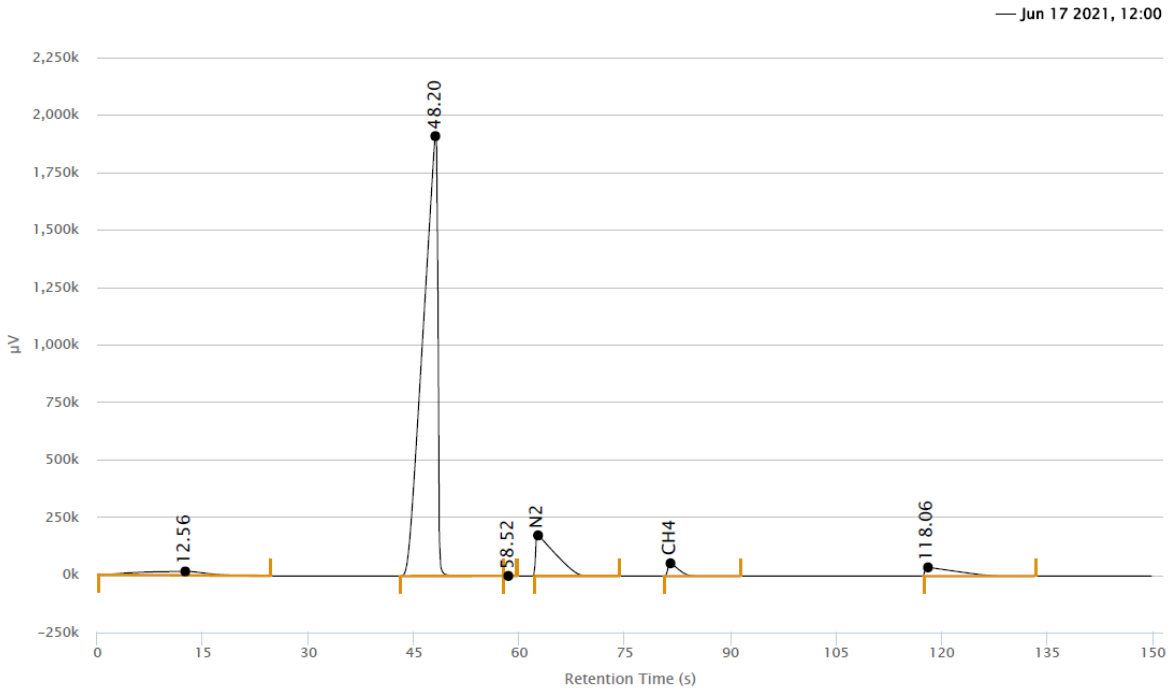

Figure 2.21: Column A Micro GC chromatogram methane test

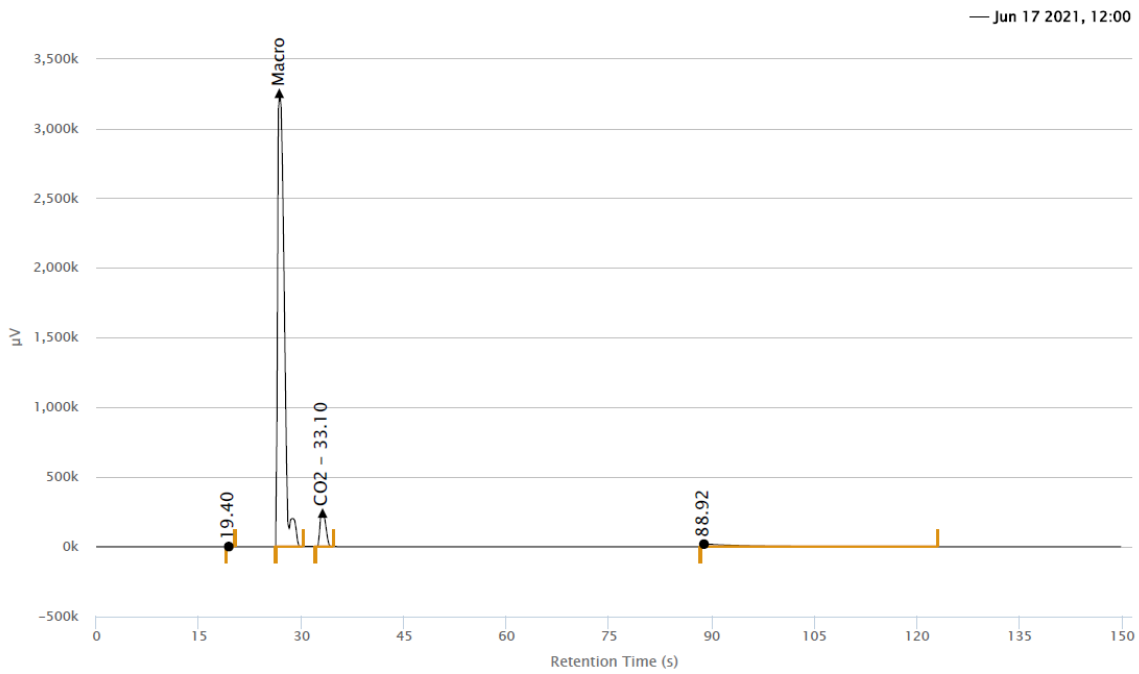

Figure 2.22: Column B Micro GC chromatogram methane test

2.3.2 Laboratory scale rig with isothermal microreactor

2.3.2.1 Description

The experimental tests in the scope of this thesis work on heterogeneous catalytic processes have been carried out by a testing unit which works completely under laboratory fume hood. The rig setup consists of three main parts which are connected by 1/4-inch stainless steel pipelines:

- feed section.
- reaction section.
- analysis section

The rig set-up used in the experiments is seen in Figure 2.23.

Figure 2.23: The experimental testing unit

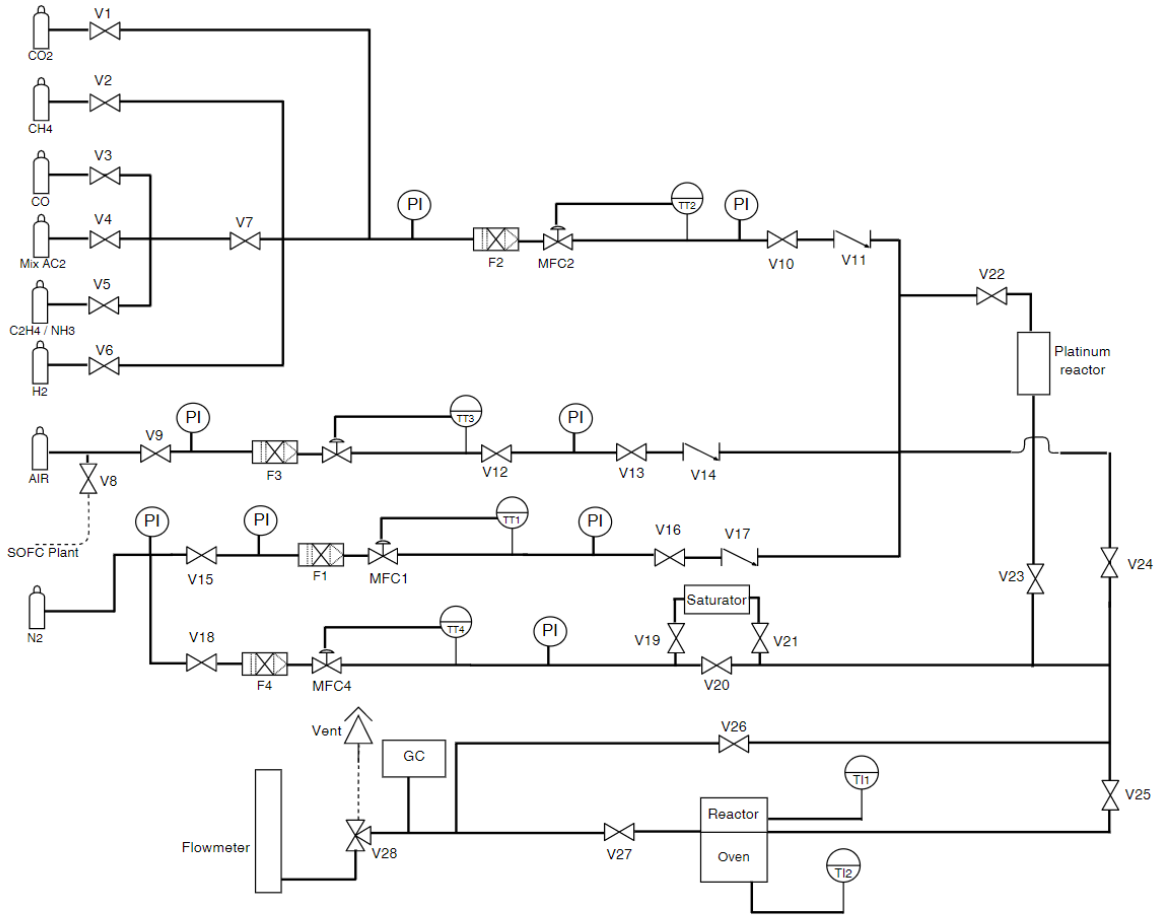

Figure 2.24: P&ID diagram of the plant

Feed section

The reactants for these experiments are mostly gaseous species. However, ethanol and sometimes water were stored in liquid phase. They required different procedures and the use of a saturator. The reactant gases come either from cylinders placed outside the laboratory (CH_4), from dedicated cylinders appositely moved in the laboratory (NO_2, N_2O in diluted mixture) or from common cylinders placed in the basement of the building (air, H_2); finally, the nitrogen (N_2) comes from a tank placed outside the building where it is kept liquid. For each gas, there is an inlet steel line and a thermo-regulated valve which enables to decrease the pressure from the cylinder (100-200 bar) to the line one (4-5 bar).

The rig has six lines whose diameters are either 1/4 inch or 1/8 inch: three lines used for fuels or co-feeding (mostly for CH_4 and H_2), the air feed line and two nitrogen lines (complementary N_2 and N_2 sent to the saturator). Each line has its own electronic mass

flow controller (MFC, model Brooks 5850S). The MFC employed for most of the experiments were:

- gaseous fuels line (CH_4, H_2) provided with a 1 NL/min MFC
- air line provided with a 200 NmL/min MFC
- saturator nitrogen line provided with a 100 NmL/min MFC
- complementary nitrogen line provided with a 3 NL/min MFC.

Moreover, for each line there are:

- an inlet valve to separate the lines and avoid back-flow
- two Bourdon spring gauges (6 bar) upstream and downstream of the Brooks to control its operation
- a metal mesh filter (7 μm) to protect the instruments from impurities in the gases
- at least one interception valve before and after the MFC.

Also in this rig each mass flow controller must be manually calibrated for each different species which passes through it. An example is seen in Figure 2.25.

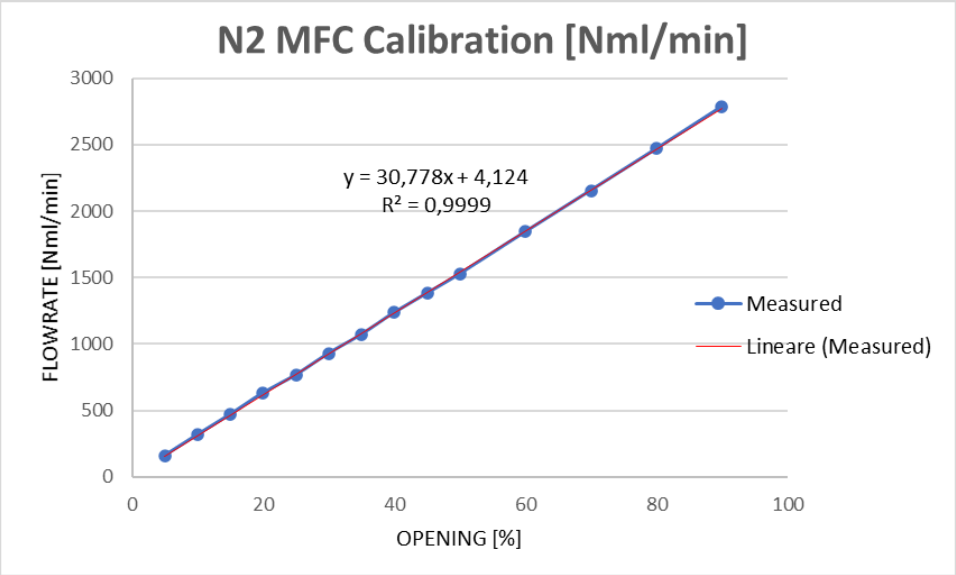

Figure 2.25: Example of calibration curve for the nitrogen

Differently from the other rig, liquid reactants like ethanol were fed to the system as a vapor using a saturator, which is a small vessel filled by the liquid as seen in Figure 2.26. Saturator is equipped with inlet and outlet lines to which the saturator nitrogen line is connected. The inlet one arrives below the free level of the liquid and makes the

N_2 flow passing through the liquid inside before it exits: in this way a part of the liquid evaporates and it is dragged by the N_2 flux, so that it is in saturated conditions at the outlet.

Figure 2.26: Saturator Setup

The vapor pressure of the liquid species is found by the semi empirical Antoine's law:

$$p_i^0(T) = exp\left(A_i + \frac{B_i}{T + C_i}\right) \tag{2.27}$$

Ai, Bi, Ci are empirical coefficients specific for each chemical component as given in Table 2.10.

Species	A_i	Bi	C_i
C_2H_5OH	8.1122	1592.864	226.184
H_2O	4.6543	1435.264	-64.848

Table 2.10: Coefficients of the Antoine's law for the considered species, where T is expressed in K and p is expressed in atm [55]

Since the saturator and the rig are operated at atmospheric pressure, the partial pressures of each species are calculated according to the ideal gas model below,

$$y_i = \frac{p_i^0(T)}{p} \tag{2.28}$$

Consequently, the flow of the evaporated species expected at the outlet of the saturator is found by,

$$F_i = \frac{y_i}{1 - y_i} F_{N_2} \tag{2.29}$$

The amount of liquid that evaporates in the saturator depends on both N2 flux and temperature. Therefore, it is really important to monitor the temperature and keep it constant during the test. For this reason, an electric heating plate regulated by a T-control is placed under the saturator. Moreover, the saturator is placed inside a becker filled by water which is thermally homogenized by magnetic stirrer during the day in order to exploit high thermal capacity of water to avoid possible temperature oscillations.

Reaction Section

All the lines converge into a unique line, which is afterwards splitted into two streams: the reactor stream and the bypass stream. A small packed-bed reactor seen in Figure 2.27, containing a platinum-based catalyst is placed on the upstream of this splitting. This reactor is taken into operation for some of the steam reforming and water co-feeding experiments for water synthesis by letting the hydrogen, air, and complementary nitrogen streams flow across the catalytic bed. During this synthesis, the nitrogen coming from the air and the complementary line are employed to reach an appropriate dilution of the H_2-O_2 mixture to keep it far from the flammability limits. The flow coming from the saturator line bypasses this reactor and is then mixed with its outlet stream in order to avoid reactions between H_2, O_2 and the liquid fuel before the injection to the main reactor. When water is not required among the reactants stream this reactor is not taken into operation and is bypassed by all the lines.

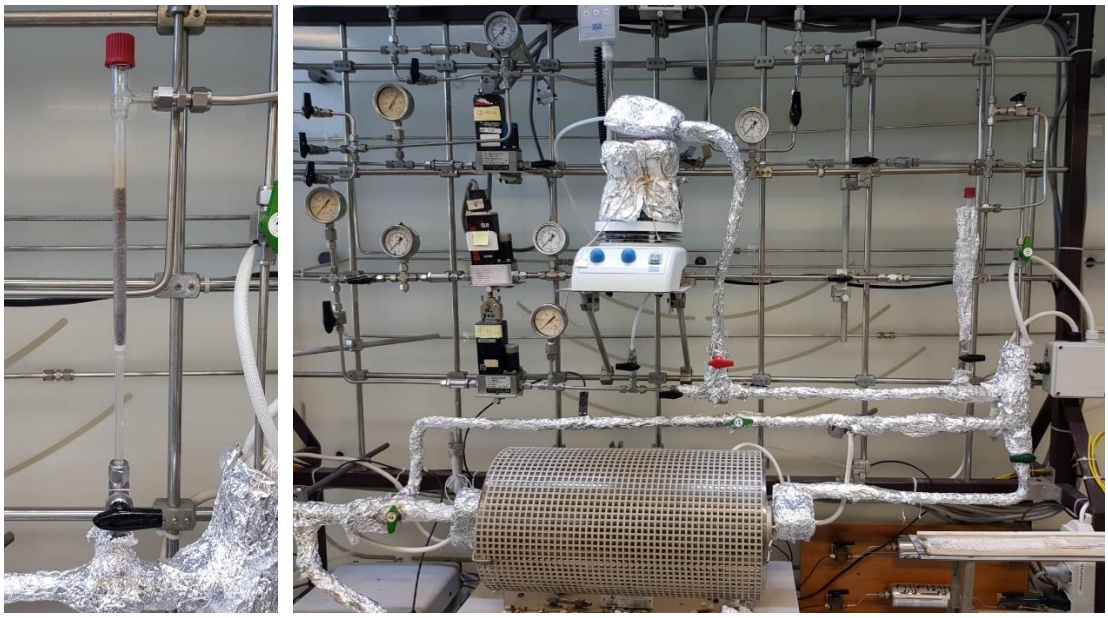

Figure 2.27: Pt-reactor adopted for water synthesis (left) and its insulated state inside the rig (right).

Both the main reactor and the bypass streams are heated up by electric resistances starting from the outlet of saturator and the platinum-based reactor up to the outlet of the rig, kept at 120-130°C to avoid any condensations in the lines. Both lines are equipped with an upstream shut-off valve, while the reactor has one also downstream which prevents reactant backflow from the bypass and allows the reactor to be completely isolated.

These two lines meet again at the downstream of the main reactor and converge towards a two-way valve: this allows the gas to be sent to the vent or alternatively to a bubble flowmeter to be used to measure the molar flows manually.

The main reactor consists of a quartz cylinder tube with an inlet and an outlet for the gases in which a high purity alumina tube (99.8%) is inserted, coated with a thin layer of catalyst with a known length and mass. It is shown in Figure 2.28. In this way, annular flow can be obtained in the reactor, and this guarantees different benefits compared to traditional packed bed reactors:

- less diffusive limitations both intra-phasic (the catalytic layer is thin) and inter-phasic (the thickness of the annular section is reduced to about 0.5 mm)
- the possibility to use higher spatial velocities, or Gas Hourly Space Velocity (GHSV), and studying fast reactions limited by equilibrium

- possibility to directly measure the temperature of the catalytic layer since it is very thin, and it is possible to consider it in thermal equilibrium with the alumina tube
- high capacity for heat dissipation by irradiation combined with the high dilution in nitrogen (90-95% N2) with the advantage of the possibility to conduct experiments that allows limited axial temperature gradients; the reactor can be considered substantially isothermal.

These characteristics of the annular reactor allow to study the kinetics of very fast and not thermodynamic equilibrium-limited reactions such as the combustion of hydrocarbons at high temperatures that occurs during the CPO.

The reactor is inserted in a cylindrical furnace with three zones Carbolite TZF 12/38/400 of internal diameter 6 cm and length 45 cm. The two lateral electric resistances work together with the central one to keep the set temperature uniform over the entire length of the oven and the temperatures of each zone are monitored by PID regulators that use N-type thermocouples as sensors.

Two K-type thermocouples (600 mm long and 1 mm in diameter) are made to slide inside the alumina tube placed next to the reactor and inside the oven environment as illustrated in Figure 2.29. In this way it is possible to measure the temperature profiles along the axial axis of catalytic bed and the corresponding internal oven environment.

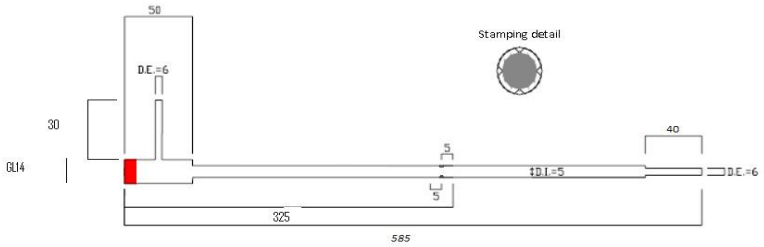

Figure 2.28: Scheme of cylindrical annular reactor.

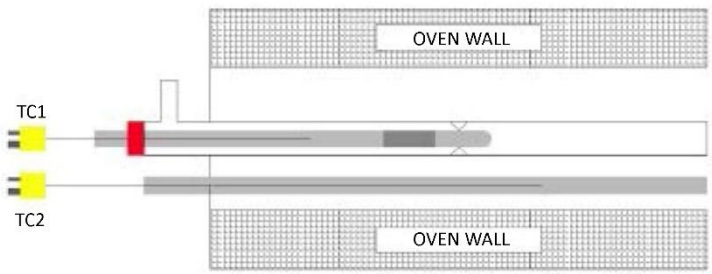

Figure 2.29: Diagram of the thermocouples inserted in the reactor and the oven.

Analysis section

The analysis of the composition of the gaseous flows is performed by means of a micro gas chromatography, shown in Figure 2.30. A sample of the mixture is aspirated and inserted through an injector into a capillary column, inside which a transport gas (or "carrier") flows. The column is covered internally by a solid species that has different affinities with the different molecules passing through it. The solid tends to form chemical bonds with the gases, but these are re-brought into the solution by the carrier gas. The final effect is a slowdown of the species and the greater is the gas-solid affinity, the greater is the slowing down effect. Therefore, they will come out of the column separated and at different times. At the exit of the column a TCD (Thermal Conductivity Detector) is placed. It consists of a Wheatstone bridge in which a resistance is connected to a flow of carrier only, another to the flow coming out of the column. If the two resistances are run over by flows with different thermal conductivity they will be cooled differently and due to the dependence of the resistivity from the temperature, there will be a variation of the voltage in time that is measured by a sensor. The resulting voltage signal is called chromatogram. Figure 2.31 shows an example of a chromatogram produced by the micro gas chromatograph for an analysis during an experiment with ethanol.

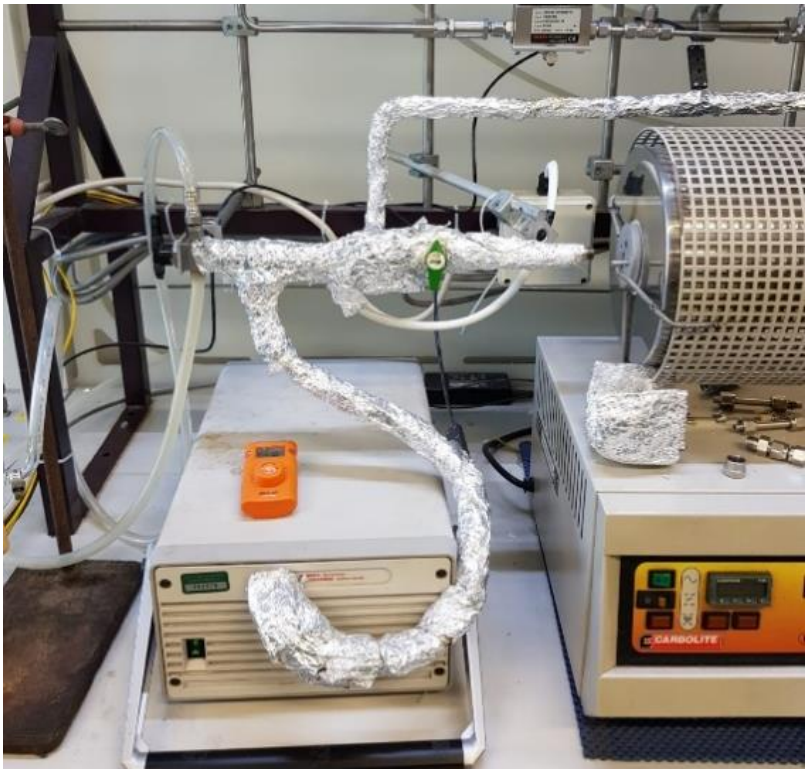

Figure 2.30: Gas chromatography as a part of the rig

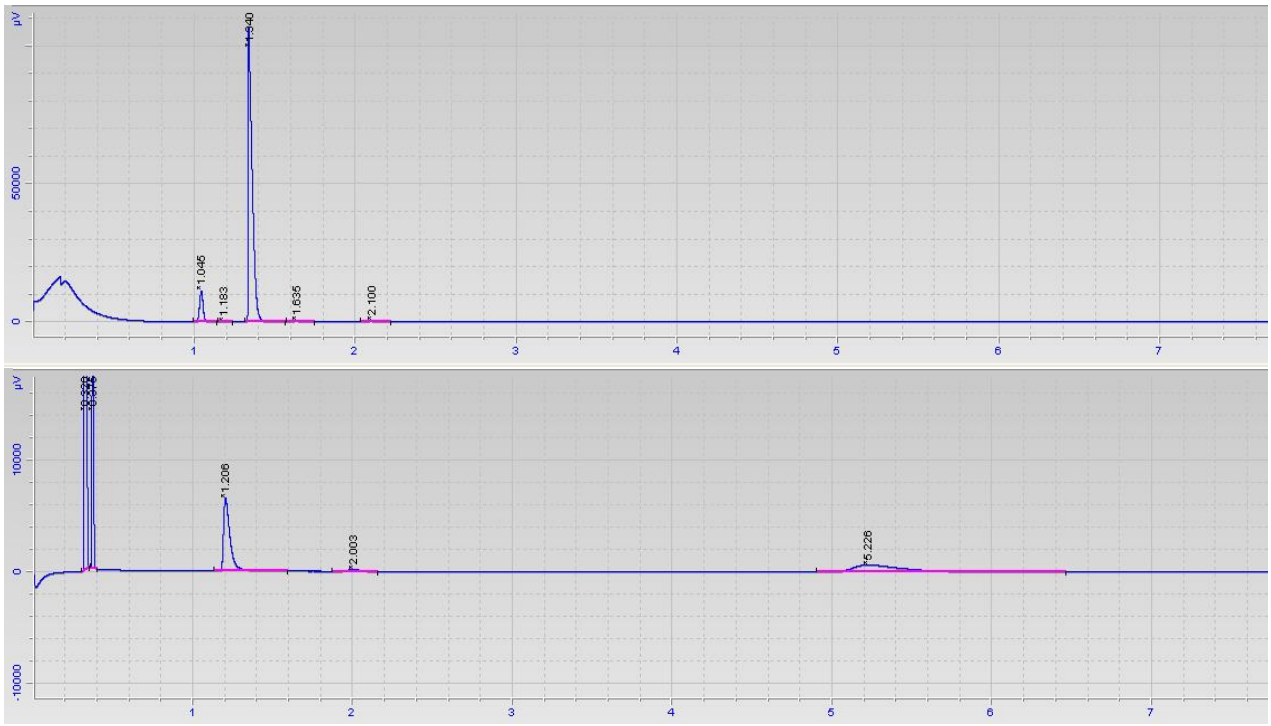

Figure 2.31: Chromatogram examples

Since the species have been previously separated in the column, each of them is associated with a peak in the voltage signal and the area underneath is proportional to its quantity. However, as told before, to convert areas into concentrations it is necessary to introduce αi, response factors, which are defined as in Equation 2.15.

The response factors, obtained from a gas chromatograph calibration, establish a direct proportionality between the flows and the areas, therefore they allow to evaluate the flows of each species knowing the flow of nitrogen. Some of the response factors used are shown in Table 2.11 respectively and the characteristics of the analysis methods used in the experiments are given in Table 2.12.

Column	Species	α_i
B (Plot U)	$O_2 + N_2 + CO$	1
	CH_4	0.43
	CO_2	0.66
	C_2H_4	0.888
	C_2H_6	0.777
	H_2O	2.12
	HCOOH	0.7757
	C_2H_4O	0.777
	C_2H_5OH	0.699
A (Molecular sieves)	H_2	0.088
	O_2	0.94
	N_2	1
	CH_4	0.43
	CO	1.057

Table 2.11: Response factors of some species

Method	Etanolo2		SR_Oxygenates	
Column	A	B	A	B
T column [°C]	90	90	90	160
T injector [°C]	100	100	100	100
Pressure [psi]	29	20.30	29	35
Injection time [ms]	30	30	30	10
Analysis time [s]	480	480	300	300

Table 2.12: Characteristics of analysis methods

In the rig, an Agilent 3000A micro-gas chromatograph equipped with two capillary columns is installed as shown in Figure 2.32: column B (PlotU) uses helium as carrier, while column A (molecular sieves) uses argon. The characteristics of the columns are shown in Table 2.13. In order not to alter the analysis, the transport gas must not contain impurities. Therefore, water and oxygen traps and dust filters have been installed upstream of it.

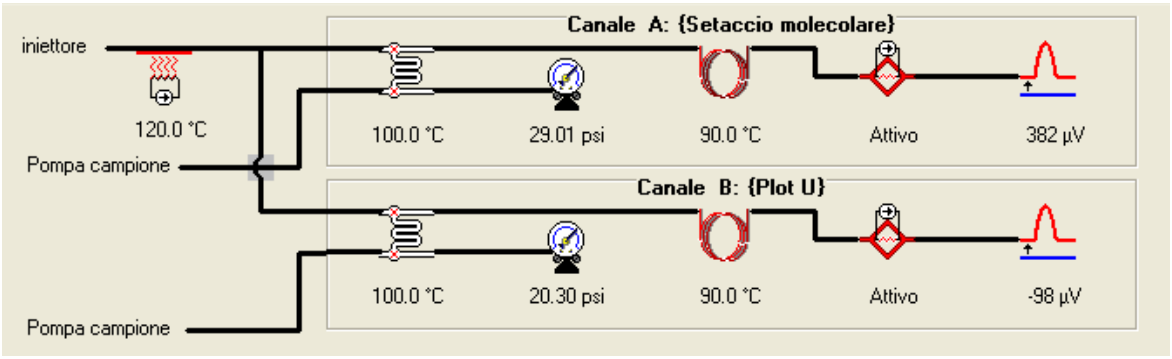

Figure 2.32: Operating scheme of the gas chromatograph.

	A (Molecular sieves)	B (Plot U)
Column type	capillary	capillary
Length [m]	10	8
Diameter [cm]	0.32	0.32
Carrier	Ar	He
Column T_{max} [°C]	180	160

Table 2.13: Characteristics of gas chromatograph columns

2.3.2.2 Experimental procedures

Start-up of the rig

The first operation before starting any experiment in the rig is the start-up of the suction hood to avoid gas leakage to the working environment. Then, the reagent cylinders placed outside the building and the valves placed upstream and downstream of the pressure reducer are opened. The reducer is typically set to 4 bar for ordinary gases and 5.5 bar for transport gases. Next, the shut-off valves are opened at the entrance to the system. At this point, before sending any gas through the pipelines, the electrical resistances that surround the lines and the related thermo-controllers, the oven (which is set to the desired set point), and the mass flow controller should be opened together with the one of the TCDs which is controlled by setting the analysis method through the computer. Micro-gas chromatograph is always kept opened

Flow measurements by the flow meter

Once the heating elements have reached the operating temperature, the gases used in the experiment are sent through the bypass line while the reactor valves are fully closed. The desired flow rate of each gas is set by adjusting proper openings of Brooks flowmeters. Each flowrate is then also measured by means of a bubble flow meter as an additional check. For using the bubble flow meter, it is necessary to turn the three-way valve to the direction of the flow meter from direction of the vent. Time measurements are taken with a chronometer (sensitivity 0.01 s) and an average of

measurements is calculated. To bring the measurement unit back to NmL, the flow temperature is also measured. Then the flow rate is given by the equation:

$$\dot{N}_i \ [NmL/min] = \frac{V_{misurato} \ [mL]}{t_{medio} \ [min]} \frac{273.15}{T_{misurata} \ [K]} \tag{2.30}$$

This procedure is repeated for each gas flow.

Implementation of the experiment

The reagent lines and the relative mass flow controllers are opened keeping the mixture always above the upper flammability limit. For example, in the methane CPO it will be necessary to first open the nitrogen, then the methane and finally the oxygen. Then the analysis of the flow of reagents is performed through the GC to verify the consistency between the flows measured at the flowmeter and those calculated by the analyses. If these two flows are matched, the valves upstream and downstream of the reactor are opened and the valve on the bypass is closed and thus sending the reactants to the reactor. When the oven has reached the set point temperature in a stable way (waiting time is about half an hour), the analysis of the products leaving the reactor is carried out at the GC. To reduce the experimental error, an average of three different analyses is calculated for each temperature point. The tests are carried out from a starting temperature ranging from 100-300°C up to 750 - 850°C with the intervals of mostly 50°C (sometimes shorter intervals like 20-40°C, depending on the experiment). For each test the temperature profiles are measured along the axis of the furnace manually.

Shut down of the rig

Once the tests are finished, the oven set point is lowered to zero. When the temperature on the screen starts decreasing, the oven can be switched off. The mass flow controllers and shut-off valves are then closed in reverse order with respect to the opening in order not to fall within the flammability range. However, the nitrogen is left open for a few minutes and allowed to flow into the reactor to clean it. After that, the reactor is isolated by opening the bypass valve and closing the downstream valve first and then upstream in order to leave it under slight nitrogen pressure. At this point, flow controllers and the valves on the nitrogen lines can be closed. Then, it is possible to close the system inlet valves, the ones straddling the pressure reducer and finally the external tanks of the reagents. The socks (the lines heating elements) and the hood are switched off. Finally, the micro-GC is left in the shut-down method which is called as "spegnimento". Periodically it is necessary to perform the conditioning of the micro-GC that is the cleaning of the columns from reagents eventually remaining inside,

bringing the columns to high temperature and making helium and argon flow for 8-12 hours with the TCD filaments turned on.

2.3.2.3 Experimental data processing

Every test carried out for this thesis work involved the measurement of temperature profiles and of composition of the output flow. Since for each experiment a certain temperature range was investigated, steady-state measurements were repeated for every set point temperature imposed on the oven. In this paragraph the post-processing of collected experimental data and the way of presenting results are described.

Calculation of molar flows starting from chromatographic analyses

The composition of the mixture coming out from the quartz reactor, hence corresponding to the composition reached at the outlet section of the catalytic layer (if accepted that no homogenous reactions take place downwards), was measured at every temperature step of each test, starting from the chromatographic analyses. The procedure here described was used to estimate the molar flow rate of each species in the mixture.

The areas under the peaks of the chromatogram are proportional to the volume flow rate of the corresponding species, according to a correction factor which depends on the sensibility of the detector towards the specific component. This factor must be evaluated during the calibration procedure. It is necessary to choose a reference species, used to normalize all the other measurements. Nitrogen, an inert species present in large excess in all the tests of this thesis work, was used as reference. Nitrogen peak is detected by both the columns of the gas chromatograph. However, Column B does not separately detect N2, O2 and CO and combines them in a single macro-peak. Therefore, to isolate them, it is necessary to resort to the signal of column A and to evaluate the fraction of the area under the macro-peak owning to nitrogen:

$$x_{areaN_2} = \frac{A^A_{N_2}}{A^A_{N_2} + A^A_{O_2} + A^A_{CO}} \tag{2.31}$$

An average fraction on three consecutive chromatographic analyses is evaluated, in order to have a solid estimate:

$$x^{average}_{areaN_2} = \frac{x^{analysis\,1}_{areaN_2} + x^{analysis\,2}_{areaN_2} + x^{analysis\,3}_{areaN_2}}{3} \tag{2.32}$$

The area of the apparent nitrogen in signal B can be therefore calculated:

$$A^{B}_{N_2\ app} = A^{B}_{macro} * x^{average}_{area N_2} \tag{2.33}$$

Since nitrogen is the reference species, it is necessary to use its area to normalize the areas under the peaks of all the other components detected by the gas chromatograph. For the signals of column B the apparent nitrogen area just calculated is used, while for column A the measured nitrogen area is directly employed:

$$f_i = \frac{A_i}{A_{N_2}} \qquad column\ A \tag{2.34}$$

$$f_i = \frac{A_i}{A^{B}_{N_2\ app}} \qquad column\ B \tag{2.35}$$

Again, for each species the average ratio is then estimated:

$$f_i^{average} = \frac{f_i^{analysis\ 1} + f_i^{analysis\ 2}\ f_i^{analysis\ 3}}{3} \tag{2.36}$$

It is also necessary to estimate the response factor α_i of each species: this parameter account for the different sensitivity of the detector towards a specific component when compared to the reference (whose response factor is fixed to 1). During the calibration procedure, a mixture with known composition is sent to the gas chromatograph and response factors are estimated. Since these factors depend on the temperature of the analysis and on the composition of the mixture that reaches the chromatograph, the calibration procedure must be carried out in conditions similar to the system of interest.

Once all $f_i^{average}$ and α_i are known, it is possible to evaluate the flowrate ($\dot{\mathrm{N}}_i$, Nml/min) of each species using the following equation:

$$\dot{\mathrm{N}}_i = f_i^{average} \alpha_i \dot{\mathrm{N}}_{N_2} \tag{2.37}$$

The flowrate of nitrogen is calculated with the following equation, where the total flow (measured at the flowmeter) is used:

$$\dot{\mathrm{N}}_i = \frac{\dot{\mathrm{N}}_{TOT}}{\sum_{i=1}^{NS} f_i^{average} \alpha_i} \tag{2.38}$$

where NS = total number of species.

Molar fractions can be evaluated as follows:

$$y_i = \frac{\dot{N}_i}{\dot{N}_{TOT}} \tag{2.39}$$

Conversions of reactants j are defined as:

$$\chi_j = \left(\frac{\dot{N}_j^{in} - \dot{N}_j^{out}}{\dot{N}_j^{in}} \right) * 100 \tag{2.40}$$

Carbon and hydrogen selectivities are also evaluated. Carbon selectivity towards product species i is given by:

$$\sigma_{C,i} = \frac{\dot{N}_i^{out} * n_{C,i}}{\dot{N}_{C,conv}} * 100 \tag{2.41}$$

where $n_{C,i}$ = number of carbon atoms in species i and $\dot{N}_{C,conv}$ accounts from the carbon atoms that passed from reactants' molecules into products' molecules:

$$\dot{N}_{C,conv} = \sum_{j=1}^{NR} \left(\dot{N}_j^{in} - \dot{N}_j^{out} \right) * n_{C,j} \tag{2.42}$$

where NR = number of reacting species.

Finally, it is important to evaluate the material balance of carbon atoms, in order to see if any carbon deposition is taking place or if the feeding mixture is changing.

$$B_C = \frac{\sum_{i=1}^{NS} \dot{N}_i^{out} * n_{C,i}}{\sum_{i=1}^{NS} \dot{N}_i^{in} * n_{C,i}} \tag{2.43}$$

Temperature profiles

Two thermocouples are employed to measure the temperature steady-state axial profile on the catalyst side and on the oven side at every temperature step of each test. Measurements were performed every 2 mm along the length of the catalytic layer. Moreover, some measurements were done also upstream and downstream with respect to the catalytic bed, in order to complete the analysis and to better check the absence of homogeneous reactions in these zones.

The annular reactor employed for this thesis work can often be approximated as isothermal: this assumption is considered true when the axial temperature gradient does not exceed 5 °C/cm. This hypothesis is not strictly verified in all the tests carried out. For this reason, the measurement of these profiles is meaningful. Furthermore, for the purposes of graphic representation of composition results, it is convenient to use

an average temperature value, which hence must be estimated from the entire axial profile. To this purpose, the algebraic average of the temperatures measured on the catalytic bed is considered.

Presentation of the results

Conversion of reactants and composition of the outlet product mixture (expressed in terms of molar fractions of its components) were represented as function of the average measured temperature for each experimental test. Hence, plots with temperature on the abscissa and conversion/molar fraction on the y axis were drawn. In these graphs, dashed lines correspond to values estimated at the thermodynamic equilibrium. The Stanjan code [56] was used to evaluate the equilibrium composition of a mixture. Temperature and pressure are given as input values to the program.

In addition to these graphs, temperature profiles were plotted as function of the axial coordinate, in order to well visualize the axial trend. The results are reported as ΔT between reactor and oven for a dual purpose. On one side, in this way the profiles measured for different set point temperatures can be put together in the same plot to be easily compared. Secondly, this is the most effective way to detect exothermic and endothermic phenomena.

2.3.2.4 Description of the operating condition of the experiments

The general conditions related with the experiments performed for this thesis work are described here. However, some of these parameters were adjusted by the purpose of the specific study. All tests were carried out at atmospheric pressure and by making a temperature climb from 100-300°C to 700-850°C at intervals of mostly 50°C (sometimes less/ more than 50°C) and speed 10°C/min.

Catalytic Partial Oxidation tests (CPO) of methane and ethanol

The typical conditions of the tests are:

- fuel fraction calculated to have a 3% molar of carbon in feed, O_2 at 1.68% ($O_2/C = 0.56$) and N_2 to complement
- GHSV was ranged from 2.5×10^5 NL/ (kg_{cat} h) to 2×10^6 NL/ (kg_{cat} h) depending on the specific test.

Oxygen is supplied by the flow of air. The dilution nitrogen is fed by the appropriate line, while the fuel is fed from a gas line or from a saturator if liquid. Methane as a fuel is supplied from a 20% nitrogen-diluted or as pure methane cylinder.

Steam Reforming tests (SR) of ethanol

The standard test conditions are:

- fuel fraction calculated to have a 3% molar carbon, H2O at 3% (Steam/C=1) and complementary nitrogen
- GHSV ranging from 5×10^5 NL/ (kg_{cat} h) to 1.5×10^6 NL/ (kg_{cat} h).

The dilution nitrogen is fed by the appropriate line, while the water is generally produced in a platinum-based reactor upstream of the main reactor by feeding H_2 and O_2. To avoid contamination of the test it is necessary to make the oxygen react completely, therefore an excess of 5% of H_2 is used. This excess is then subtracted from the experimental curves, so that they represent only the net production of hydrogen due to reforming. Ethanol was stored liquid in the saturator, where a stream of N_2 was sent as done in CPO tests.

Steam Reforming tests (SR) of methane

The standard test conditions are:

- fuel fraction calculated to have 1% molar carbon, H2O from 1.5% to 4.5% (Steam/C=1.5-4.5) and complementary nitrogen
- GHSV fixed at 1.0×10^6 NL/ (kg_{cat} h).

In these experiments, methane was taken from the bottle outside the lab and sent as a gaseous fuel, while water was fed using the saturator. Hence, in this case, Pt-reactor was not employed

2.4 Mathematical model of the annular reactor

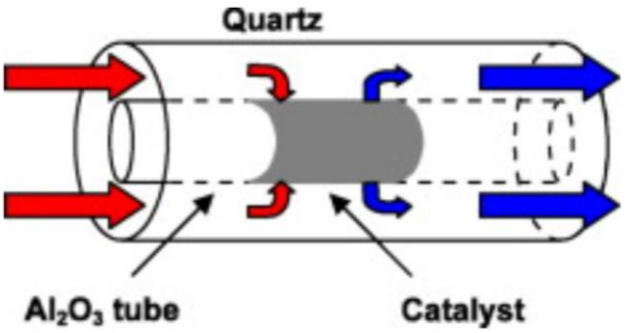

Figure 2.33: Scheme of the annular reactor

For the kinetic analysis of the experiments obtained in the annular reactor, an existing one-dimensional heterogeneous model was used. This model was developed in

previous works [12][66][67] and applied to the development of kinetic schemes of catalytic partial oxidation and steam reforming of hydrocarbons and oxygenates on a Rh-Al_2O_3.

The model consists of the differential mass balances for the reacting species (bulk phase) coupled with continuity equation (gas-solid interface) and is based on the following assumptions:

- Ideal plug-flow conditions for gas phase
- Isothermal condition, where the temperature on the catalytic bed is set equal to that of the gas phase
- Laminar flow
- Radial concentration gradient limited to an infinitesimal layer next to the catalytic bed: hence, only the bulk concentration in the gas phase (C^B) and at the gas-solid interface (C^W) must be considered in the description of the radial profile
- Negligible axial diffusion in the gas phase, due to high Péclet number.

In this thesis work, the reactor model, coupled with independently developed CPO and SR kinetic schemes for CH_4 and EtOH over Rh/Al_2O_3 were used to comparatively analyze the performance of Rh/Mg-Al_2O_4.

2.4.1 Description of the model

Equations

Given these assumptions, it is possible to evaluate the concentration profile along the axis of the annular reactor of a reacting system with NS species by means of 2*NS unknown variables. They are the NS species molar concentration in the gas phase x_i^B and the NS species molar concentration at the gas-solid interface x_i^W. Pressure and temperature are fixed and homogeneous. Hence, it is necessary to write 2*NS independent equations to solve this system.

NS equations are the plug flow mass balances used to model the gas phase species, expressed in dimensionless form.

$$Pe_{m,i}\frac{dF_i^*}{dz^*} = -\frac{4}{1+\frac{1}{R^*}}Sh_{loc,i}(x_i^B - x_i^W)\frac{F_{TOT}}{F_{TOT}^0} \tag{2.44}$$

With $F_i = F_i^0 @ z^* = 0$ as an inlet condition, where the dimensionless axial coordinate $z^* = \frac{z}{D_{hydr}}$, dimensionless molar flowrates $F_i^* = \frac{F_i}{F_{TOT}^0}$ and the geometric dimensionless parameter for annular section $R^* = \frac{D_i}{D_{out}}$ are employed. The hydraulic diameter is

defined as $D_{hydr} = D_{out} - D_{in}$. Given NA as the number of atomic species present in the system, it is possible to substitute NA of these first order differential equations with other NA atomic balances, that are linear first order algebraic equations. Thus, they would lead to a meaningful simplification of the model. The atoms present in the systems analysed here are carbon, hydrogen and oxygen, and the atomic balances are the following.

$$\sum_{i=1}^{NS} (F_i - F_i^0) n_{C,i} = 0 \tag{2.45}$$

$$\sum_{i=1}^{NS} (F_i - F_i^0) n_{H,i} = 0 \tag{2.46}$$

$$\sum_{i=1}^{NS} (F_i - F_i^0) n_{O,i} = 0 \tag{2.47}$$

The remaining NS constraints are provided by the steady-state equations of mass continuity between the catalytic wall and the bulk gas phase, where the radial mass flow of each species is equated to its overall formation/consumption rate.

$$Sh_{loc,i}(x_i^B - x_i^W) = \sum_{j=1}^{NR} \nu_{i,j} \alpha_i r_j \tag{2.48}$$

Where NR is the total number of reactions and the adaptive parameter α_i is defined as follows:

$$\alpha_i = \frac{D_{hydr} m_{cat}}{S D_i C_{TOT}} \tag{2.49}$$

Since the gas mixture can be considered ideal, the total concentration can be evaluated through the ideal gas law: $C_{TOT} = \frac{P}{RT}$.

Molecular diffusivities D_i are evaluated with the Fuller-Schettler-Giddings correlation, adopting the approximation of binary diffusivities of each species in N_2 [69][69]. The terms of reaction rates are described in the following paragraph.

Both inter-phase and intra-phase mass transfer limitations are taken into account by the model, so that it is possible to decouple each contribution from intrinsic reaction kinetics. The equations used to consider mass transfer resistances are described in next paragraphs.

The final system of 2*NS equations must be solved with numerical methods to simulate the profile of NS x_i^W and NS x_i^B along the axial coordinate of the annular reactor.

Inter-phase mass transfer limitations

Inter-phase limitations are accounted for using the local Sherwood number $Sh_{loc,i}$, whose expression has already been used in literature to interpolate the exact solution of Graetz-Nusselt problem inside channels with different types of section [70], [71], then adapted to annular geometry with third type boundary conditions [72].

$$\frac{K_{c,i}d_h}{D_i} = Sh_{loc,i} = Sh_{inf} + 6.874e^{-71.2z_{Sh_i}}\left(1000z_{Sh_i}\right)^{-0.35} \tag{2.50}$$

Where the dimensionless axial coordinate z_{Sh_i} is defined as $z_{Sh_i} = \frac{z^*}{Pe_{m,i}}$ and correspond to the Graetz coordinate. The value of Sh_{inf} is defined with the following expression for the annular duct.

$$Sh_{inf} = Sh_{circ} - 1.7548R^* \tag{2.51}$$

Where $R^* = \frac{R_{int}}{R_{out}}$ of the annular duct.

Intra-phase mass transfer limitations

Intra-phase mass transfer resistances are accounted for using generalized efficiency factors for each reacting species, hence methane and oxygen for methane CPO, methane and water for methane SR. The same can be said for the CPO and SR of EtOH.

Considering as example the efficiency of O_2, it is defined as:

$$\eta_{O_2} = \frac{\tanh\left(\Phi_{O_2}\right)}{\Phi_{O_2}} \tag{2.52}$$

Where Φ_{O_2} is the Thiele modules for oxygen. This value accounts for the ratio between intrinsic reaction rate and internal diffusional rate. In this context, it is calculated as follows.

$$\Phi_{O_2} = \frac{1}{\eta_{O_2}^{\infty}} \tag{2.53}$$

Where Bishoff correlation is used to evaluate $\eta_{O_2}^{\infty}$:

$$\eta_{O_2}^{\infty} = \frac{\sqrt{2}}{\delta_L r_{O_2} c_{O_2}^S} \sqrt{\int_0^{c_{O_2}^S} D_{eff,O_2} r_{O_2}(C) dC} \tag{2.54}$$

Wakao-Smith random pore model[73] is exploited to express the effective diffusivities.

$$D_{eff,i} = \epsilon_M^2 D_{M,i} + \frac{\epsilon_\mu^2 (1 + 3\epsilon_M)}{1 - \epsilon_M} D_{\mu,i} \tag{2.55}$$

Where $D_{M,i}$ and $D_{\mu,i}$ are respectively the macroporous and microporous diffusivity of species i. The following values were assigned to the morphological features of the catalyst: average macropore diameter $D_{Macro} = 200\ nm$, average micropore diameter $D_{Micro} = 500\ nm$, macro-void volume percentage $\epsilon_M = 5\%$, micro-void volume percentage $\epsilon_\mu = 55\%$. These values have been estimated by N_2 adsorption/desorption and Hg intrusion. A sensitivity analysis was performed on these parameters to evaluate the role of the catalytic layer morphology on the results. Also the thickness of the catalytic layer was assumed constant and it was evaluated taking into account the volume occupied by the catalyst:

$$\delta_L = \sqrt{\frac{m_{cat}}{\rho_{cat} \pi L_{cat}} + \left(\frac{D_t}{2}\right)^2} - \frac{D_t}{2} \tag{2.56}$$

Internal mass transfer limitations, if it is present, are accounted for by the model by multiplying each intrinsic reaction rate for the internal efficiency factor.

Kinetic model of methane and Ethanol conversion to CO/H_2.

The overall rate of production of a species is r_i, defined as:

$$r_i = \sum_{j=1}^{NR} \nu_{ij} r_j \tag{2.57}$$

Where r_j is the expression of rate of reaction j and ν is the stoichiometric coefficient of the species I in the reaction j.

In previous studies, kinetic models have been developed to describe the processes of CPO and SR of several fuels.

An indirect-consecutive reaction scheme is assumed: it consists of a step of total oxidation followed by a subsequent steam reforming. The C1 scheme also includes post combustion of CO and H_2, methanation from CO, water gas shift (WGS) and

reverse water gas shift (RWGS). We herein illustrate the kinetic scheme for methane and ethanol.

Reaction	**Reaction rate r $\left[\frac{mol}{g_{cat}s}\right]$**
CH_4 total oxidation $CH_4 + 2O_2 \rightarrow CO_2 + H_2O$	$r_{ox,CH_4} = \frac{k_{ox,CH_4} P_{CH_4}}{1 + k_{ads,H_2O} P_{H_2O}} \sigma_{O_2}$
CH_4 steam reforming $CH_4 + H_2O \leftrightarrow CO + 3H_2$	$r_{SR,CH_4} = \frac{k_{SR,CH_4} P_{CH_4} \left(1 - \eta_{SR,CH_4}\right)}{1 + k_{ads,CO} P_{CO} + k_{ads,O_2} P_{O_2}} \sigma_{H_2O}$
Water Gas Shift $CO + H_2O \rightarrow CO_2 + H_2$	$r_{WGS} = \frac{k_{WGS} P_{H_2O} (1 - \eta_{WGS})}{1 + k_{ads_{H_2O}} P_{H_2O}} \sigma_{CO}$
Reverse Water Gas Shift $CO_2 + H_2 \leftrightarrow CO + H_2O$	$r_{RWGS} = k_{RWGS} P_{CO_2} (1 - \eta_{RWGS}) \sigma_{H_2}$
Methanation from CO $CO + 3H_2 \leftrightarrow CH_4 + H_2O$	$r_{met} = k_{met} P_{H_2} (1 - \eta_{met}) \sigma_{CO}$
H_2 oxidation $H_2 + \frac{1}{2} O_2 \leftrightarrow H_2O$	$r_{ox,H_2} = k_{ox,H_2} P_{H_2} \sigma_{O_2}$
CO oxidation $CO + \frac{1}{2} O_2 \rightarrow CO_2$	$r_{ox,CO} = k_{ox,CO} P_{CO} \sigma_{O_2}$
EtOH oxidation $C_2H_5OH + 3O_2 \rightarrow 2CO_2 + 3H_2O$	$r_{TO} = \frac{K_{TO} P_{O2}}{\left(1 + K_{adsO2} \frac{P_{O2}}{P_{ETOH}}\right)^2}$

EtOH steam reforming $C_2H_5OH + H_2O \rightarrow 4H_2 + 2CO$	$r_{SR,EtOH} = \frac{k_{SR_{EtOH}} P_{EtOH}(1-\eta_{SR})}{1+\frac{k_C P_{EtOH}}{P_{H2O}}}$
EtOH decomposition $C_2H_5OH \rightarrow CH_4 + CO + H_2$	$r_{DEC} = K_{DEC} P_{ETOH} \sigma_{O2}$
EtOH oxidative dehydrogenation $C_2H_5OH + \frac{1}{2}O_2 \rightarrow C_2H_4O + H_2O$	$r_{oxdeH2} = k_{OxdeH2} \cdot \frac{k_{ads,O2,ace} \cdot P_{O2}}{1 + k_{ads,O2,ace} \cdot P_{O2}}$

Table 2.14: Stoichiometry and expressions of reaction rate employed in the kinetic model of methane/EtOH CPO/SR

As told before in the CPO of methane, seven reactions are present. The total oxidation of methane to CO_2 and H_2O,which is an exothermic reaction; the methane steam reforming to CO and H_2 which is endothermic; the post-combustion of CO and H_2 that are exothermic reactions; The methanation from CO, exothermic, giving methane and water as products; water gas shift (WGS), exothermic, which from CO and water produce carbon dioxide and hydrogen; and reverse water gas shift (RWGS) that is the opposite reaction compare to the WGS. About the latter ones, WGS and RWGS have independent kinetics, that have been developed to describe conditions for the equilibrium.

Dry reforming stoichiometry is not considered, because data can be properly simulated without its inclusion [22], as CO_2 consumption observed at high temperature is due to RWGS, which is thermodynamically favoured in this temperature range.

Concerning the conversion of ethanol, the kinetic scheme consists of: ethanol oxidation, ethanol SR, ethanol decomposition and ethanol oxidative dehydrogenation.

Stoichiometry and relative kinetic expressions of these reactions are listed in Table 2.14. It can be noticed that methane total oxidation reaction rate depends on the partial pressure of the methane but not on the oxygen concentration as experimentally proven[74]. The overall reaction order of the CH_4 oxidation reaction is lower than one, where the competitive adsorption of water on active sites of the catalyst is accounted for. Similarly, steam reforming reaction rate has a linear dependence on methane partial pressure, while it is not influenced by water concentration as a result of the

competitive adsorption of CO and O_2 taken into account in the term at the denominator. WGS, RWGS, methanation and post combustion of CO and H_2 have a kinetic of first order of the reactant in excess (respectively, H_2O, CO_2, H_2, CO and H_2). These correlations are found in [12], [22].

Reaction rates limited by the equilibrium are multiplied by the term $(1-\eta_j)$, which accounts for the slowing down effect when the reaction is approaching the thermodynamic equilibrium. Coefficients η_j comprise the extent of reaction j with respect to its equilibrium value:

$$\eta_j = \frac{K_{p,j}}{K_{eq,j}} \tag{2.58}$$

Where $K_{p,j} = \prod_{i=1}^{NS} P_i^{\nu_{ij}}$ and $K_{eq,j} = \exp\left(-\frac{\Delta G_j^0}{RT}\right)$, the equilibrium constant.

Details about thermodynamic calculation are reported in Section 2.4.2

Coefficients σ_i are necessary to account for the extinction of the co-reactant, when the reaction rate is independent from its concentration. The numerical tolerance was chosen between 10^{-6} and 10^{-20} depending on the conditions in order to guarantees numerical convergence.

$$\sigma_i = \frac{P_i}{P_i + 10^{-6}} \tag{2.59}$$

Reaction rate constants k_j are evaluated with the modified Arrhenius equation:

$$k_j(T) = k_j\left(T_{rif,j}\right)\exp[-\frac{E_{att,j}}{R}\left(\frac{1}{T}-\frac{1}{T_{rif,j}}\right)] \tag{2.60}$$

A similar expression is used for thermodynamic adsorption constants:

$$k_{ads,i}(T) = k_{ads,i}\left(T_{rif,ads,i}\right)\exp[-\frac{\Delta H_{ads,i}}{R}\left(\frac{1}{T}-\frac{1}{T_{rif,ads,i}}\right)] \tag{2.61}$$

The values of coefficients appearing in these equations are reported in Table 2.15 and in Table 2.16.

Reaction	$k_{rif,j}\ \left[\frac{mol}{atm\ g_{cat}\ s}\right]$	$E_{att}\ \left[\frac{kJ}{mol}\right]$	$T_{rif,j}\ [K]$
CH_4 total oxidation	2.00×10^{-2}	92	773
CH_4 steam reforming	2.00×10^{-2}	92	773
Water Gas Shift	6.24×10^{-2}	25	873
Reverse Water Gas Shift	4.20×10^{-3}	62	773
Methanation from CO	0	88	773
H_2 oxidation	6.67×10^{-4}	62	313
CO oxidation	1.74×10^{-2}	76	523
EtOH oxidation	2.00×10^{-1}	70	473
EtOH steam reforming	4.00×10^{-1}	90	873
EtOH decomposition	5.00×10^{-3}	40	623
EtOH oxidative dehydrogenation	1.11×10^{-3}	98	523

Table 2.15: Coefficients for the calculation of kinetic constants of the reactions present in the model

Adsorbed Species	$k_{rif,ads,i}\ \left[\frac{1}{atm}\right]$	$\Delta H_{ads,i}\ \left[\frac{kJ}{mol}\right]$	$T_{rif,ads,i}\ [K]$
O_2 (CH_4 test)	1.4	-23	873
O_2 (EtOH test)	5.461	73	873

H_2O	25	-57	773
CO	410	-37	773
H_2	190	-30	773

Table 2.16: Coefficients for the calculation of adsorption constants present in the model

2.4.2 Thermodynamic calculations

Introduction

Steam reforming and partial oxidation of ethanol involve complex mechanisms and numerous species can be produced. On the other hand, even if the decomposition mechanism of formic acid is simpler due to its C1 property, several species are present at equilibrium.

The equilibrium composition was evaluated for all the tests reported in this thesis. the dashed lines present in composition plots represent the equilibrium condition. For these calculations, Stanjan code[56] was used, inserting the temperature, pressure and initial composition of the system as input data. The identification of products and reactants was required. For the case of ethanol, the catalytic partial oxidation process can be considered as the combination of oxidation and steam reforming reactions, in the presence of oxygen defect compared to complete combustion. For steam reforming (SR), hydrogen, carbon monoxide, carbon dioxide, methane, acetaldehyde, residual ethanol and water are considered here as possible products, as reported in previous thermodynamic studies [75]. For the case of CPO, oxygen is another species in addition to the steam reforming ones. On the other hand, in the case of formic acid, the species taken into account for equilibrium calculations are hydrogen, carbon monoxide, carbon dioxide, methane, residual formic acid and water. Ethylene and, moreover, solid carbon (graphite) are not considered in these calculations. Hence, to complete this analysis, the thermodynamic study of these processes has been completed by minimizing the Gibbs global energy of the system. For the sake of brevity, these results are not reported here.

Minimization of Gibbs free energy

The equilibrium compositions are calculated through the minimization of Gibbs free energy of the system. Matlab® software was used for these calculations. The thermodynamic and physicochemical properties involved in the calculations were selected from [55]and reported in Table 2.17 and Table 2.18.

The specific heat is calculated as follows, where T is expressed in K:

$$c_p\left[\frac{J}{mol*K}\right] = A + B \times T + C \times T^2 + D \times T^3 \quad (2.62)$$

Species	Enthalpy of formation (ideal gas) [J/mol] (298 K)	Entropy of formation (ideal gas) [J/mol*K] (298K)
Ethanol C_2H_5OH	-2.35e5	280.64
Formic Acid HCOOH	-3.786e5	248.70
Acetaldehyde C_2H_4O	-1.644e5	264.2
Ethane C_2H_6	-8.474e4	229.12
Water H_2O	-241814	188.72
Carbon dioxide CO_2	-393510	213.68
Carbon monoxide CO	-110530	197.56
Methane CH_4	-74520	186.27
Oxygen O_2	0	205.149
Nitrogen N_2	0	191.61
Hydrogen H_2	0	130.57

Table 2.17: Enthalpy and entropy of formation of different species.

Species	A	B	C	D
Ethanol	9.014	2.141e-1	-8.39e-5	1.373e-9
Acetaldehyde	7.716	1.823e-1	-1.007e-4	2.38e-8
Ethane	5.409	1.781e-1	-6.938e-5	8.713e-9

Water	32.220	1.9225e-3	10.548e-6	-3.5940e-9
Carbon dioxide	19.78	73.390e-3	-55.98e-6	17.14e-9
Carbon monoxide	30.848	-12.84e-3	27.870e-6	-12.71e-9
Methane	19.238	52.09e-3	11.966e-6	-11.309e-9
Oxygen	28.087	-0.0042e-3	17.447e-6	-10.664e-9
Nitrogen	31.128	-13.556e-3	26.777e-6	-11.673e-9
Hydrogen	27.124	9.267e-3	-13.799e-6	7.64e-9

Table 2.18: Coefficients for the calculation of specific heat at constant pressure.

The calculation of the equilibrium composition refers to specific conditions of T, P and feed composition. At equilibrium condition, the total free energy (4.2) of the system at those constant T and P must be minimized.

$$G = \sum G_i \times n_i = \sum \mu_i \times n_i \qquad (2.63)$$

Where G_i [J/mol] is Gibbs partial free energy of species *i*, μ_i [J/mol] the chemical potential of species *i* and n_i number of piers of species *i*.

In this thermodynamic analysis, the ideal gas state is considered because the critical pressure of reactants and products is much higher than the operating pressure (1 atm). The critical properties of the compounds involved in the analysis are listed in Table 2.19.

Species	Critical Temperature [K]	Critical pressure [bar]
Ethanol	514	61.37
Formic Acid	588	58.10
Acetaldehyde	466	55.5

Ethane	305.32	48.72
Water	647,13	219,4
Carbon dioxide	304,21	73,9
Carbon monoxide	132,92	34,9
Methane	190,564	45,9
Oxygen	154,58	50,2
Nitrogen	126,2	33,9
Hydrogen	33,19	13,2

Table 2.19: Critical temperatures and pressures of the species of interest.

According to Lewis equation, the chemical potential is expressed as:

$$\mu_i(T,P,y) = \mu_i\left(T,P_{ref}\right)^* + RTln\left(\frac{f_i}{f_i^0}\right) \quad (2.64)$$

Where: $\mu_i(T,P,y)$ and and $\mu_i\left(T,P_{ref}\right)^*$ [J/mol]are the chemical potential of species i, evaluated at the actual state of the system at temperature T, pressure P and composition y, and at reference state respectively, while f_i and f_i^0 are the actual and reference fugacity of species i. The chosen reference state is pure ideal gas, at P_{ref} = 1 atm.

The general expression of the fugacity of a species in the gas phase is the following:

$$f_i(T,P,y) = P \times y_i \times \Phi_i^v(T,P,y) \quad (2.65)$$

Where $\Phi_i^v(T,P,y)$ is fugacity coefficient of species i in a system at temperature T, pressure P and molar composition y.

Approximating the system as an ideal gas mixture, the fugacity coefficient is unitary and the fugacity is reduced to the partial pressure of the i-th species. The expression of chemical potential becomes:

$$\mu_i(T,P,y) = \mu_i\left(T,P_{ref}\right)^* + RTln\left(\frac{P * y_i}{P_{ref}}\right) \tag{2.66}$$

The chemical potential at reference conditions $\mu_i(T,P_{ref})^*$ can be expressed as:

$$\mu_i\left(T,P_{ref}\right)^* = h_i\left(T,P_{ref}\right) - Ts_i\left(T,P_{ref}\right) \tag{2.67}$$

Where h_i [J/mol] and s_i [J/mol/K] are the molar enthalpy and molar entropy of species i.

Summing up the chemical potentials, Gibbs global free energy will be a function to be minimized by using the codes developed on Matlab®. The constraints of minimization are the atomic balances applied to carbon, hydrogen and oxygen.

$$\sum k_{i,j} * n_i^0 = \sum k_{i,j} * n_i \tag{2.68}$$

Where $k_{i,j}$ represents the number of j atoms (j=C, H, O) in species i, while n_i^0 and n_i are the number of moles of species i in the initial state and at thermodynamic equilibrium respectively. Another constraint is that the number of moles of each species at equilibrium cannot be less than zero.

In the model, $K_{eq,j}(\tilde{T})$ is the equilibrium constant of reaction j at a certain temperature can be calculated as follows:

$$K_{eq,j}\left(\tilde{T}\right) = \prod_{i=1}^{n} a_i{}^{\nu_i j} \ @\ equilibrium \tag{2.69}$$

Where a_i are the activities of the species i at equilibrium, $\nu_{i,j}$ are the stoichiometric coefficient of the species i in reaction j.

The equilibrium constant $K_{eq,j}(\tilde{T})$ can be also expressed as follows:

$$K_{eq,j}\left(\tilde{T}\right) = \exp\left(-\frac{\Delta G_{R,j}^0\left(\tilde{T}\right)}{R\tilde{T}}\right) \tag{2.70}$$

Where $\Delta G_{R,j}^0\left(\tilde{T}\right)$ is the standar-state free energy of reaction j at temperature $\tilde{T}$.

By calculating the equilibrium conditions at varying temperature, a linearized correlation for the $\Delta G^0_{R,j}(\tilde{T})$ can be derived, such that:

$$\Delta G^0_{R,j}(\tilde{T}) = A_j + B_j\tilde{T} \tag{2.71}$$

Parameters A_j and B_j were evaluated for those reactions limited by equilibrium and present in the kinetic scheme described in Table 2.11: CH4 SR, WGS, ethanol SR, methanation of CO.

3. Role of the active phase support on the CPO of ethanol in autothermal conditions

CPO of hydrocarbons and oxygenates has been studied for small scale production of hydrogen intensively in the recent years. With the aim of providing insights about the performance of the process in a commercial application, the adiabatic lab scale rig presented in section 2.2 was used to test the catalytic performance of coated honeycomb monoliths. The rig equipped with the spatially resolved sampling technique allows the measurement of the temperature of the solid and gas phases, together with the concentration along the axis of the catalytic monolith. The resulting profiles provides valuable information on the performance of the process under different working conditions and using different fuels. Moreover, catalyst deactivation can be monitored and insights on the different deactivation mechanisms can be provided through the repeated experiments. The CPO process has been studied for years in this plant proving its suitability for the small scale H_2 production using different fuels.

Recently, cordierite honeycomb monoliths coated with 2% wt. Rh supported on α-Al_2O_3 and Mg-Al_2O_4 were tested with the aim of evaluating the role of the active phase support on the stability of the catalyst [44]. Results of this study showed that magnesium-aluminate, as an active phase support, provides higher stability compared to the alumina that is lower deactivation after experimental testing with ethanol. The reduced deactivation rate was coupled with a decrease of the overall carbon deposited on the surface, which was evaluated through temperature programmed oxidation (TPO). In this chapter we extend this investigation to a third commercial mixed-oxide support, that is a La-promoted alumina. 2% wt. Rh washcoat was prepared and tested under similar working conditions of the previous studies on MgAl2O4. Axial profiles of temperature and concentration, were measured and compared with the profiles obtained in the previous work with Mg-Al_2O_4 during CPO tests of methane and ethanol. This work focuses on the deactivation trend of the catalyst by monitoring the systematic loss of performance identified by the growth of the hot spot temperature on the surface of the monoliths. At the end of this chapter, the aged catalytic monolith was subjected to TPO to evaluate quantitively and qualitatively carbon deposition on the surface during the CPO of ethanol. Results of the TPO analyses, are compared with

the profiles obtained for catalysts supported on α-alumina and Mg aluminate. Table 3.1 represents the main characteristics of the catalyst that has been compared in this chapter.

Monolith	Catalyst	Primer	Lcat [cm]	m cat [g]	Thickness [μm]
MarkIV	2% Rh/α - Al2O3	Yes	3.14	0.713	14.5
MarkMgIII	2% Rh/Mg-Al2O4	Yes	2.82	0.790	29.9
MarkLaI	2% Rh/La-Al2O3	Yes	3.34	0.849	16.2

Table 3.1: CPO and TPO tested catalysts

* thicknesses were calculated assuming homogeneous distribution of the washcoat, a washcoat density of 1.25 g/cm^3 for α-alumina and La-alumina and a washcoat density of 0.76 g/cm^3 for Mg-alumina.

Ignition procedure

To light off the reactor in the absence of a heating source, a procedure adopted during previous activities was followed. It consists of two phases:

1. Initially preheating of the catalyst by stoichiometric H2 combustion, with 6% v/v H2, 3%v/v O2, N2 to balance and 5 NL/min as total flow rate. The catalytic conversion of H2 increases the reactor temperature, as monitored with a thermocouple placed downstream the reactor (thermocouple 3 in Figure 3.1, blue line in Figure 3.2)
2. Once the temperature read by the thermocouple downstream the monolith reaches a value of about 220°C, the second phase starts, during which the H2/air feed is switched into either CH4/Air /N2 or EtOH/Air/N2 feed, with a total flow rate of 10 NL/min. Exothermic reactions ignite and the reactor heating completes, eventually leading to the reaching of steady state close to adiabatic conditions.

Figure 3.1 shows the temperature trends during the light off process; the green square highlights the switch from H2/O2/N2 to the ethanol-air-nitrogen mixture at 220 °C.

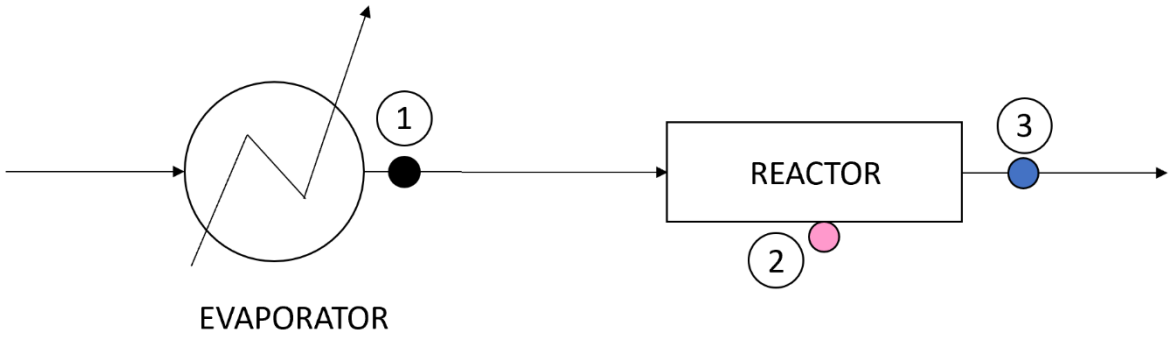

Figure 3.1: Sketch of the position of the thermocouples

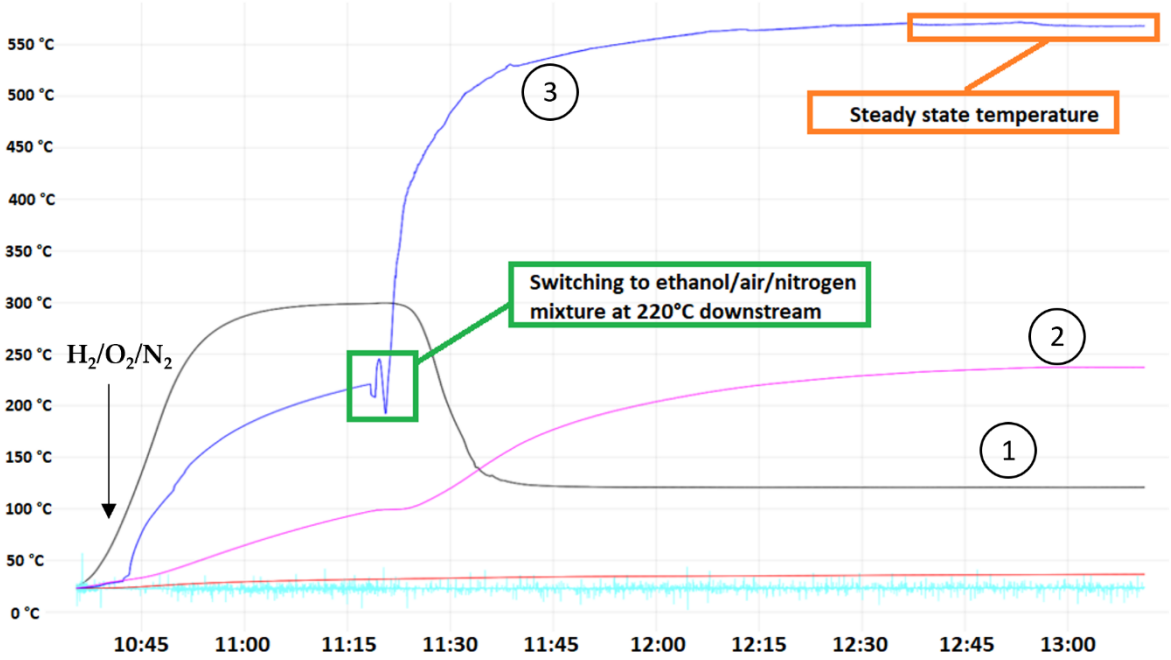

Figure 3.2: Ignition procedure: blue line = TC downstream the reactor; black line = TC inside the evaporator; pink line = peripheral TC at the reactor entrance

Switching to EtOH/Air/N2 mixture is not performed in a single step where the temperature is kept under control through a progressive decease of the C/O ratio and the diluting nitrogen flow. During these steps, the total volumetric flow was always kept constant and equal to 10 NL/min. This is because the mass flow controllers and the pump have regulation limits: it is not possible to adopt flow rates below 5 NL/min, which would impose pump rpm too low, and mass flow controller openings below 1%. There is no predefined number of steps in which the ignition must be designed. Therefore, once the volumetric flow rates and temperatures are determined, the last step involves the check of the mass flow controller openings: for each step, a theoretical

opening and a theoretical pump rotational speed are calculated using the calibration curves, and then the flow rates are checked from the consumption rate of the fuel in the graduated burette.

Reactor thermal efficiency

The thermal efficiency α of the reactor (Equation 3.1) was evaluated to verify the adiabatic operation of the process.

$$\alpha = \frac{T_{exp}^{out} - T_{exp}^{in}}{T_{adiabatic}^{out} - T_{exp}^{in}} \tag{3.1}$$

In this equation T_{exp}^{in} is the temperature measured by a thermocouple located at the inlet of the reactor, T_{exp}^{out} is the temperature measured by a thermocouple at the end of the monolith and $T_{adiabatic}^{out}$ is the adiabatic temperature calculated from the enthalpy balance with the inlet composition, inlet temperature and the outlet composition. The thermal efficiency of the reactor for all the performed experiments in this study, was about 90%, which indicates that the reactor operated in a condition very close to the adiabatic one.

3.1 CPO CH4

The CPO test with CH_4/air provides a benchmark for the verification of the reactor performance and the comparison with the reference catalysts. The results of a CH_4-CPO test, obtained with the lanthanum-alumina are presented in Figure 3.4. Vertical dotted lines represent the total length of the monolith, while the horizontal line on the right represents the thermodynamic equilibrium value.

The profiles obtained are qualitatively similar to the ones obtained in previous CPO studies over Rh/α-Al_2O_3 [13][14][42]. Two reaction zones are distinguished: the inlet oxy-reforming zone, where oxygen is still present in the gas phase, and the downstream reforming zone, where oxygen is totally converted. In the oxy-reforming zone a step increase of the temperature occurs, with the formation of a hotspot, due to the overlap of oxidation and reforming reactions on the catalyst surface. The reforming reaction in the reforming zone lowers the temperature and increases the syngas productivity. Previous modelling studies accounting for the rate of heterogeneous reactions and heat and mass transfer phenomena have clearly shown that the consumption of oxygen in completely controlled by its diffusion rate. Regarding the methane consumption, it proceeds under mixed chemical-diffusive control [39]. After the complete consumption of oxygen, the fuel continues to react with water, via steam reforming, producing H_2 and CO. As a result of the overlap between exothermic

reactions and endothermic reforming reactions, the temperature of the solid phase, measured by the pyrometer through the optic fiber, is expected to show a maximum at the entrance of the monolith (oxy-reforming zone) and to further decline (reforming zone) to the adiabatic equilibrium temperature. It is also expected the full equilibration with the gas-phase temperature profile, measured by the thermocouple. In MarkLaI experimental campaign, the temperature profiles of solid and gas phase were flat along most of the monolith growth, with a small growth of a hotspot as shown in Figure 3.2. As reported in Figure 3.3, the axial concentration profiles vary a lot at the entrance of the reactor and reach the equilibrium mole fraction rapidly. Thus, the two zones are not clearly distinguishable, but a unique short reaction zone is detected. This can be caused by the relatively large washcoat load and thickness which maximize the steam reforming rate at the very inlet [39]. However, the axial evolution of water, characterized by a steep peak at the very inlet and a decay down to the equilibrium value, clearly reveals the sequence of oxidation and steam reforming producing and consuming water respectively. Finally, it is observed that at the outlet of the catalyst, the pyrometer signal has a sudden drop since the tip of the optical fiber collect the radiation from the surrounding surfaces of the reactor, which are at a lower temperature [37]. The temperature measured by the thermocouple downstream the monolith decreases as well but at a lower extent, because of the cup mixing phenomena, that is, the mixing of gases of the central and outer channels which might be colder due to some residual heat dispersion of the system.

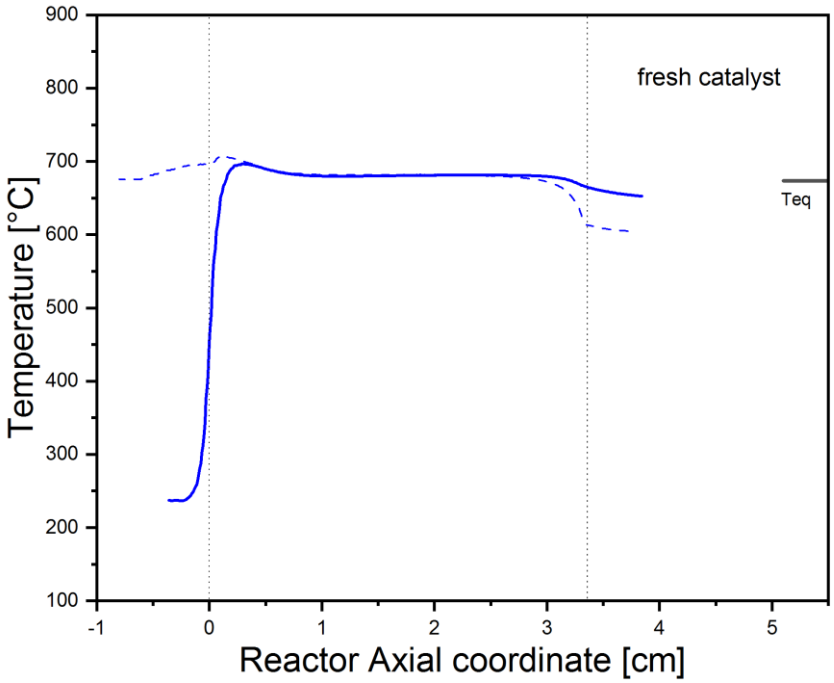

Figure 3.3: Spatially resolved temperature profile for the reference CPO CH4 experiment on MarkLaI. Operating conditions: CH4 = 27.3%, C/O = 0.9, Tin = 25°C, flow rate = 10NL/min

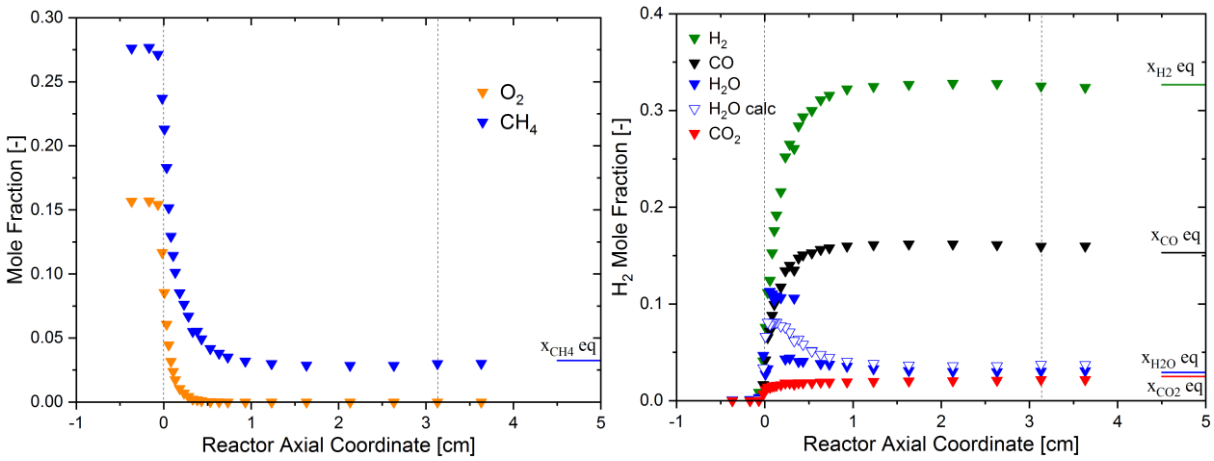

Figure 3.4: Spatially resolved concentration profiles for the benchmark CPO experiment on MarkLaI. A) Reactants. B) Products

The comparison of CPO-CH_4 benchmark tests over MarkLaI and MarkMgIII are reported in Figures 3.4 and 3.5 for temperature and concentration profiles respectively. Looking at the temperature profile, it can be seen that the trend and the maximum temperature of both the gas and solid phase were almost the same for both catalysts, with a slightly higher peak temperature reported for MarkMgIII with respect to the one of MarkLaI.

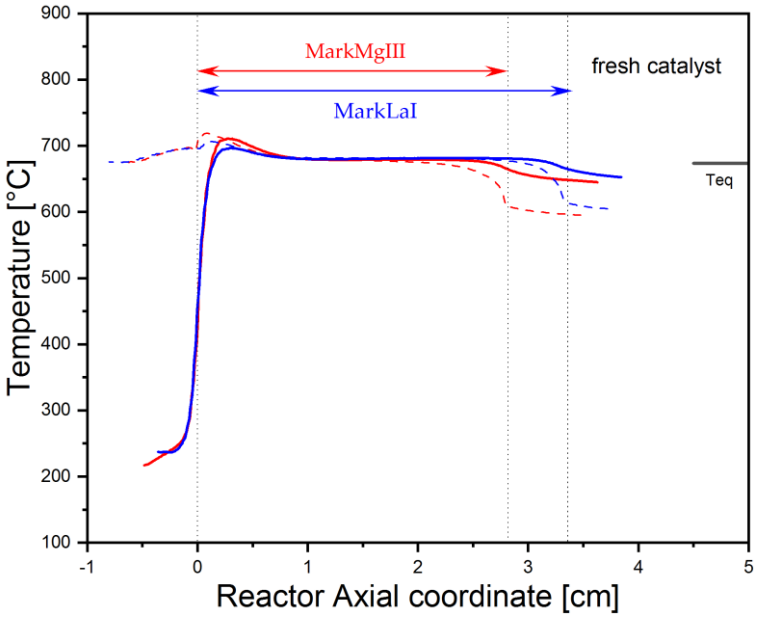

Figure 3.5: Comparison between MarkMgIII and MarkLaI temperature profiles for the CPO of CH4 benchmark test. Operating conditions: CH_4 = 27.3%, C/O = 0.9, T_{in} = 25°C, flow rate = 10 NL/min.

Concerning the axial concentration profiles of the reactants and of the main products, plotted in Figure 3.6, it is possible to notice that the oxygen consumption and the methane consumption have the same rates in both catalysts.

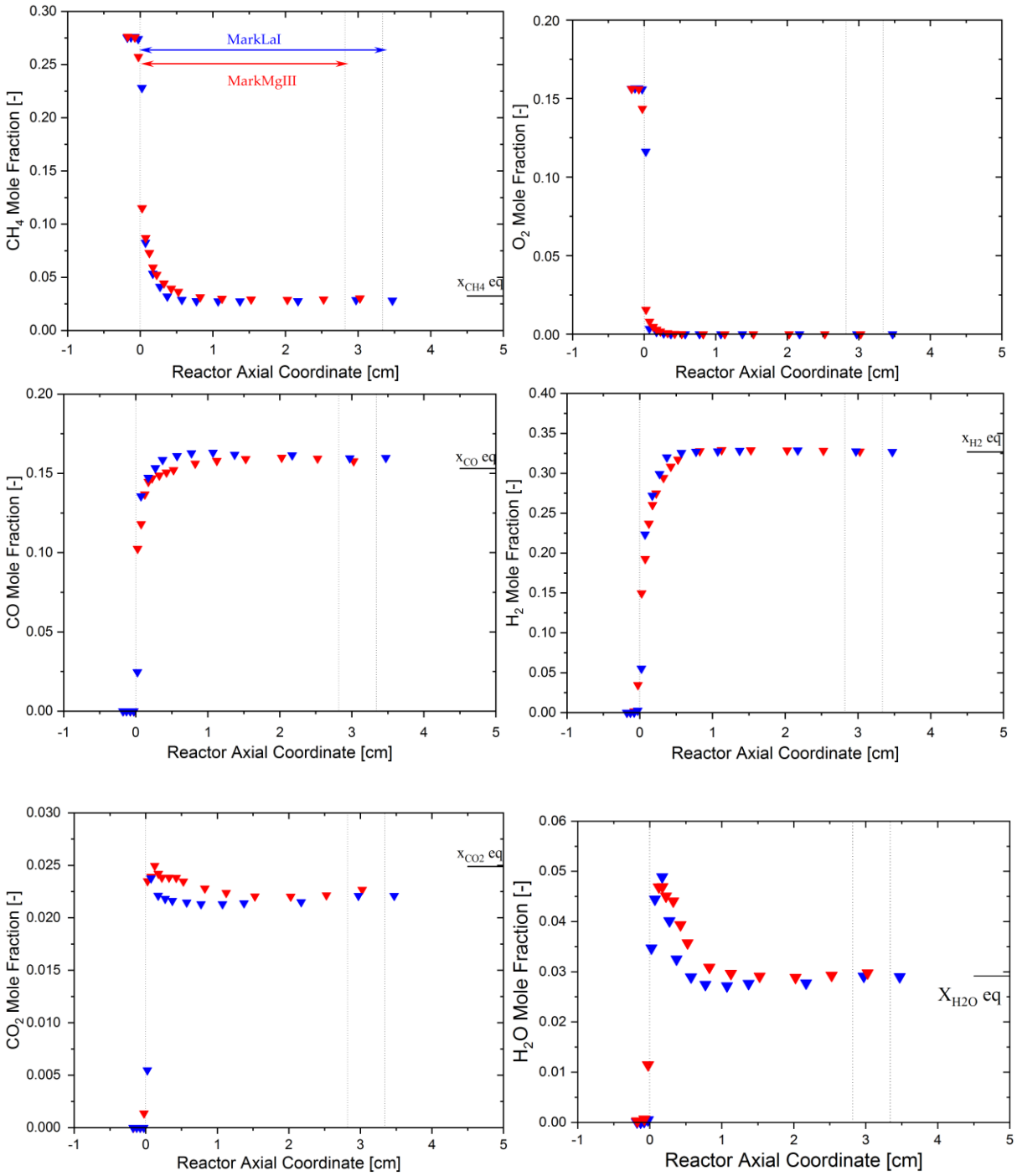

Figure 3.6: Comparison between MarkMgIII and MarkLaI concentration profiles for the CPO of CH4 benchmark test. Operating conditions: CH_4 = 27.3%, C/O = 0.9, T_{in} = 25°C, flow rate = 10 NL/min.

The oxygen is totally consumed at 1 mm from the entrance. The trends of all the products are very similar comparing the two catalysts. However, MarkLaI shows a slightly higher concentration of CO and H_2, while MarkMgIII a higher production of CO_2 and H_2O was recorded at the first 15mm of catalysts. From this point, the curves become flat toward the equilibrium value.

3.2 CPO of EtOH

The spatially resolved temperature profiles of ethanol CPO for MarkLaI and MarkMgIII are presented in Figure 3.7. Here the support did not seem to affect significantly the thermal behavior. In both cases, the temperature measured by the thermocouple shows a fast rise in the first part of the catalyst until reaching the maximum, of which the bigger is the one of MarkLaI. The pyrometer measurement shows hot spots at higher temperatures, exactly at the catalyst entrance. The limited intensity of the hotspots, always lower than 850 °C, suggests that major sintering does not occur during the experiments.

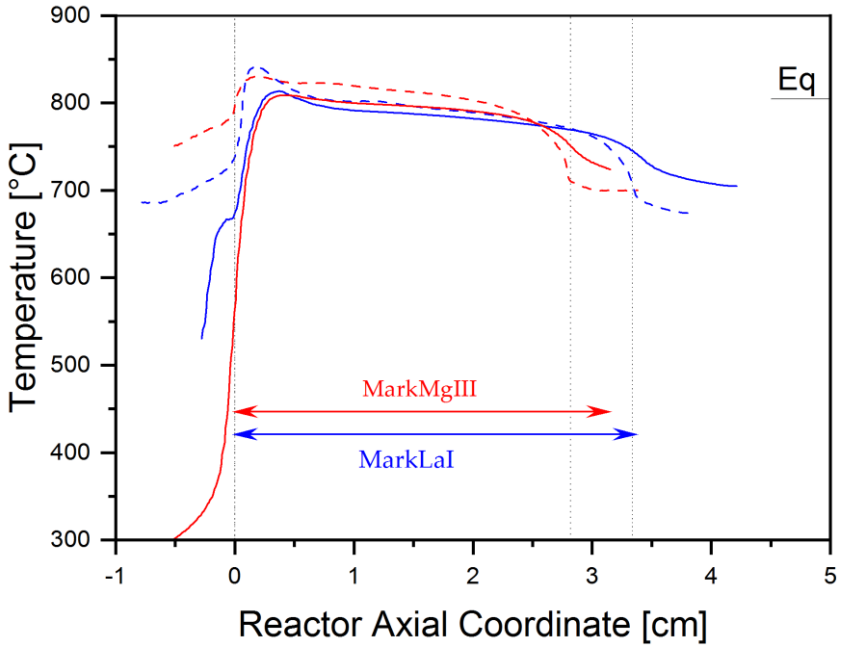

Figure 3.7: Comparison between MarkMgIII and MarkLaI temperature profiles for the CPO of C_2H_5OH test with H_2O co-feed. Operating condition: C_2H_5OH = 11.2%, H_2O = 3%, C/O = 0.65, T_{in} = 150°C, flow rate = 10 NL/min.

In Figure 3.8 the axial concentration profiles of reactants and products are plotted. The O_2 consumption, in the same way that happens with the methane feed, occurs at the very entrance of the reactor. Differently from the CPO of CH4 however, the EtOH consumption occurred along a more extended length by a combination of total

oxidation and steam reforming. The main products were hydrogen and carbon monoxide, steadily produced along all the axial length of the reactor. For both the catalysts, water shows a maximum at around 1mm from the entrance, and this is in line with its consumption by steam reforming and its formation by oxidation reactions. For the CO_2, it is mostly produced at the entrance for both catalysts. The production of acetaldehyde mostly took place in front of the monolith due to the homogeneous reactions occurring in the void space and in the reactor head. A slightly higher concentration of acetaldehyde is recorded for the La-doped catalyst which may be explained by the higher gas temperature recorded before the catalyst compared to MarkMgIII. Regarding the ethylene, its production starts at the entrance of both catalysts. For both the species, the complete consumption occurs before 1 cm, mainly by steam reforming as shown in the decreasing concentration of water. The amount of acetaldehyde, ethylene and water is higher in MarkLaI, while oxygen and ethanol quantity upstream to the catalyst are mostly the same. Regarding the methane profile, it shows different behaviors for the two catalysts. For the two catalysts, the production starts at the entrance, with a steep rise and has a decreasing trend in the first 7mm, due to the steam reforming. Then the concentration increase very slowly along the catalytic channel. Several reactions can play a role in determining the complex evolution of methane, i.e., decomposition of ethanol and acetaldehyde, methanation, steam reforming, or homogeneous cracking reactions: the initial formation could have been caused by homogeneous cracking reactions that were due to the high temperature within the first two millimeters of the catalyst. An intermediate consumption of methane is most likely due to heterogeneous steam reforming. The final formation of methane, experienced in both Mg-aluminate and La-doped alumina supported catalysts, after the drop in the molar fraction was probably due to heterogeneous reactions, e.g., methanation of synthesis gas or acetaldehyde decomposition to methane and carbon monoxide[37]. For both catalysts, the overall reaction process was practically complete within 1 cm, i.e. less than half of the coated length, and a close approach to equilibrium was reached, as revealed by the flattening of most of the concentration profiles. It is worth mentioning that the compositions of the product stream measured downstream from the reactor were slightly different from those measured at the end of the monolith but within the central channel; this can be explained by the cup-mixing effect that has been already observed in previous studies [37], where the outer channels may be colder due to some residual dispersion of the system and the kinetic limitations affect the efficiency of steam reforming reactions. This effect is also visible in the temperature profiles.

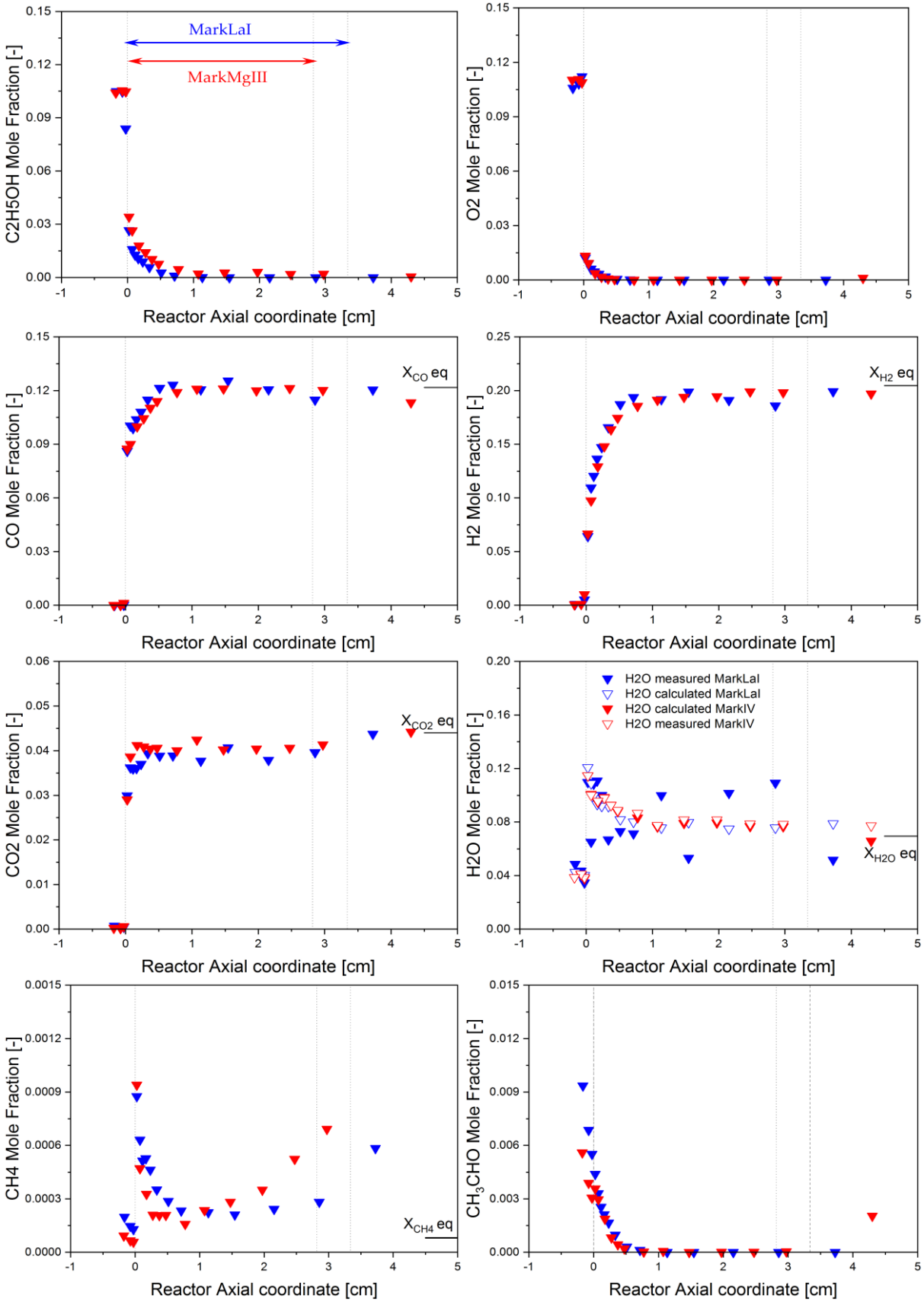
MarkLaI
MarkMgIII
C2H5OH Mole Fraction [-]
O2 Mole Fraction [-]
CO Mole Fraction [-]
H2 Mole Fraction [-]
CO2 Mole Fraction [-]
H2O Mole Fraction [-]
CH4 Mole Fraction [-]
CH3CHO Mole Fraction [-]
Reactor Axial coordinate [cm]
X_CO eq
X_H2 eq
X_CO2 eq
X_H2O eq
X_CH4 eq
H2O measured MarkLaI
H2O calculated MarkLaI
H2O calculated MarkIV
H2O measured MarkIV

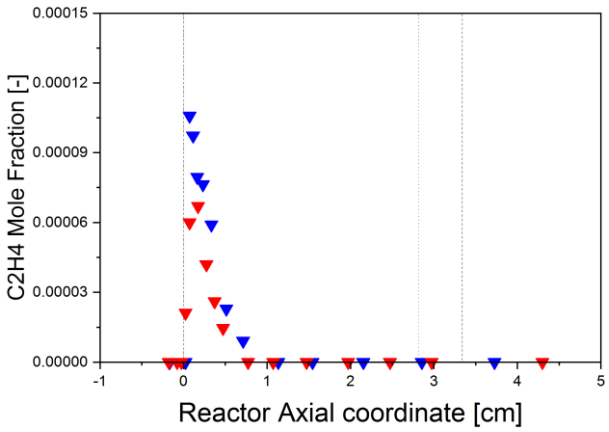

Figure 3.8: Comparison between MarkMgIII and MarkLaI concentration profiles for the CPO of C_2H_5OH test with H_2O co-feed. Operating condition: C_2H_5OH = 11.2%, H_2O = 3%, C/O = 0.65, flow rate = 10 NL/min

3.3 Deactivation

The stability of the catalysts during the ethanol campaign was verified through a periodical repetition of standard CH_4 CPO tests, during which axial temperature profiles (with both the thermocouple and the pyrometer) and integral outlet composition were measured. At the end an additional concentration CH_4 CPO test was run. The temperature tests were performed after each ethanol experiment and the profiles measured by the pyrometer and thermocouple are reported in Figure 3.9 A and B for MarkLaI and MarkMgIII respectively. The total working time of MarkLaI with ethanol was about 13h. After this time frame, the growth of a hot spot in CH_4 CPO was distinctly observed and more pronounced when compared with MarkLaI. The hot spot is formed as a result of the superposition of the exothermic oxidation and endothermic steam reforming process.

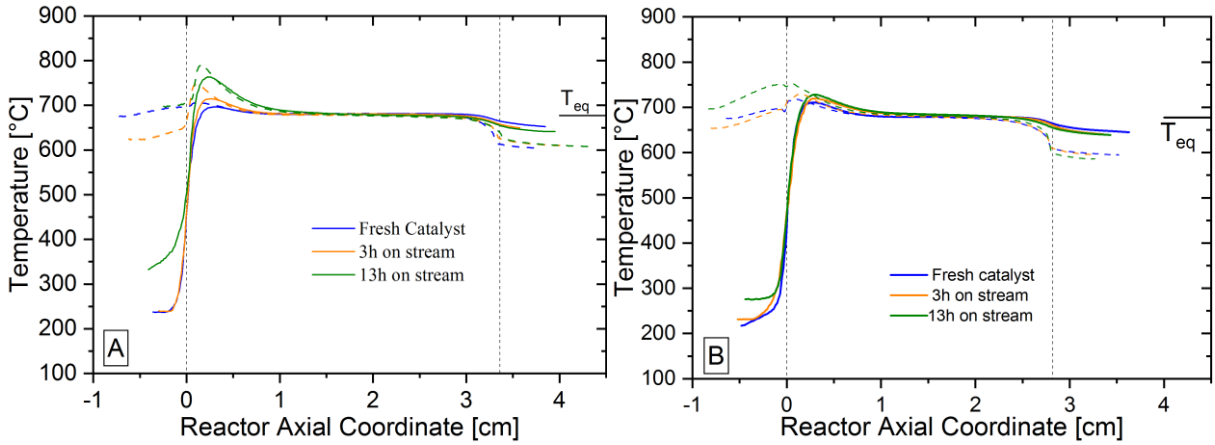

Figure 3.9: Periodical temperature profile for the CPO of CH_4 for A: MarkLaI and B: MarkMgIII aging. Operating conditions: CH_4 = 27.3 %, C/O = 0.9, Tin = 25 °C, flow rate = 10NL/min.

The released heat flux is not influenced by the catalyst deactivation since the rate of the exothermic oxidation reactions is extremely high and entirely governed by mass transfer. This can be verified from the mostly complete overlapping of oxygen concentration profiles of the fresh and aged catalyst showed in Figure 3.10

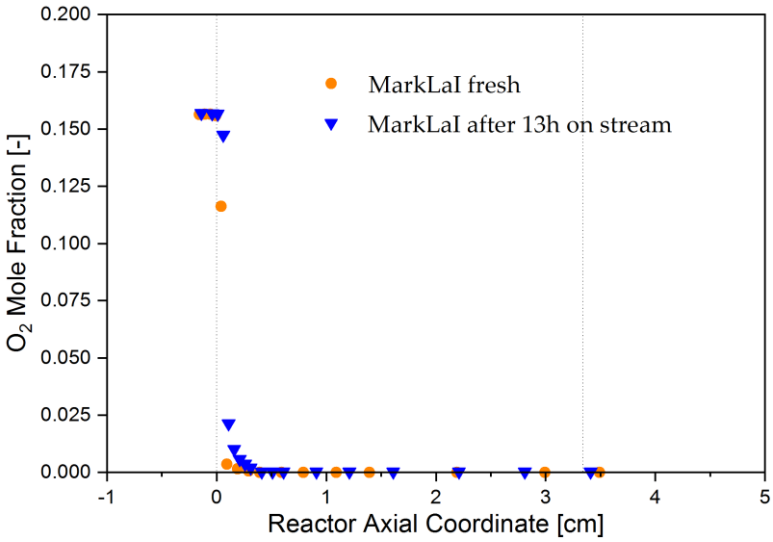

Figure 3.10: Effect of the catalyst deactivation on the O_2 concentration profile for CH_4 CPO. Orange circles represent the fresh catalyst. Blue triangles represent the aged one. Operating conditions: CH_4 = 27.3 %, C/O = 0.9, T_{in} = 25°C, flow rate = 10NL/min.

Here the oxygen consumption is extremely high and entirely governed by mass transfer. Instead, catalyst deactivation limits the reaction rate of CH4 stream reforming because it is under partial chemical kinetic control. During the 13h stream of ethanol, some loss of activity was experienced.

3.4 Temperature Programmed Oxidation

Following the same procedure used in previous studies, MarkLaI was analysed to identify the major deactivation mechanism. Figure 3.11 shows the reactor with a catalyst used in a previous thesis [44] loaded, before (A) and after (B) its utilization. It can be seen that after 13h on stream, the color of the catalyst become grey, which may indicates the presence of carbon deposits. However, Rh oxidation is also a known cause of catalyst blackening.

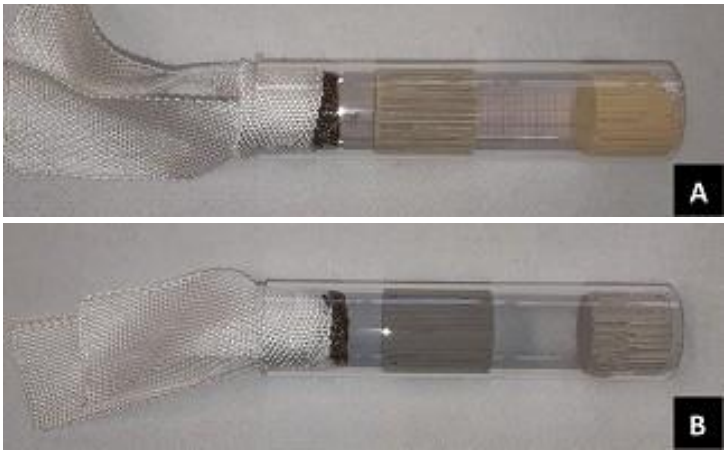

Figure 3.11: Reactor display of fresh (A) and aged (B) catalyst

In order to characterize qualitatively and quantitatively the carbonaceous structures formed on the aged catalyst, the MarkLaI catalyst was subjected to temperature programmed oxidation (TPO). It was cut in three parts along the axial coordinate, as detailed in Figure 3.12 and Table 3.2. The samples were then ground and loaded into a quartz reactor and oxidized in air, monitoring the amount of CO2 produced up to 800°C.

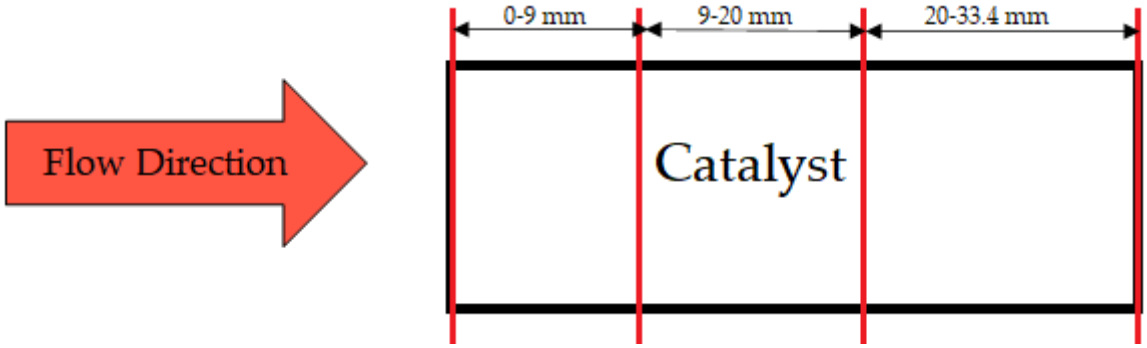

Figure 3.12: Scheme of a monolith with the cutting zone highlighted

Zone	L [mm]	Sample [g]
I	0-9	0.1250
II	9-20	0.1243
III	20-33.4	0.1233

Table 3.2: TPO sample data

Figure 3.13 shows the TPO profiles of MarkLaI, MarkMgIII and MarkIV, used as a comparison. Three CO_2 peaks can be distinguished, associated to the combustion of

different types of carbon deposition on the surface. The main characteristics and the overall amount of carbon deposited on each catalyst are reported in Table 3.3.

The molar flow rate of carbon dioxide has been normalized on the number of moles of rhodium, assuming a uniform distribution of the metal on the monolith, in order to get comparable results among different TPO tests.

The first peak is clearly visible for all the 3 catalysts, and it is around 290°C and can be correlated with the oxidation of relatively non-structured carbon and/or carbon deposited on the catalytic sites. The second peak, less sharp than the first one, detected at about 400°C, may be linked to more ordered structures. This peak is more evident in MarkLaI than in the other two. The third peak was found at around 550°C and can be correlated with the gasification of relatively more complex graphitic carbon structures and/or carbon located on the acidic sites of the support, far from the Rh sites[14][38].

From the TPO results reported above, it is possible to observe that the total amount of carbon deposited on MarkLaI is higher than the one deposited on MarkMgIII and MarkIV (Table 3.3), with MarkMgIII being the one with the lowest deposition. From Figure 3.13, it can be seen that amount of carbon deposited along the axial direction is quite constant for MarkMgIII and MarkLaI, while for MarkIV there is much more carbon deposited on the first segment than in the second and third one.

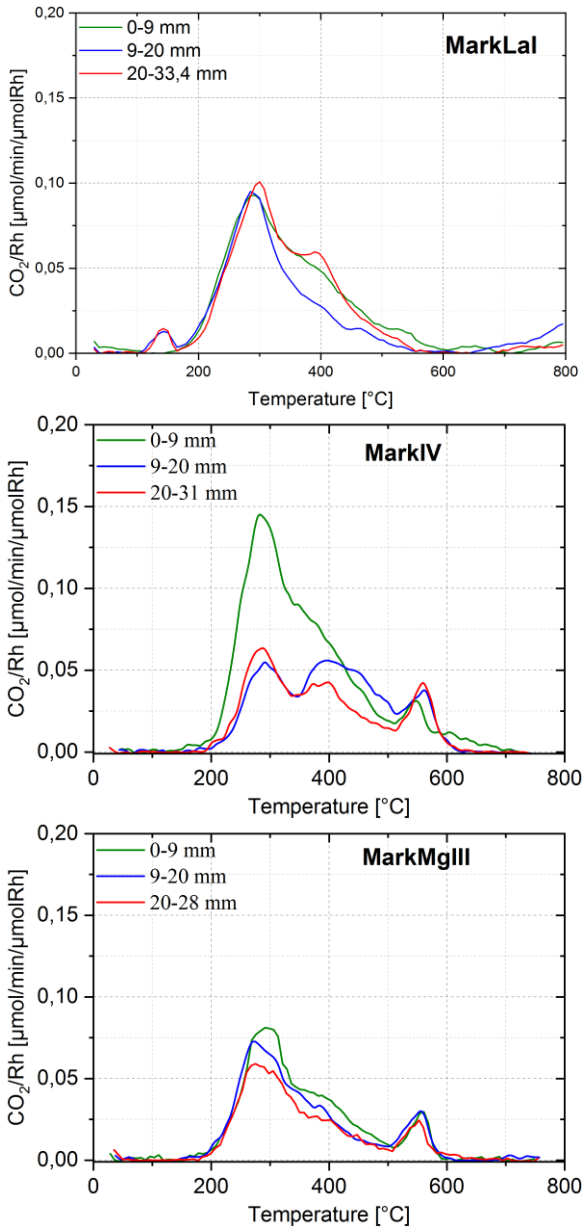

Figure 3.13: TPO results of MarkLaI, MarkIV and MarkMgIII

Catalyst	Formulation	m Cat [g]	TOS	Carbon Deposits [µmolC / µmolRh]
MarkLaI	2% Rh/La-Al2O3	0.849	13h	37.65
MarkIV	2% Rh/α-Al2O3	0.713	13h	32.17
MarkMgIII	2% Rh/Mg-Al2O4	0.790	13h	23.27

Table 3.3: Main characteristics and amount of carbon released as CO_2 in the TPO of each catalyst.

Looking at the collected data, it looks like the La-doped alumina and the Mg-aluminate don't have major differences related to the productivity of syngas, both from methane and EtOH. The only difference that has been pointed out is the one regarding the stability, as seen in the deactivation behavior. Additionally, MarkMgIII shown the lowest tendency towards coke formation among the three tested catalysts making the Mg-aluminate, being more stable, the most suitable support of the three for the CPO of EtOH. The results of this study call the attention towards a need for a kinetic investigation to evaluate the role played by the active phase support in the CPO process.

4. Experimental activities in the annular reactor

The adiabatic reactor is not suitable for the kinetic investigation since it is a non-isothermal reactor; it operates under the influence of heat and mass transfer limitations; and gas phase reactions are expected to play an important role. The tools in catalysis, suited for the kinetic investigation are isothermal microreactors, where the temperature of the catalytic bed is uniform and known and where, by varying contact time, the process can be observed from different to integral regime which implies the changing of role of consecutive reactions or inhibition phenomena. In our laboratory, a special design of microreactor has been developed consisting in an annular duct. Herein the catalyst is present in the form of thin film over a ceramic tube that is then inserted into a quartz tube. The gas stream flows in between. This reactor has the advantages of having less diffusive limitations and high capacity for heat dissipation by irradiation combined with the high dilution in nitrogen. The negligible pressure drop and the high space velocity that can be reach, allow to obtain quasi-isothermal conditions because of the laminar regime that characterize the small duct. These characteristics allow to study the kinetics of very fast and not thermodynamic equilibrium-limited reactions such as CPO in which the combustion of hydrocarbons at high temperatures occurs. This reactor has been used for years for the study of the production of syngas from different fuels, such as EtOH, methane or formic acid. In particular the study of methane on this plant has brought to the creation of a kinetic model (introduced in Section 2.4). So in this section, the role of the active phase support will be discussed, through the kinetic study in the annular reactor, performing experiments of methane and ethanol CPO and SR on a $Rh/MgAl_2O_4$ coated tube. The effect of the GHSV and O_2/C ratio was evaluated for both. The tests performed on $Rh/Mg\text{-}Al_2O_4$ have been compared, in a qualitative way, to analogues results obtained from testing Rh/Al_2O_3, in order to highlight possible differences in the pathways of the conversion and macro-differences in the kinetics, in particular on the reaction rate. Later, a comparison between experiments with $Rh/Mg\text{-}Al_2O_4$ and prevision of a model was carried out. This model was developed to account the performance of Rh/Al_2O_3 (model description in section 2.4), and the comparison with its provision allows to make an evaluation more precise and to quantify some differences between the 2 systems. In this way it is possible to excluding also the effects caused by experimental factors such as the possibility of having slightly different conditions in the tests.

Thermodynamic analysis

Steam reforming and partial oxidation of methane and ethanol involve complex mechanisms and numerous species. The thermodynamic equilibrium composition was evaluated for all the tests reported in this thesis using the a chemical equilibrium calculator provided by the Colorado State University under the hypotheses of constant temperature and pressure [56]. As the catalytic partial oxidation process can be considered as the combination of oxidation and steam reforming reactions in the presence of oxygen deficit, the analysis included the gas phase species $C_2H_5OH, CH_3CHO, CH_4, C_2H_6, CO, CO_2, H_2, H_2O, N_2, and\ O_2$ as reported in previous thermodynamic studies [75]. For the case of CPO, oxygen is another species in addition to the steam reforming ones. Solid carbon (graphite) was not considered in these calculations as the selected working conditions thermodynamically disfavours the formation of coke. Results of this analysis are reported as a dashed line in all the following presented plots.

4.1 Effect of conditioning

Previous studies of catalytic activity in Rh/Al_2O_3 systems have shown that catalyst performance changes when exposed to reaction conditions [76]. This was associated with a superficial reconstruction of the catalyst. It would consist in the progressive disappearance of defective sites in favor of a larger growth of particles exposing regular and high-density crystalline faces. This leads to a progressive increase in "useful" activity for the α-Al_2O_3 catalyst, for example in SR reactions. A diagram of the conditioning process was shown in Figure 4.1.

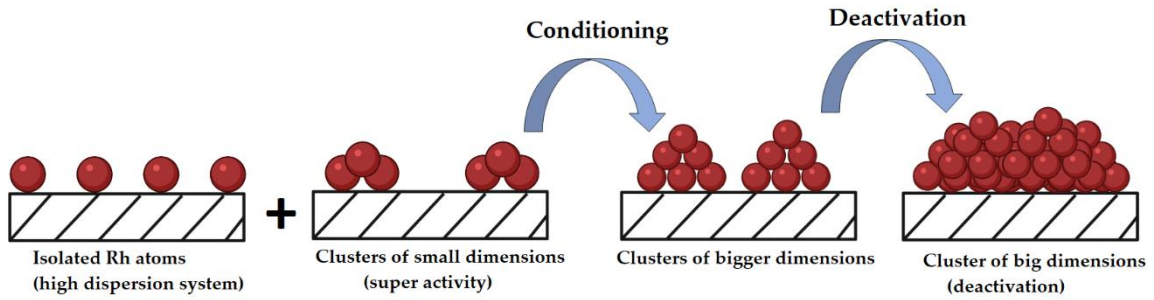

Figure 4.1: Restructuring of aggregates during conditioning

Consequentially, before CPO and SR experiments with EtOH, it was necessary to subject the catalytic system to some conditioning tests using methane as fuel, in order to verify the activity and the stability of the catalyst. For methane CPO, a standardized procedure is followed to reach stable activity conditions: repeating tests with 3% v/v CH_4, 1.68% v/v O_2 and N_2 to balance the mixture, using a space velocity (GHSV) of 8e5 $NL/h/kg_{cat}$.

Figure 4.2 shows the results of two methane conditioning tests, Run15 and Run16, carried out in succession. The presented plots verify the repeatability of the results and the stability of the catalyst after the conditioning.

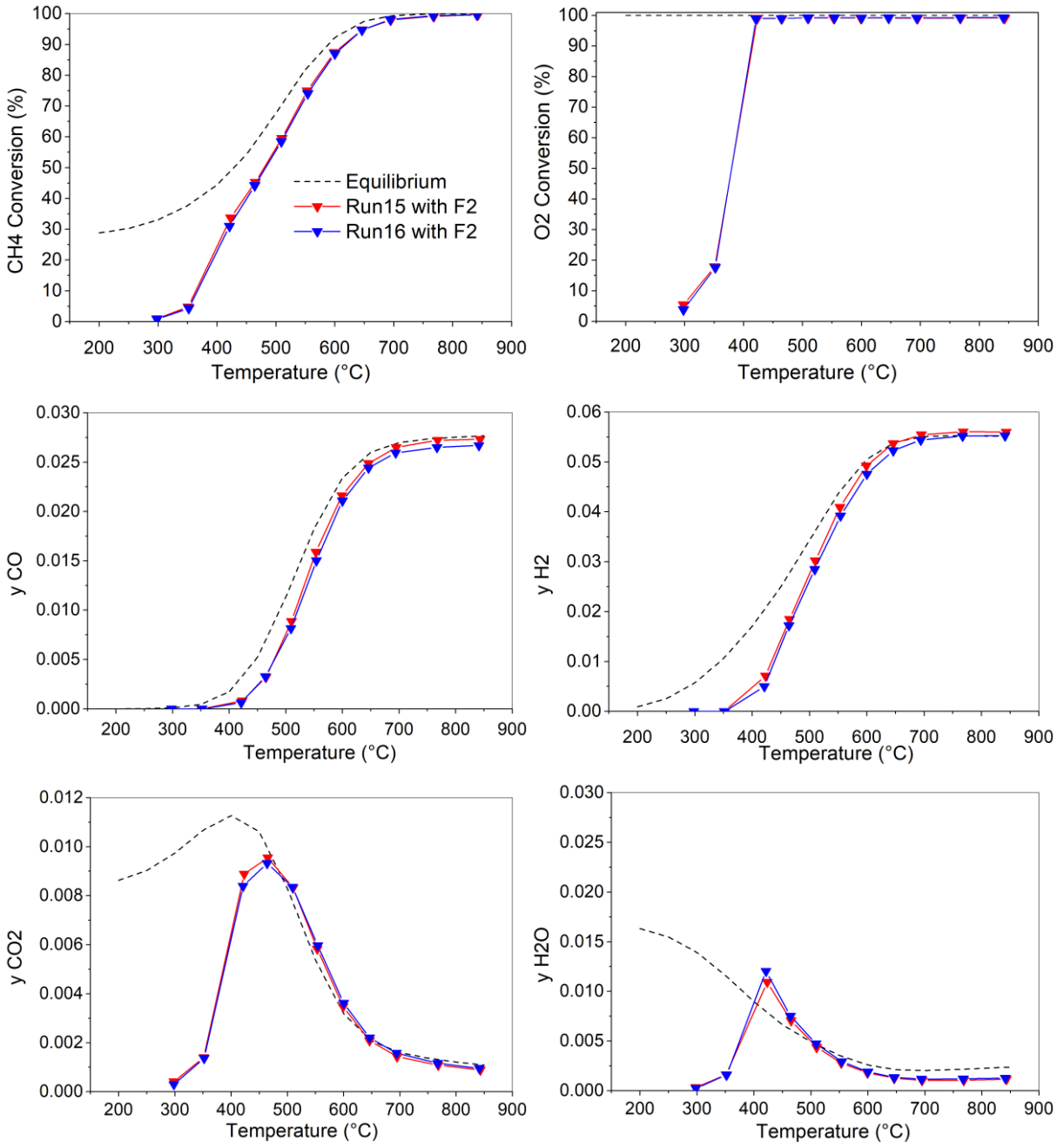

Figure 4.2: Conditioning of Rh/Mg-Al_2O_3. Red: Run15 Blue: Run16. Operating conditions: GHSV = 800000 NL/h/kg CH_4 = 3% O2/C = 0.56.

Differently from the α-Al_2O_3 supported catalyst reported in Hochkoeppler and Braglia thesis work[57], in this conditioning tests, the activity does not seem to change so

much, without an increase of useful activity in the SR zone and without a loss in the mid-temperature zone.

In all the CPO tests carried out in this thesis work, the ratio O2/C is kept at 0.56, being a higher than the stoichiometric value for partial oxidation (for methane, it is equal to 0.5), chosen to disfavor carbon deposition on the catalyst.

4.2 Preliminary tests with CH_4/O_2 and CH_4/H_2O feeds and comparison with alumina

4.2.1 Methane CPO

In this section, three parameters (temperature, space velocity and feed composition of CPO CH4 test have been explored to study their effect on the overall products distribution. The test consists of temperature ramp from 300 to 850 °C at varying feed conditions. After each experiment, the obtained plot has been compared with an experiment done in the same condition with an α-alumina catalyst.

Effect of temperature and space velocity

The catalyst F2 (Rh/Mg-Al_2O_4) has been tested at two different space velocity (8e5 and 2e6 NL/h/kg) in the range of temperature from 300 to 850 °C, maintaining for most of the test a step of 50 °C. Firstly, the results of these tests have been compared to see the effect of this space velocity over the products distribution. Then, in order to highlight some differences caused by the different support, the results have been compared, in a qualitative way, with results obtained with Rh/Al_2O_3 catalysts. The catalyst used in this section are reported in Table 4.1.

Catalyst	support	m cat[g]	L [cm]	thickness [µm]
F2	Mg-Al2O4	0.020	3	67*
GV1	α-Al2O3	0.054	6	55*
GV5	α-Al2O3	0.036	5	45*

Table 4.1: GV1, GV5 and F2 main characteristics.

* Thicknesses were calculated assuming homogeneous distribution of the washcoat and a washcoat density of 1.25 g/cm^3 and 0.76 g/cm^3 for Rh/α-Al_2O_3 and Rh/MgAl_2O_4 respectively.

The tests have been performed in the same CPO CH_4 conditions: inlet molar fraction of CH_4= 3% and ratio O2/C = 0.56. **Figure 4.3** shows the effect of the increase of space velocity on the Mg-alumina support. In black it is represented the lower GHSV, while with the red one the higher one. Having a higher GHSV, the residence time of the flow is lower, causing so a lower conversion of the fuel. In fact it can be seen that the product distribution in the lower space velocity case, starting from around 500°C, approach the equilibrium line, reaching also complete conversion of methane at high temperatures, while the higher one never get close to it, ending with a maximum conversion of methane of around 90%. A direct consequence of this lower conversion is the lower quantity of products of steam reforming (CO and hydrogen) at high temperatures, consistent with the higher concentration of CO_2 and water. **Figure 4.4** shows instead the effect of increasing the space velocity in the α-alumina case. These two figures make possible a qualitative comparison between the effect of the 2 supports over the CPO of methane. Considering the lower space velocity in both graphs, in the case of the alumina, the conversion and the distribution of products don't come as close to the equilibrium line as in the case of the Mg-alumina. Considering the effect of GHSV, in the alumina case, regarding the oxygen conversion, the differences between the two space velocity is lower compared to the Mg-alumina case. Much more evident is the effect on the CO_2 and water for alumina, in which the two different space velocity influence the distribution, having much less CO_2 at higher space velocity and much more H_2O, differently from the case of Mg-alumina.

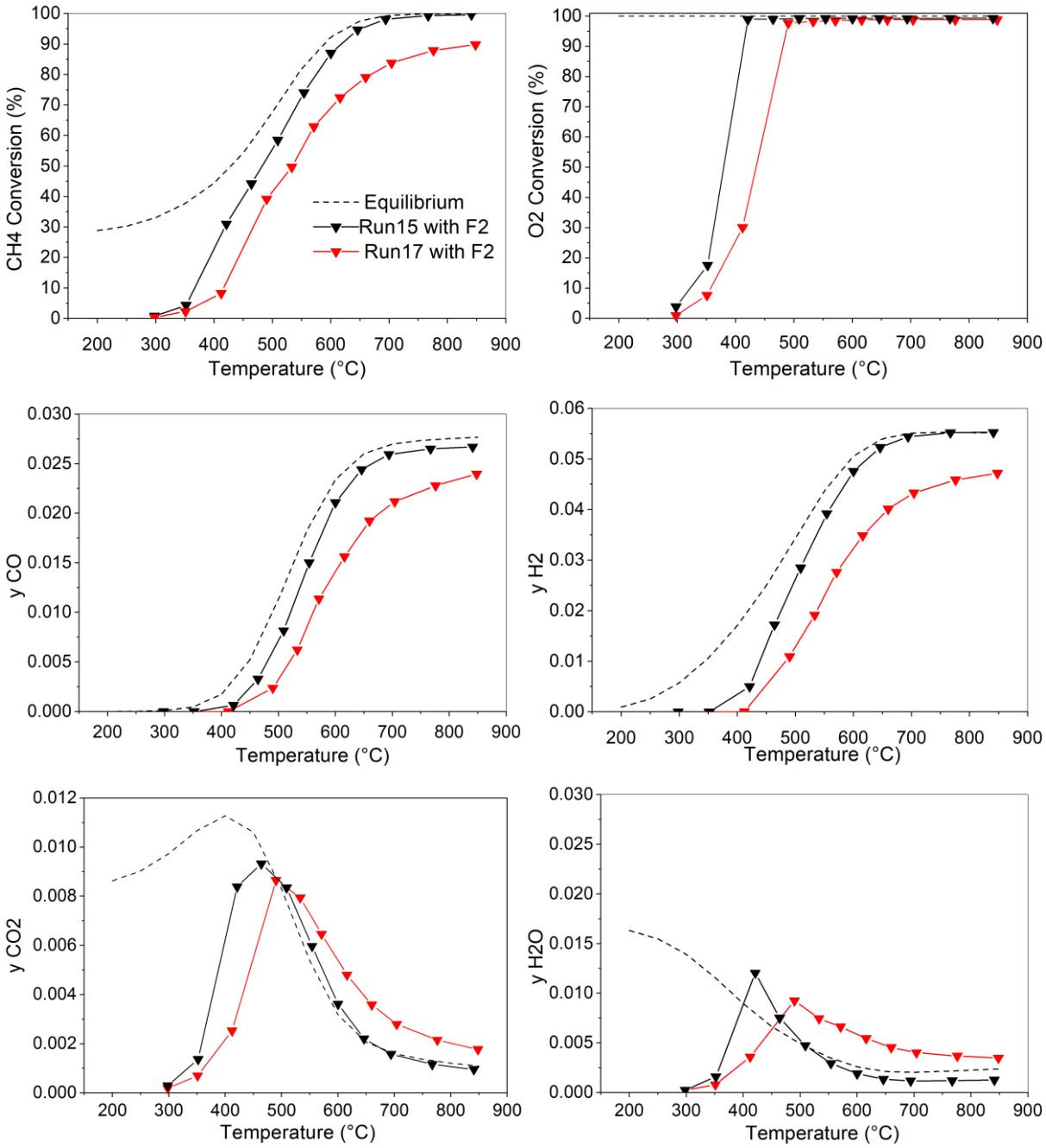

Figure 4.3: Effect of GHSV on CPO CH4 tests with Mg-alumina catalyst F2.

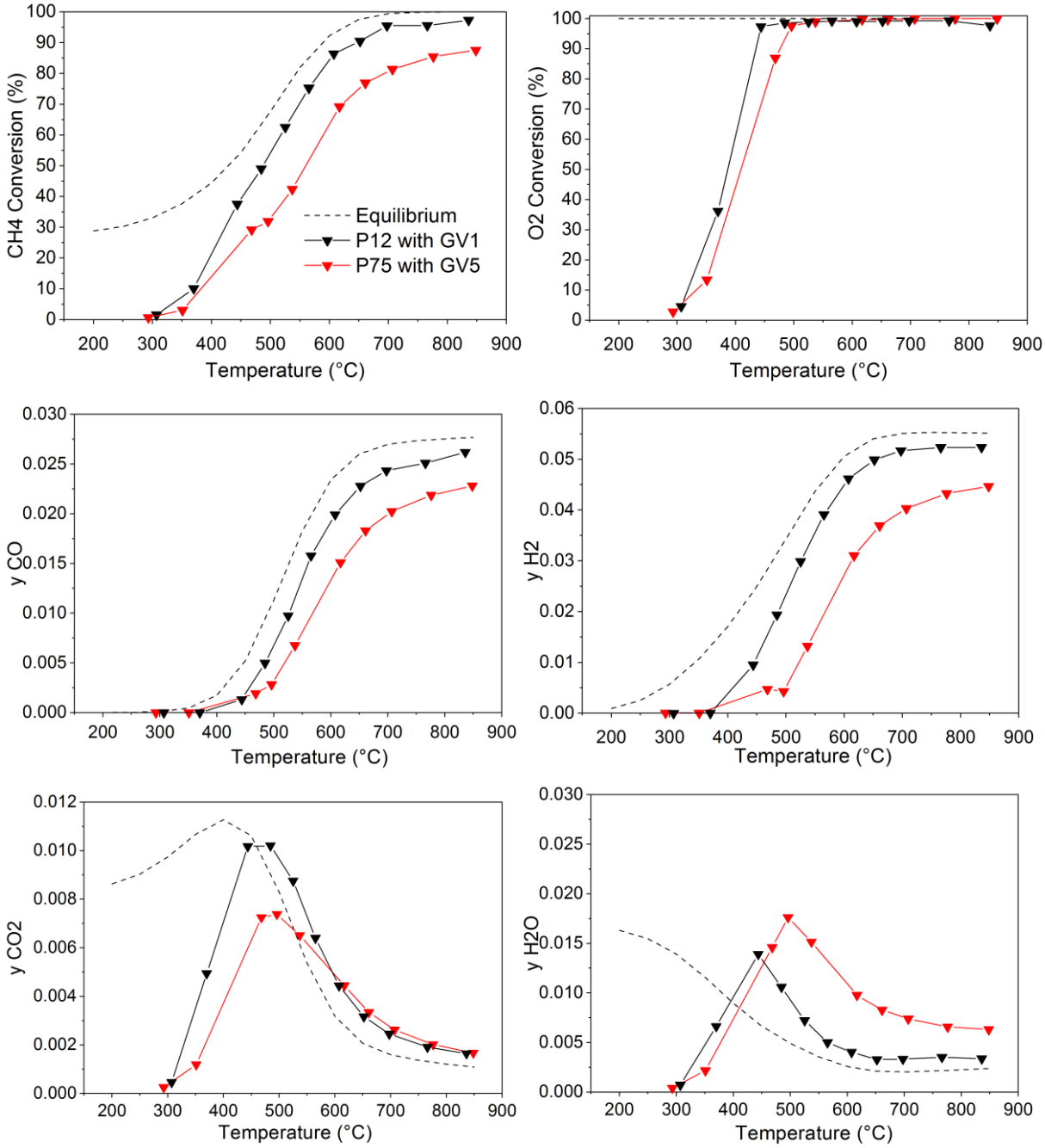

Figure 4.4: Effect of GHSV on CPO CH_4 tests with α-alumina catalysts.

In order to make a more precise evaluation, the experimental results regarding the effect of the space velocity over a Rh/Mg-alumina support have been compared to the prediction of the kinetic model described in Section 2.4. The results of this comparison are shown in Figure 4.5.

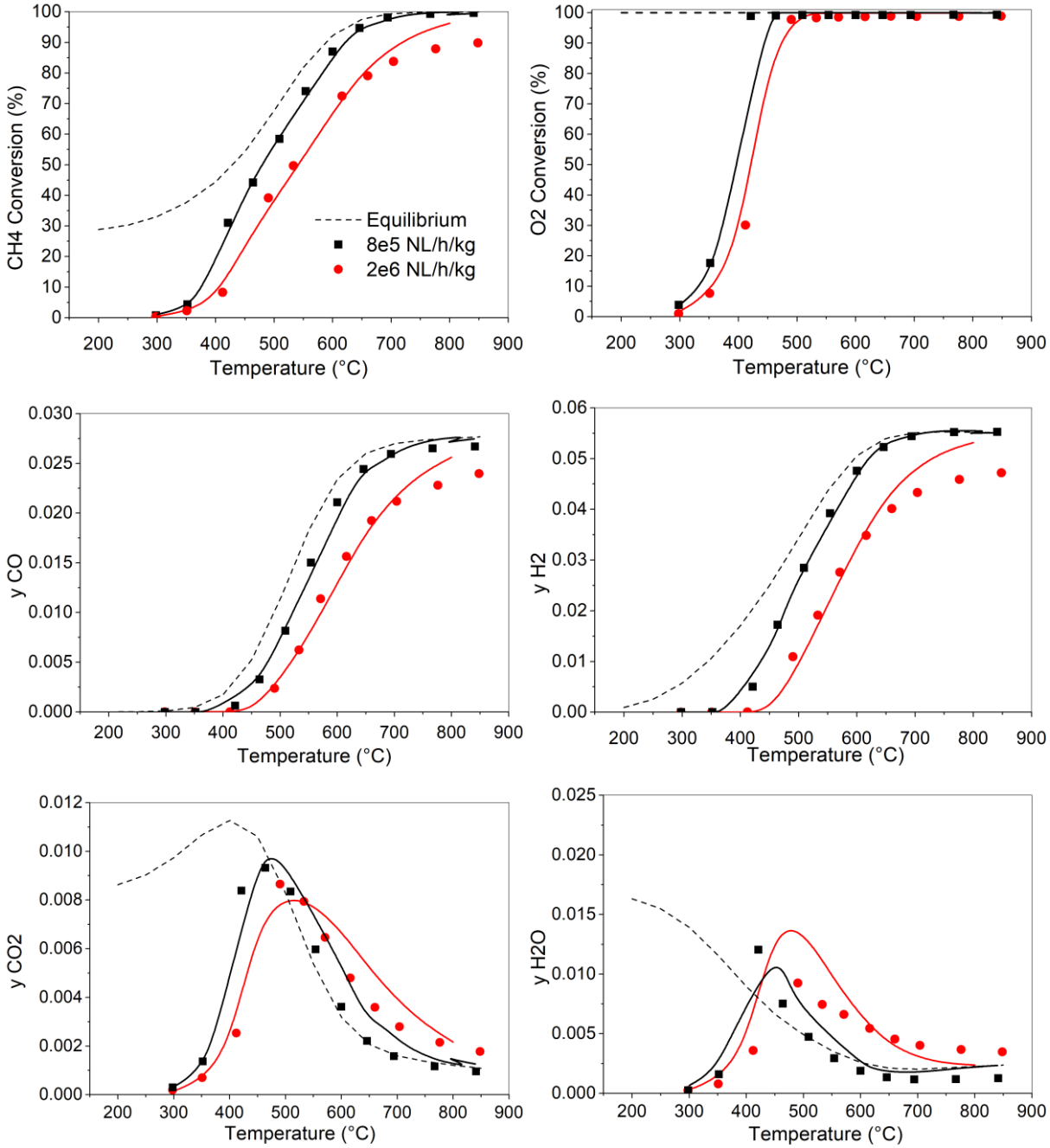

Figure 4.5: Comparison between experimental and model data for the CPO of CH_4: Effect of the space velocity

In the case of low space velocity, the model simulations are very close to the experimental data, with some small differences in the case of water and CO_2. In the case of high space velocity, still in the low temperature range the model can predict well the behavior of the various species. However, going to high temperature range,

from 600 °C, differences show up. In particular, regarding the methane conversion at high temperatures, the model predicts a nearly complete conversion, while in our experimental data we cannot reach values over 90%. This is the region where mass transfer resistance can assume a role and influence the reactivity. A way to decrease these differences between experimental data and the model could be to take into account this mass transfer limitation by decreasing the Sherwood number. Also the morphology of the catalyst could be taken into account.

In the overall, it seems that the model follows in a good way our data, meaning that the kinetic behavior of the two supports can be considered very close one to each other.

Effect of temperature and oxygen to carbon ratio

Another parameter that is interesting to study is the oxygen to carbon ratio and its effect on the concentration profiles for the methane CPO. Three ratios have been chosen for this experimental campaign: 0.56, 1 and 1.3. They have been obtained keeping the methane concentration constant at 3% v/v and varying the oxygen concentration: 1.68, 3 and 3.9% are the resulting concentrations. As it is shown in Figure 4.6, CH4 conversion was unaffected by the change of ratio at lower temperatures (between 300 and 400°C). With the decrease of O2/C ratio, the production of CO and H2 at equilibrium increase, and this is because high concentrations of O2 favor combustion by increasing selectivity in water and CO2, while decreasing the one of H2 and CO. For this reason, the production of syngas results to be shifted towards higher temperature with the increase of the ratio. As done before, these experimental data have been compared to the one obtained through the model simulation. Figure 4.7 shows this comparison.

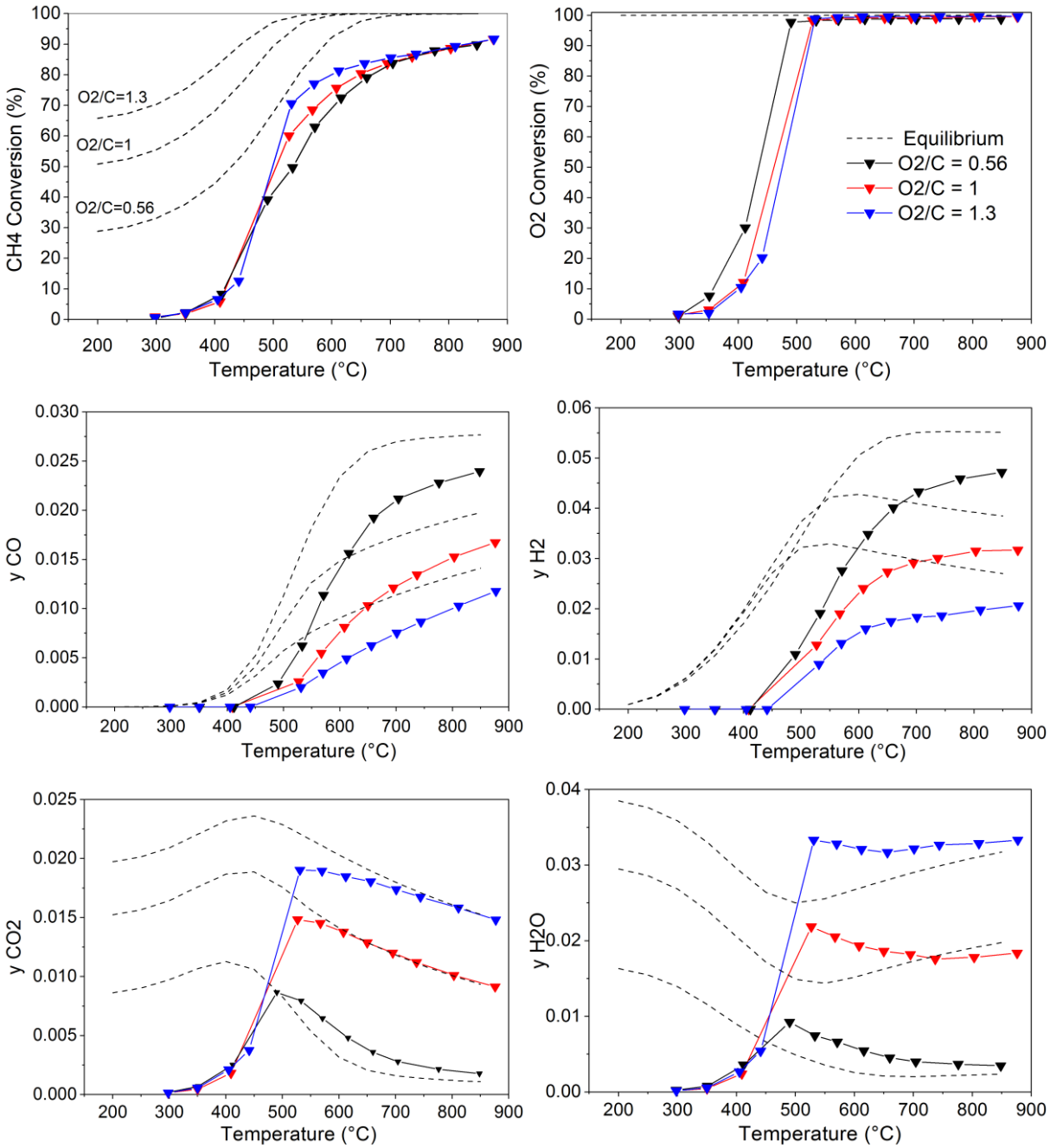

Figure 4.6: Effect of O2/C ratio on CPO CH4 tests with Mg-alumina catalyst F2.

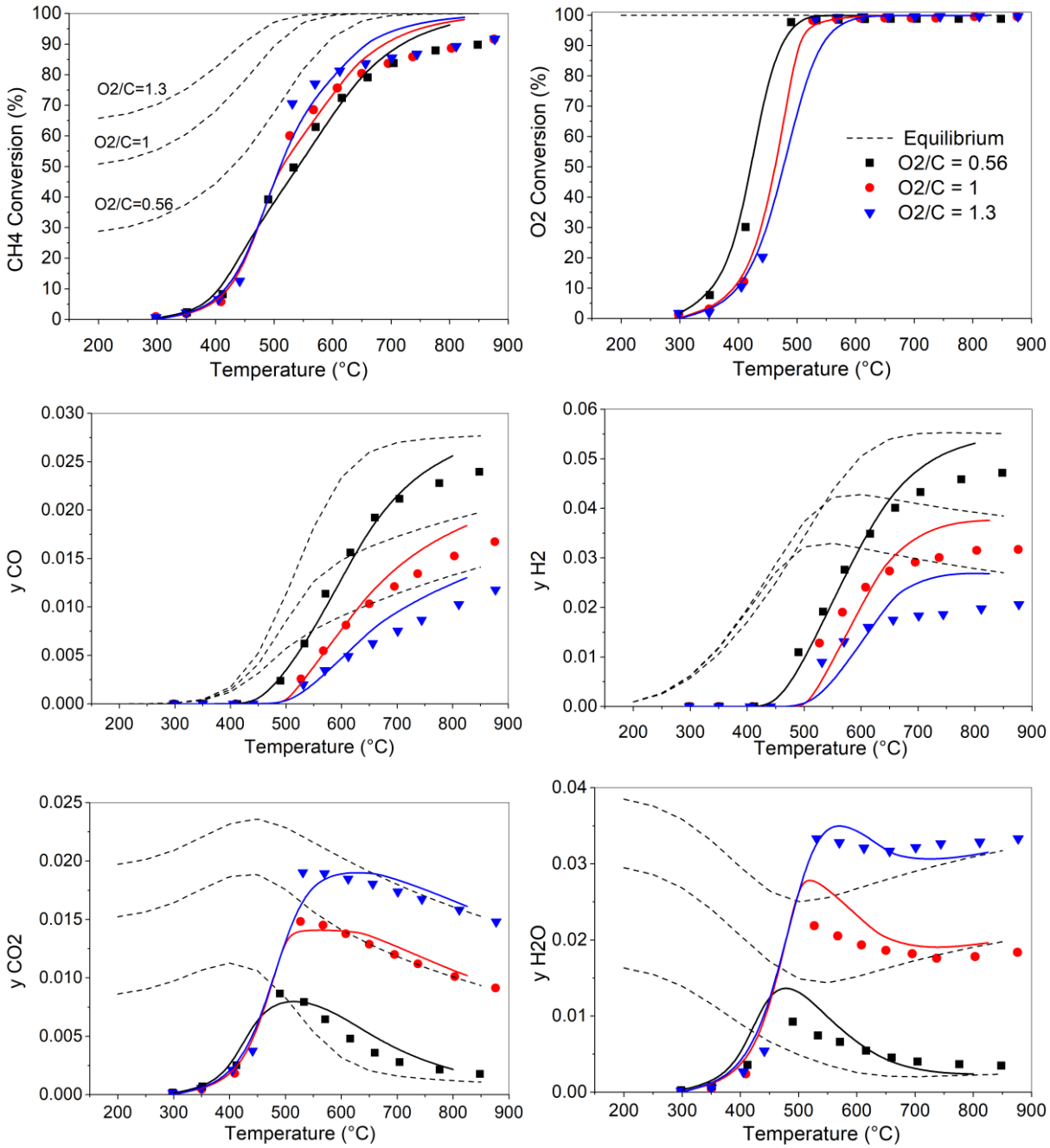

Figure 4.7: Comparison between experimental and model data of methane CPO: effect of the oxygen to carbon ratio.

The model follows in a good way the experimental data also in this case, especially the oxygen conversion graphs. Carbon dioxide is a little overestimated at high temperature, while water is overestimated at middle temperatures. Methane conversion reach the same value at high temperatures, without reaching total conversion. The products are well represented by the model.

4.2.2 Methane SR

In this experimental campaign, F2 has been compared with a α-alumina catalyst from Piazza-Bayram thesis work[74]. Nearly all the trends result to be quite similar, with the blue lines being the Run26 done with F2, while orange one the Test97 done with GV5, introduced in previous section. The only interesting difference is the shift of the CO2 concentration line, with the F2 one being lower until 600°C and then overcoming the other.

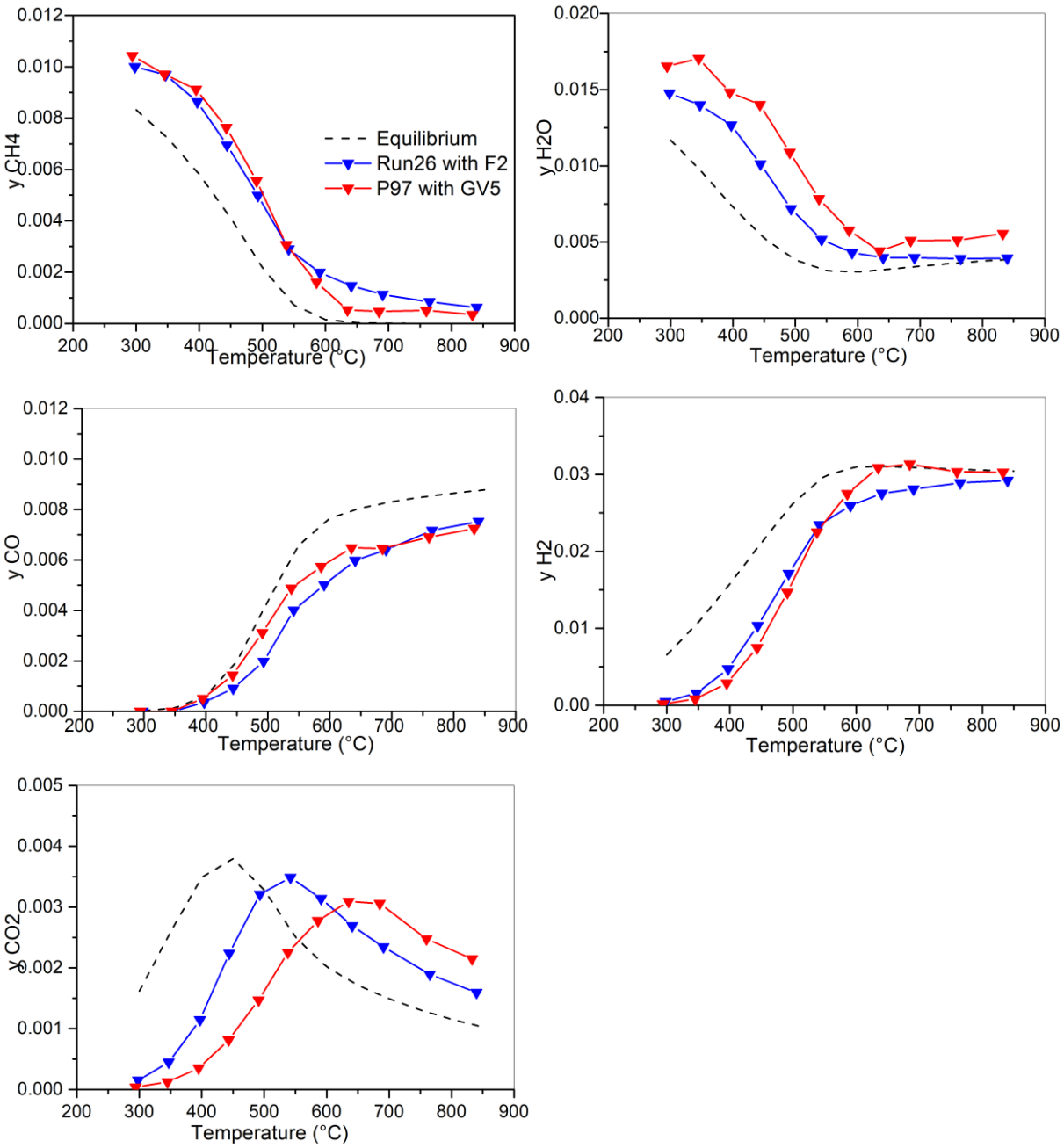

Figure 4.8: Comparison between SR CH4 done with F2 and GV5 catalysts.

As previously done for the CPO of methane, also the SR of methane can be simulated through the kinetic model.

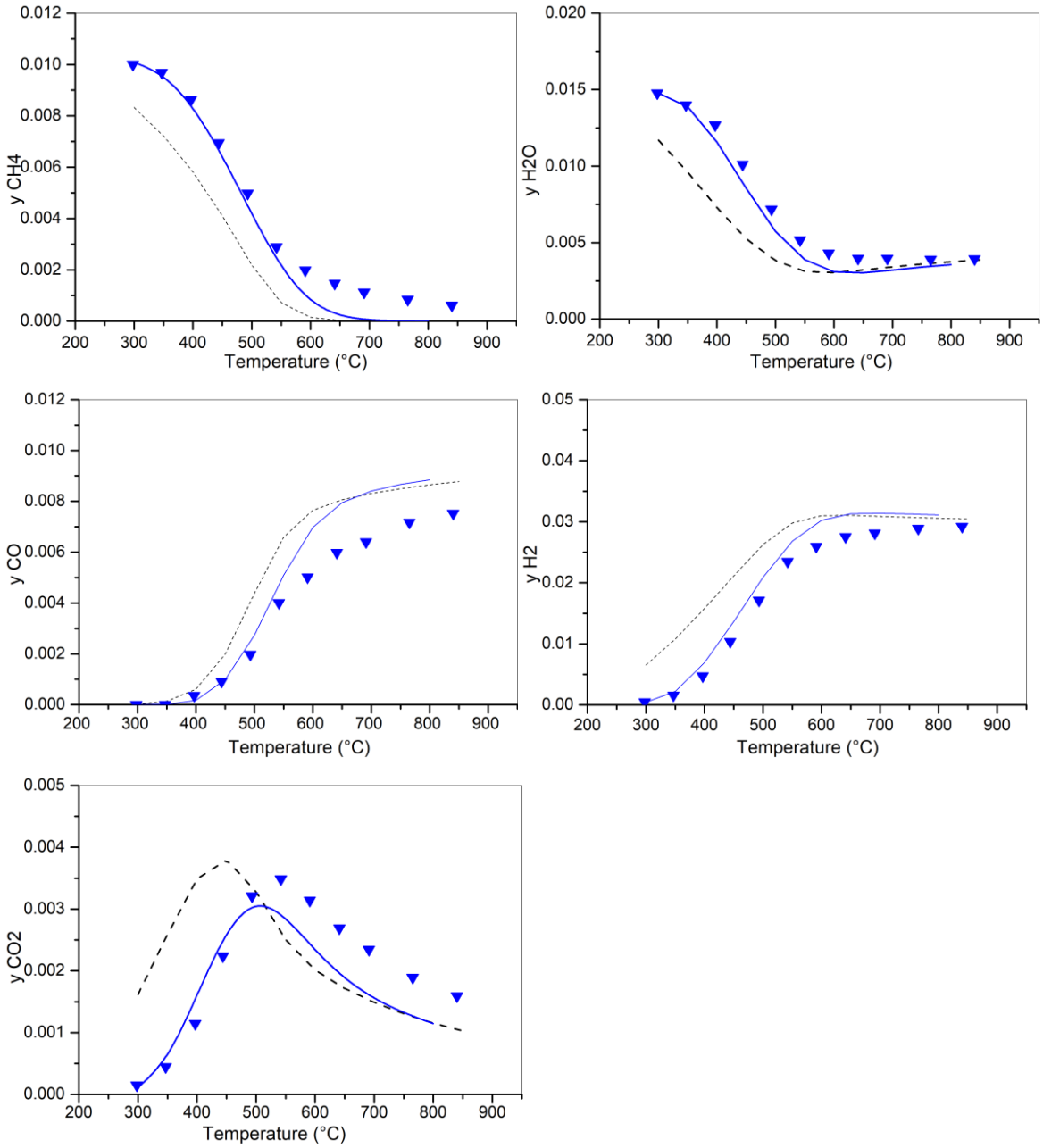

Figure 4.9: Comparison between experimental and model data for SR of methane.

In this case the model follows the reactants very precisely till 550 °C, and then does not obtain the exact values for the methane trend. The CO_2 production is underestimated while the CO production is overestimated by the model. The H_2 trend is similar between experimental and model data.

4.3 Test with EtOH/O_2 and EtOH/H_2O feeds and comparison with alumina

4.3.1 CPO of EtOH

The experimental campaign with methane has substantially confirmed that no significant change of reaction rates was associated to the nature of the support. However, the experiments in the adiabatic reactor reveal that EtOH CPO is a more critical process, and the reactor performance depends not only on the rate of major reaction involved in the conversion of ethanol and oxygen, but also on the extent of secondary reactions responsible for the formation of C-surface species which can negative affect the stable operation. For this reason, the investigation was extended to EtOH CPO and SR on the isothermal reactor. Ethanol CPO experiments were conducted on a 2% Rh-$MgAl_2O_4$ catalyst and then compared with test done on α-alumina. In these tests, O2/C ratio is 0.56, higher than the stoichiometric value (for ethanol it is equal to 0.25), to disfavour the formation of carbon deposits.

Table 4.2 lists the main characteristics of the 2 catalysts, being F2 the one with Mg-alumina and GV6 the one with α-alumina

Catalyst	support	m cat [g]	L [cm]	thickness [µm]
F2	Mg-Al2O4	0.020	3	67 *
GV6	α-Al2O3	0.050	5	61 *

Table 4.2: GV6 and F2 main characteristics.

* thicknesses were calculated assuming homogeneous distribution of the washcoat and a washcoat density of 1.25 g/cm^3 and 0.76 g/cm^3 for α-Al_2O_3 and $MgAl_2O_4$ respectively.

All the tests were conducted at atmospheric pressure and very diluted mixture to operate under near-isothermal conditions. Temperature gradually increases from 150 to 800 °C. In the graphs, the dashed curves represent the equilibrium lines and they have been calculated using Stanjan [56] website (acetaldehyde equilibrium line cannot be seen in the plot because its average value, in the order of 10^{-10} is out of scale).

The ethanol is fed through a saturator, and temperature and nitrogen flow are the parameters that control the amount of it passing into the steam phase. The first, as the saturator is not thermally insulated, is highly variable during the tests so it causes ethanol input to the reactor to vary significantly even within the same experiment.

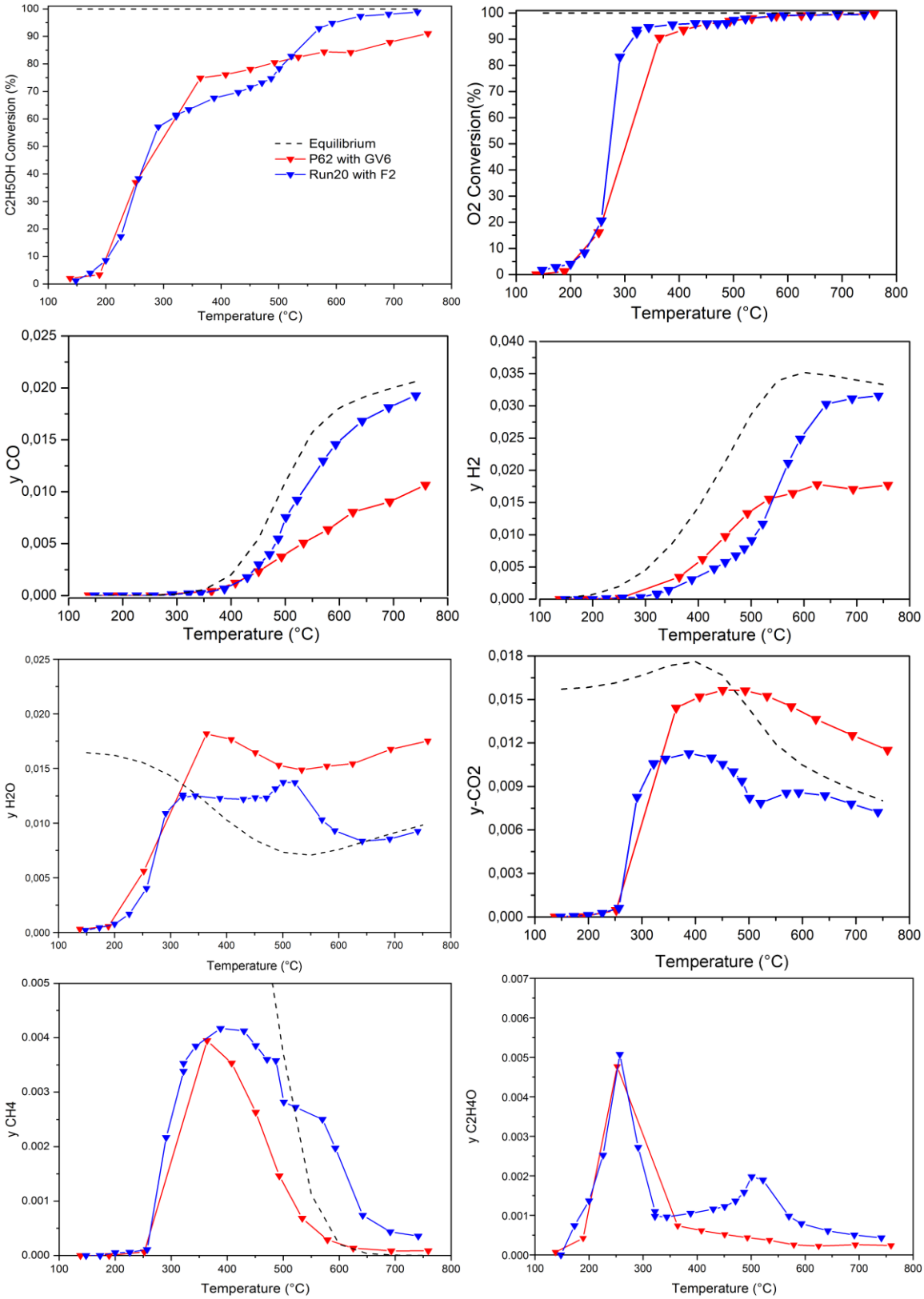

Figure 4.10: Comparison between GV6 and F2 concentration profiles for the CPO of EtOH. Operating conditions: GHSV = 1500000 NL/h/kg EtOH = 1.5% O2/C = 0.56.

In Figure 4.10 a comparison between Mg-aluminate (blue) and alumina (red) is shown. The overall ethanol conversion is higher with F2, showing a sort of plateau between 400 and 600°C, and then increasing again toward nearly complete conversion. The overall production of syngas is much higher than the one of GV6, while CO2 and H2O are produced less. Until 400°C the acetaldehyde profiles are quite similar, but at higher temperature the Mg-alumina present a second peak, at 500°C. The CH_4 production is higher with F2 than the one with α-alumina.

GHSV effect

In this section the effect of the space velocity will be tested on Mg-aluminate catalyst. The GHSV taken into consideration are 5e5, 9e5 and 1.5e6 NL/h/kg, respectively in red, green and blue lines. Dotted lines represent the equilibrium lines obtained through a Chemical equilibrium calculator[56]. Differently from what was expected, the different GHSV, and therefore the different resident times do not affect much the conversion. EtOH conversion lines are quite similar one with each other in the mid temperature range, with a peak a 200°C found only at the lower space velocity. In contrast to what was expected, the higher space velocity case is not the one producing less syngas. This can be because the 9e5 space velocity case was the last one performed, and so the condition in which the catalyst was already heavily subjected to the ethanol stream. Then, similarly to what done for the methane CPO, the kinetic model for EtOH CPO over Rh/α-alumina has been used to simulate the present tests and the results are presented in Figure 4.12. The rate equations and kinetic parameters have been reported in Section 2.4. The comparison between experiments and model predictions suggests that Rh/Mg-aluminate and Rh/alumina, the low temperature conversion of ethanol and oxygen was mainly due to the oxidative dehydrogenation to acetaldehyde and water with comparable rates and temperature/GHSV dependences. At higher temperatures, the model predictions underestimated the observed conversion and indeed the rate of EtOH cracking to methane and CO_x was more pronounced over the Rh/Mg-Al_2O_4. Concerning the syngas production and composition, above 500 °C we observed that the rate of SR was comparable over the two catalysts, but over the present Mg-aluminate catalyst, the rate of WGS (which is responsible for the consecutive conversion of CO into CO_2) was lower than over Rh/alfa-alumina catalyst. Notably, both experiment and model predictions show a limited dependence of EtOH conversion on GHSV at intermediate temperatures (300-500 °C), which suggests that the extent of the deep oxidation reaction (the controlling route in this T-range) is stoichiometrically rather than kinetically controlled. In the same temperature range, small addition formation of acetaldehyde was observed over the Mg-aluminate catalyst, likely associated to a dehydrogenation reaction; this reactivity was not present over Rh/alfa-alumina catalyst.

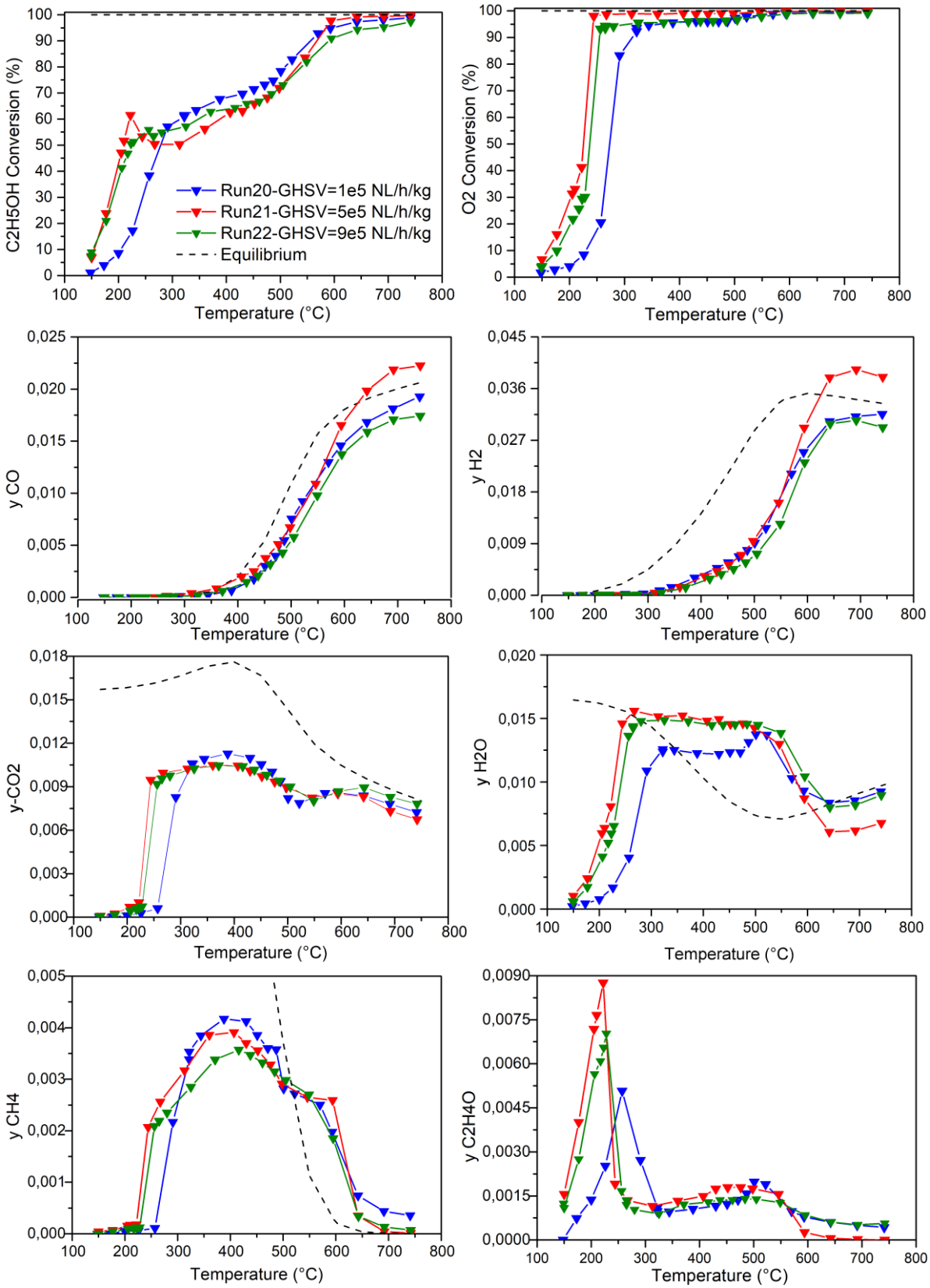

Figure 4.11: Effect of different GHSV in EtOH CPO on Mg-Al_2O_4 catalyst.

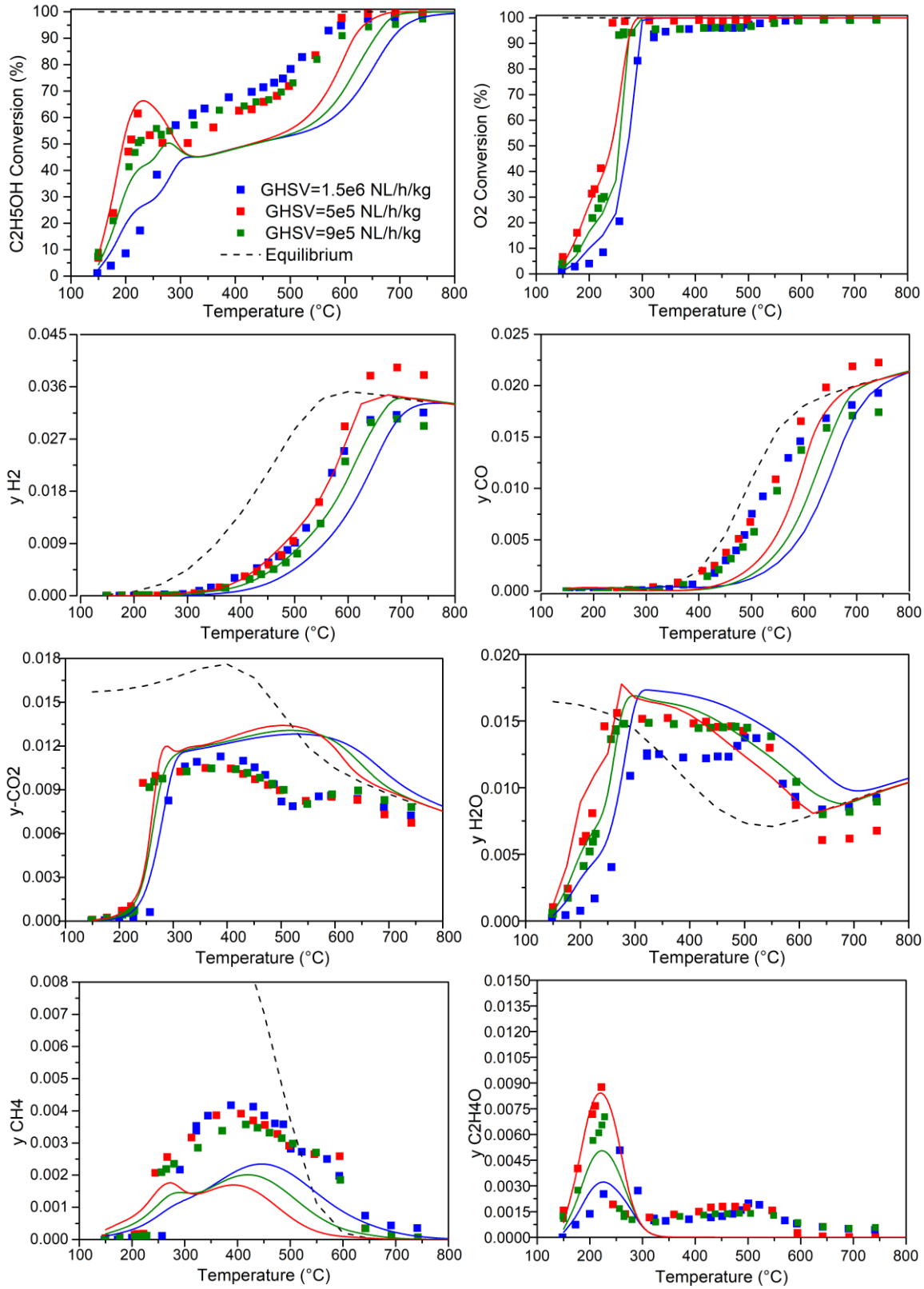

Figure 4.12: Comparison of CPO of EtOH at different GHSV between experimental data and model results.

4.3.2 SR of EtOH

Also in this case, after the experimental campaign with methane, follows the one with ethanol as a fuel.

As done during all this chapter, the Mg-aluminate catalyst has been compared to the commercial alumina one subjected at the same test. This comparison can be seen in Figure 4.13. Green lines represent the Run29 performed with F2 (Mg-Al2O4) and the blue lines the test38 with GV1(α-alumina). Dotted lines represent the equilibrium lines obtained using a chemical equilibrium calculator[56].

Apparently, the Mg-alumina catalyst has a much higher EtOH conversion in the 350-600°C range, producing more acetaldehyde, consistently with the dehydrogenation contribution observed also in the CPO test in the same range of temperature. At higher conversion, the production of syngas remains much higher in the Mg-alumina case. To be noticed, is the higher conversion of ethylene by the GV1 catalyst, with a peak value that is more than double with respect to the one of F2.

The acetaldehyde production can be explained by ethanol dehydrogenation $C_2H_5OH \rightarrow CH_3CHO + H_2$, while the ethylene is the product of dehydration $C_2H_5OH \rightarrow C_2H_4 + H_2O$. This is consistent with the contribution also observed in CPO at 400-600 °C.

Interestingly, Rh/Mg-Al_2O_4 gave rise to less ethylene formation, a known coke precursor.

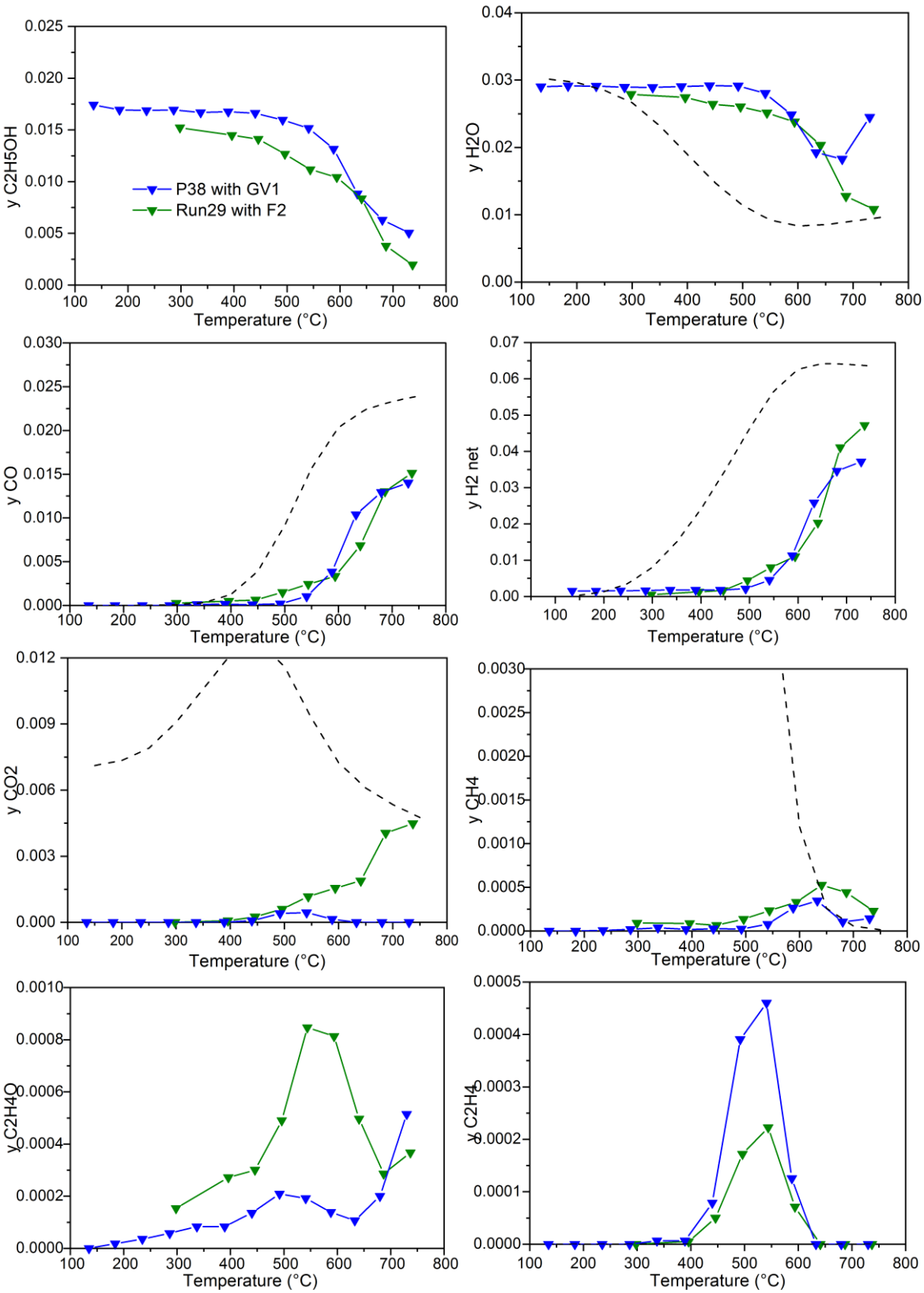

Figure 4.13: SR EtOH comparison of an Mg-alumina catalyst with an alpha-alumina catalyst

Effect of GHSV

To conclude the studied performed on this Mg-aluminate catalyst, the space velocity effect on the steam reforming with ethanol is investigated. Three values of GHSV were tested: 1.5e6, 9e5 and 5e5, and the order of the test was from higher to lower GHSV. As seen in section 4.3, the order of the experiment has to be considered, since the last one is the one that was subjected to a higher total flow of ethanol during the campaign. Results are reported in Figure 4.14. The overall EtOH conversion seems to be in line with the fact that a higher GHSV lead to a lower residence time, and so to a lower conversion. This is coherent also with the syngas production, being the highest in the lowest GHSV case. To be noticed is the much higher production of acetaldehyde in the high space velocity case. The ethylene trends are much different one to each other. The water in the 5e5 NL/h/kg case has a slightly different behavior in the 300-600°C range, with a sort of peak at 350°C. In the overall they are consistent with the expected effect of contact time on the catalytic process; thus, at decreasing GHSV and increasing contact time, the conversion grew as the productivity of all the major products. The CO_2 formation is the result of a WGS consecutive to a SR: $CO + H_2O \rightarrow CO_2 + H_2$. The formation of methane is a consequence of the methanation from CO and hydrogen, $CO + 3H_2 \rightarrow CH_4 + H_2O$. The WGS and the methanation are thermodynamically limited.

Trace amount of methane and ethylene were observed, and they grew at lower temperature with decreasing GHSV. Concerning the acetaldehyde, the peak production in between 400 and 650 °C is largely reduced (as also shown by conversion curves) which suggest a partial evolution of the catalyst properties from the first to the next experiment.

The conditions of the experiments in this section have been used for the simulation of the kinetic EtOH model. The results of this simulation are represented in Figure 4.15. The conversion of EtOH from the model is nearly overlapping the experimental results from 550 °C, while before it is much less. This can be due to the fact that the ethylene production is not considered in the model, while in the experiments the production is quite high. Also the production of methane is really underestimated from the model. The model cannot predict the production of acetaldehyde differently from the methane kinetic model. The production of syngas is comparable between model and experimental data.

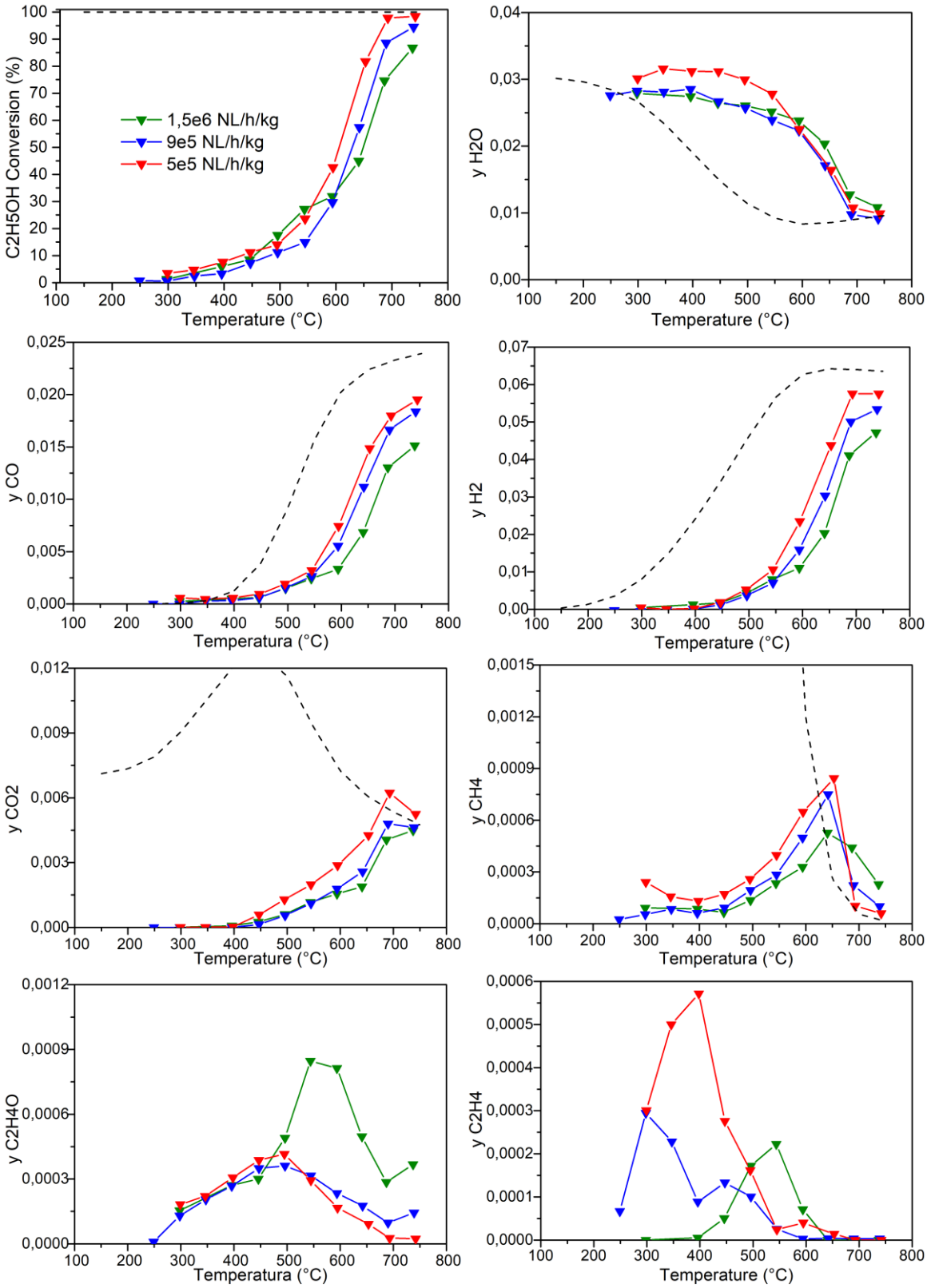

Figure 4.14: Effect of the variation of space velocity in the SR of EtOH with F2

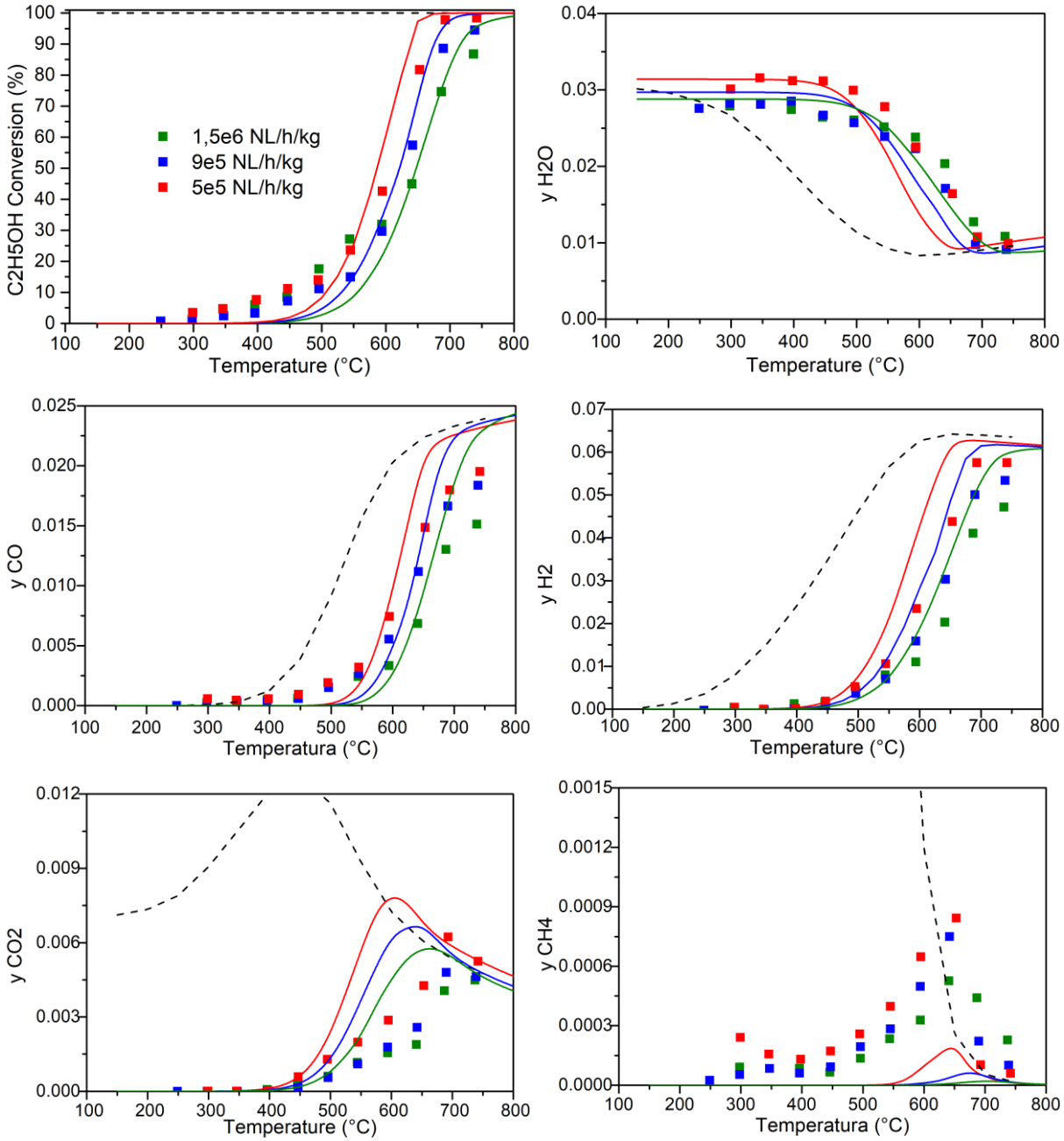

Figure 4.15: Comparison of SR of EtOH at different GHSV between experimental data and model results

We observe a substantially satisfactory comparison. It is however observed that the simulations (thus the performance of the Rh/Al_2O_3 catalyst) reflect a steeper T-dependence. In fact, the model tends to underestimate the conversion below 600 °C and overestimate the observed conversion at the higher temperatures. Secondary

observations involve the role of WGS and methanation. Apparently the rate of WGS is higher on Al_2O_3, while the opposite for the methanation. This might reflect a stronger adsorption of EtOH on Al_2O_3 hindering the reaction at lower temperature.

4.4 Ageing and Temperature programmed oxidation

Similarly, to what has been done in Chapter 3 after adiabatic experiments, temperature programmed oxidations were performed after selected agings over the Mg-aluminate supported catalyst to investigate the tendency to coke deposition of the catalyst. At this scope, a fresh catalyst, F4 have been used for an ageing test, in which the catalytic bed is subjected to the reactant flow for two hours. The aim of this procedure is to study the source of deactivation of the catalyst. The operating temperature is fixed, which in this case is around 200 °C, to be as close as possible to the peak of the acetaldehyde. The ageing test for this catalyst has been done in CPO of ethanol conditions: GHSV = 1500000 NL/h/kg, O_2/C = 0.56, yEtOH = 1.5%. The outlet gaseous products composition and the temperature profiles over catalytic bed are measured by interval of 30 minutes.

Looking at Figure 4.16, each point represents one composition measured every 30 minutes. At around 200 °C ethanol is converted through a mechanism of oxidative dehydrogenation and acetaldehyde is produced. The concentration measurements seem in line with the CPO of EtOH previously done.

The next step consists in the temperature programmed oxidation. In this case, a comparison with a TPO done in previous work with α-alumina[74] has been performed in order to make a qualitative evaluation on the main sources of deactivation. The result of this comparison can be seen in Figure 4.17, normalizing the CO_2 released by the BET area. This TPO consists of subjecting the catalyst, previously used for the ageing, to a stream of air. The GHSV chosen is the same as the one used for the TPO of the α-alumina (25000 NL/h/kg). Starting from ambient temperature, the stream has been heated using the oven until 800 °C, with a heating ramp of 2 °C/min. During all the experiment duration, concentration measurements have been performed. To check the properly performed heating, the temperature has been measured continuously during the experiment.

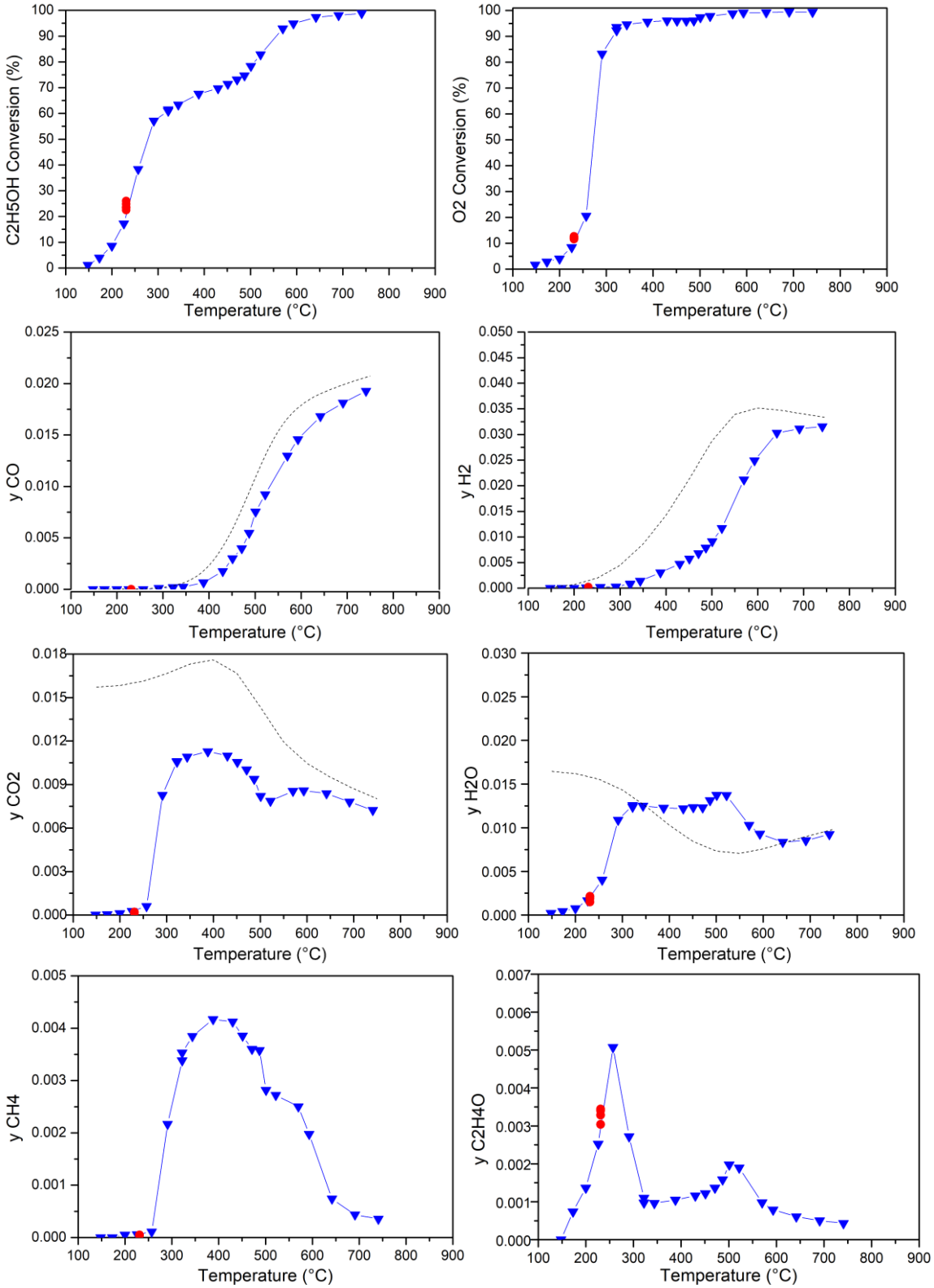

Figure 4.16: EtOH CPO ageing profiles. Dots: ageing test results; continuous line + scatter: Run20 with F2 described in section 4.3.

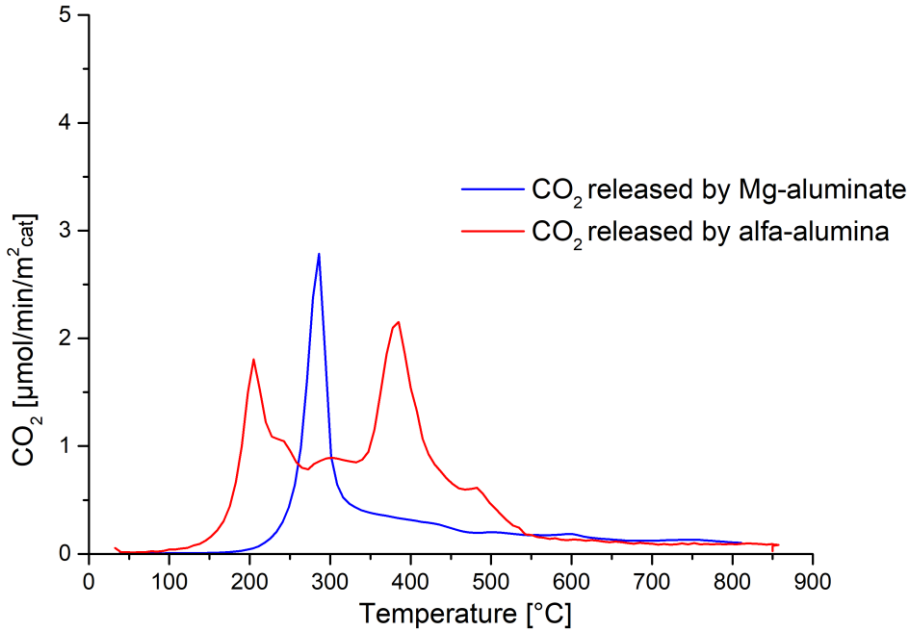

Figure 4.17: CO_2 released by the two catalyst when subjected to TPO.

From the graphs, some consideration can be derived. Multiple peaks can be distinguished for the α-alumina. The two with peaks at around 200 and 300 °C, represents the most reactive species, while the two peak at 400 and 500 °C represents the less reactive ones. The alumina shows different contributions for the release of CO_2, that can be associated to different chemical species (oxygenates at different grade of oxidation and different adsorption strength, but also carbon aggregates of different dimension and more/less close to the Rh site). Differently, in the Mg-aluminate case, there is one major CO2 peak at 300 °C resulting from the oxidation of an expectedly highly reactive surface carbon aggregate, while no high temperature peaks are formed from structured C deposits.

The kinetic study performed during this chapter has highlighted that the Mg-aluminate and the commercial alumina kinetics are quite similar. This is also seen running Mg-alumina data in the α-alumina kinetic model, in which there is a good matching at low temperature range where mass transfer limitations have not a high effect. By looking to the temperature programmed oxidation, the type of carbon deposit on the catalyst surface is different based on the support that have been used, which shows a real role for the support on the deactivation of the catalyst.

Conclusions

$Rh/\alpha\text{-}Al_2O_3$ has been identified in the literature and from previous studies of the research group, as a reference formulation for the autothermal conversion of light hydrocarbons to H_2/CO mixtures. The conversion of the C_1-C_3 hydrocarbon fuels into syngas is a very fast process that approaches thermodynamic equilibrium at few milliseconds contact times; the operation of the autothermal reactor is stable and not hindered by coking phenomena. The use of oxygenated fuels, instead, gives rise to more complex product distribution and the formation of coke precursors, such as ethylene and acetaldehyde, cannot be avoided and negatively affect the stable operation of the reactor. The nature and reactivity of the catalyst can greatly affect the evolution of such undesired reaction intermediates. In recent years, studies have been performed to find a support that could minimize the formation of coke precursors and/or their consecutive condensation to carbon aggregates. In this thesis work, thermodynamic and kinetic investigations were conducted on methane and ethanol CPO and SR over 2% Rh/Al_2O_3-La, 2% $Rh/Mg\text{-}Al_2O_4$, and 2% $Rh/\alpha\text{-}Al_2O_3$ catalysts. Experiments have been carried out in a lab-scale adiabatic reactor for process verification, and in an isothermal microreactor for deepening the kinetic knowledge. Research focused on the characterization of the performance of the different commercial supports to investigate their effect on the production of H_2 and on the stability of the process.

The first part of the project extended the activity of a previous work and consisted of the preparation of $Rh/La\text{-}\alpha\text{-}Al_2O_3$ coated on a cordierite honeycomb monolith, using a percolate-spin-coating technique. The monolith was tested in the adiabatic reactor and CPO tests were performed using a mixture of water (8% wt.) and ethanol (92% wt.), with an oxygen ratio of 0.65 and a dilution ratio of 0.5. The adiabatic reactor is equipped with the spatially resolved sampling technique, that allows the acquisition of axial concentration and temperature profiles. The results of this campaign have been compared to those obtained in the same conditions using a different supported catalyst (magnesium-aluminate). The temperature measurements over the two catalysts showed that the nature of the support has a minor effect on the thermal behavior of the reactor, since in both cases the profiles obtained were similar, with a hotspot located at the monolith entrance, with similar and moderate peak intensity. Concentration results show that, for both catalysts, the overall reaction process was practically complete within 10 mm, which can be associated to the fast chemical processes and the relatively thick washcoat layer that the spin coating technique guarantees. During time on stream, however, evidence of a deactivation process was

collected with progressive increase of the hotspot temperature during periodically repeated CH_4-CPO tests. The catalytic monolith was then unloaded, cut and exposed to temperature programmed oxidation tests, that allow to characterize quantitatively and qualitatively the carbonaceous structures formed on catalyst during the experiments. It was found that the total amount of carbon deposited on the La-doped-alumina catalyst was higher than the one on the magnesium-aluminate one. From this and previous results, we could thus identify Mg-Al_2O_4 as the best commercial support for the stable operation of the Rh-catalysts in the ethanol CPO.

In the second part of the work, we then addressed a deeper kinetic investigation of the ethanol conversion processes over the Rh/$MgAl_2O_4$ catalyst. The annular microreactor was applied at this scope. This reactor allows to work at high gas hourly space velocity (GHSV) under quasi-isothermal conditions. With this configuration, the impacts of both the diffusional limitations and thermodynamic constraints are reduced. CPO and SR of methane and ethanol were investigated. Different conditions have been considered varying the GHSV and the oxygen to carbon ratio of the reaction. The experimental campaign has been compared qualitatively with the results of analogue investigations in previous thesis works, where the α-alumina had been used as a reference.

Besides, a more quantitative comparison between Rh/Mg-Al_2O_4 and Rh/α-Al_2O_3 catalysts was obtained by comparing the present results with the predictions of a model developed in previous thesis to describe the processes on Rh/α-Al_2O_3. No major difference was found between the two catalysts, especially when looking at the major reactions (oxidations, steam reforming). However, the kinetic investigation in microreactor confirmed the lower tendency of Mg-Al_2O_4 to strongly adsorb ethanol and to promote the formation of surface C species.

Suitable morphological properties (surface area, Rh dispersion) and low acidity are apparently the favorable features that provide superior performances to this support, especially the control of coking phenomena.

Bibliography

[1] J. A. Moulijn, M. Makkee, and A. E. Van Diepen, "Chemical Process Technology."

[2] T. Rostrup-Nielsen, "Manufacture of hydrogen," *Catal. Today*, vol. 106, no. 1–4, pp. 293–296, Oct. 2005, doi: 10.1016/J.CATTOD.2005.07.149.

[3] IEA, "Global hydrogen demand by sector in the Net Zero Scenario, 2020-2030," Paris. [Online]. Available: https://www.iea.org/data-and-statistics/charts/global-hydrogen-demand-by-sector-in-the-net-zero-scenario-2020-2030.

[4] M. Plazas-González, C. A. Guerrero-Fajardo, and J. R. Sodré, "Modelling and simulation of hydrotreating of palm oil components to obtain green diesel," *J. Clean. Prod.*, vol. 184, pp. 301–308, May 2018, doi: 10.1016/j.jclepro.2018.02.275.

[5] L. D. Schmidt, E. J. Klein, C. A. Leclerc, J. J. Krummenacher, and K. N. West, "Syngas in millisecond reactors: higher alkanes and fast lightoff," *Chem. Eng. Sci.*, vol. 58, no. 3–6, pp. 1037–1041, Feb. 2003, doi: 10.1016/S0009-2509(02)00645-0.

[6] S. M. M. E. Ayad, C. R. P. Belchior, G. L. R. da Silva, R. S. Lucena, E. S. Carreira, and P. E. V. de Miranda, "Analysis of performance parameters of an ethanol fueled spark ignition engine operating with hydrogen enrichment," *Int. J. Hydrogen Energy*, vol. 45, no. 8, pp. 5588–5606, Feb. 2020, doi: 10.1016/J.IJHYDENE.2019.05.151.

[7] J. D. Holladay, J. Hu, D. L. King, and Y. Wang, "An overview of hydrogen production technologies," *Catal. Today*, vol. 139, no. 4, pp. 244–260, Jan. 2009, doi: 10.1016/J.CATTOD.2008.08.039.

[8] A. Mostafa and Y. Uysal, "Catalytic Partial Oxidation of ethanol on Rh coated monoliths : in situ measurements of temperature and concentration profiles," 2019, [Online]. Available: https://www.politesi.polimi.it/handle/10589/148831.

[9] H. Nourbakhsh, J. Rahbar Shahrouzi, H. Ebrahimi, A. Zamaniyan, and M. R. Jafari Nasr, "Experimental and numerical study of syngas production during premixed and ultra-rich partial oxidation of methane in a porous reactor," *Int. J. Hydrogen Energy*, vol. 44, no. 60, pp. 31757–31771, Dec. 2019, doi: 10.1016/J.IJHYDENE.2019.10.084.

[10] A. P. E. York, T. Xiao, and M. L. H. Green, "Brief overview of the partial oxidation of methane to synthesis gas," *Top. Catal.*, vol. 22, no. 3–4, pp. 345–358, Apr. 2003, doi: 10.1023/A:1023552709642.

[11] G. Iaquaniello *et al.*, "Natural Gas Catalytic Partial Oxidation: A Way to Syngas and Bulk Chemicals Production," in *Natural Gas - Extraction to End Use*, InTech, 2012.

[12] A. Donazzi, A. Beretta, G. Groppi, and P. Forzatti, "Catalytic partial oxidation of methane over a 4% Rh/α-Al2O3 catalyst: Part I: Kinetic study in annular reactor," *J. Catal.*, vol. 255, no. 2, pp. 241–258, Apr. 2008, doi: 10.1016/J.JCAT.2008.02.009.

[13] A. Donazzi, D. Livio, A. Beretta, G. Groppi, and P. Forzatti, "Surface temperature profiles in CH4 CPO over honeycomb supported Rh catalyst probed with in situ optical pyrometer," *Appl. Catal. A Gen.*, vol. 402, no. 1–2, pp. 41–49, Jul. 2011, doi: 10.1016/J.APCATA.2011.05.022.

[14] A. Mostafa, Y. Uysal, R. B. S. Junior, A. Beretta, and G. Groppi, "Catalytic partial oxidation of ethanol over Rh-coated monoliths investigated by the axially resolved sampling technique: Effect of H2O co-feed," *Catal. Today*, vol. 367, pp. 71–82, May 2021, doi: 10.1016/J.CATTOD.2020.09.030.

[15] H. Liander, "The utilisation of natural gases for the ammonia process," *Trans. Faraday Soc.*, vol. 25, p. 462, 1929, doi: 10.1039/tf9292500462.

[16] C. Padovani and P. Franchetti, "Incomplete oxidation of methane with oxygen and air." .

[17] M. Prettre, C. Eichner, and M. Perrin, "The catalytic oxidation of methane to carbon monoxide and hydrogen," *Trans. Faraday Soc.*, vol. 42, p. 335b, 1946, doi: 10.1039/tf946420335b.

[18] D. A. Hickman and L. D. Schmidt, "Synthesis gas formation by direct oxidation of methane over Pt monoliths," *J. Catal.*, vol. 138, no. 1, pp. 267–282, Nov. 1992, doi: 10.1016/0021-9517(92)90022-A.

[19] D. A. Hickman, E. A. Haupfear, and L. D. Schmidt, "Synthesis gas formation by direct oxidation of methane over Rh monoliths," *Catal. Letters*, vol. 17, no. 3–4, pp. 223–237, 1993, doi: 10.1007/BF00766145.

[20] S. S. Bharadwaj and L. D. Schmidt, "Catalytic partial oxidation of natural gas to syngas," *Fuel Process. Technol.*, vol. 42, no. 2–3, pp. 109–127, Apr. 1995, doi: 10.1016/0378-3820(94)00098-E.

[21] M. Bizzi, G. Saracco, R. Schwiedernoch, and O. Deutschmann, "Modeling the

partial oxidation of methane in a fixed bed with detailed chemistry," *AIChE J.*, vol. 50, no. 6, pp. 1289–1299, Jun. 2004, doi: 10.1002/aic.10118.

[22] A. Donazzi, A. Beretta, G. Groppi, and P. Forzatti, "Catalytic partial oxidation of methane over a 4% Rh/α-Al2O3 catalyst Part II: Role of CO2 reforming," *J. Catal.*, vol. 255, no. 2, pp. 259–268, Apr. 2008, doi: 10.1016/J.JCAT.2008.02.010.

[23] B. C. Michael, A. Donazzi, and L. D. Schmidt, "Effects of H2O and CO2 addition in catalytic partial oxidation of methane on Rh," *J. Catal.*, vol. 265, pp. 117–129, 2009.

[24] L. V. Mattos and F. B. Noronha, "Hydrogen production for fuel cell applications by ethanol partial oxidation on Pt/CeO2 catalysts: The effect of the reaction conditions and reaction mechanism," *J. Catal.*, vol. 233, no. 2, pp. 453–463, 2005, doi: 10.1016/j.jcat.2005.04.022.

[25] N. M. Marinov, "A detailed chemical kinetic model for high temperature ethanol oxidation," *Int. J. Chem. Kinet.*, vol. 31, no. 3, pp. 183–220, 1999, doi: 10.1002/(SICI)1097-4601(1999)31:3<183::AID-KIN3>3.0.CO;2-X.

[26] N. Hebben, C. Diehm, and O. Deutschmann, "Catalytic partial oxidation of ethanol on alumina-supported rhodium catalysts: An experimental study," *Appl. Catal. A Gen.*, vol. 388, no. 1–2, pp. 225–231, Nov. 2010, doi: 10.1016/J.APCATA.2010.08.055.

[27] P. K. Cheekatamarla and C. M. Finnerty, "Synthesis gas production via catalytic partial oxidation reforming of liquid fuels," *Int. J. Hydrogen Energy*, vol. 33, no. 19, pp. 5012–5019, Oct. 2008, doi: 10.1016/J.IJHYDENE.2008.07.003.

[28] C. Diehm, T. Kaltschmitt, and O. Deutschmann, "Hydrogen production by partial oxidation of ethanol/gasoline blends over Rh/Al2O3," *Catal. Today*, vol. 197, no. 1, pp. 90–100, Dec. 2012, doi: 10.1016/J.CATTOD.2012.06.032.

[29] D. K. Liguras, K. Goundani, and X. E. Verykios, "Production of hydrogen for fuel cells by catalytic partial oxidation of ethanol over structured Ru catalysts," *Int. J. Hydrogen Energy*, vol. 29, no. 4, pp. 419–427, Mar. 2004, doi: 10.1016/S0360-3199(03)00210-6.

[30] H. Chen *et al.*, "Hydrogen production via autothermal reforming of ethanol over noble metal catalysts supported on oxides," *J. Nat. Gas Chem.*, vol. 18, no. 2, pp. 191–198, Jun. 2009, doi: 10.1016/S1003-9953(08)60106-1.

[31] C. P. Rodrigues, V. T. da Silva, and M. Schmal, "Partial oxidation of ethanol on Cu/Alumina/cordierite monolith," *Catal. Commun.*, vol. 10, no. 13, pp. 1697–1701, Jul. 2009, doi: 10.1016/J.CATCOM.2009.05.010.

[32] C. P. Rodrigues, V. T. da Silva, and M. Schmal, "Partial oxidation of ethanol over cobalt oxide based cordierite monolith catalyst," *Appl. Catal. B Environ.*, vol. 96, no. 1–2, pp. 1–9, Apr. 2010, doi: 10.1016/J.APCATB.2010.01.027.

[33] J. R. Salge, G. A. Deluga, and L. D. Schmidt, "Catalytic partial oxidation of ethanol over noble metal catalysts," *J. Catal.*, vol. 235, no. 1, pp. 69–78, Oct. 2005, doi: 10.1016/J.JCAT.2005.07.021.

[34] D. Pagani *et al.*, "A kinetic analysis of the partial oxidation of C3H8 over a 2% Rh/Al2O3 catalyst in annular microreactor," *Catal. Today*, vol. 197, no. 1, pp. 265–280, Dec. 2012, doi: 10.1016/J.CATTOD.2012.09.004.

[35] D. Pagani *et al.*, "A Kinetic Investigation of the Catalytic Partial Oxidation of Propylene over a Rh/Al 2 O 3 Catalyst," *Ind. Eng. Chem. Res.*, vol. 53, no. 5, pp. 1804–1815, Feb. 2014, doi: 10.1021/ie4025352.

[36] R. Batista da Silva *et al.*, "Chemical pathways in the partial oxidation and steam reforming of acetic acid over a Rh-Al2O3 catalyst," *Catal. Today*, vol. 289, pp. 162–172, Jul. 2017, doi: 10.1016/J.CATTOD.2016.08.018.

[37] D. Livio, C. Diehm, A. Donazzi, A. Beretta, and O. Deutschmann, "Catalytic partial oxidation of ethanol over Rh/Al2O3: Spatially resolved temperature and concentration profiles," *Appl. Catal. A Gen.*, vol. 467, pp. 530–541, Oct. 2013, doi: 10.1016/J.APCATA.2013.07.054.

[38] A. Carrera, M. Pelucchi, A. Stagni, A. Beretta, and G. Groppi, "Catalytic partial oxidation of n-octane and iso-octane: Experimental and modeling results," *Int. J. Hydrogen Energy*, vol. 42, no. 39, pp. 24675–24688, Sep. 2017, doi: 10.1016/J.IJHYDENE.2017.08.020.

[39] A. Beretta *et al.*, "Optimal design of a CH4 CPO-reformer with honeycomb catalyst: Combined effect of catalyst load and channel size on the surface temperature profile," *Catal. Today*, vol. 171, no. 1, pp. 79–83, Aug. 2011, doi: 10.1016/J.CATTOD.2011.03.081.

[40] A. Donazzi, M. Maestri, A. Beretta, G. Groppi, E. Tronconi, and P. Forzatti, "Microkinetic analysis of CH4 CPO tests with CO2-diluted feed streams," *Appl. Catal. A Gen.*, vol. 391, no. 1–2, pp. 350–359, Jan. 2011, doi: 10.1016/J.APCATA.2010.06.030.

[41] A. Donazzi, D. Livio, C. Diehm, A. Beretta, G. Groppi, and P. Forzatti, "Effect of pressure in the autothermal catalytic partial oxidation of CH4 and C3H8: Spatially resolved temperature and composition profiles," *Appl. Catal. A Gen.*, vol. 469, pp. 52–64, Jan. 2014, doi: 10.1016/J.APCATA.2013.09.054.

[42] A. Carrera, A. Beretta, and G. Groppi, "Catalytic Partial Oxidation of Iso-octane

over Rh/α-Al 2 O 3 in an Adiabatic Reactor: An Experimental and Modeling Study," *Ind. Eng. Chem. Res.*, vol. 56, no. 17, pp. 4911–4919, May 2017, doi: 10.1021/acs.iecr.7b00255.

[43] R. Batista, A. Carrera, A. Beretta, and G. Groppi, "Thermal Deactivation of Rh/α-Al2O3 in the Catalytic Partial Oxidation of Iso-Octane: Effect of Flow Rate," *Catalysts*, vol. 9, no. 6, p. 532, Jun. 2019, doi: 10.3390/catal9060532.

[44] M. Bressan, "Catalytic partial oxidation of ethanol on Rh coated monoliths: advanced catalyst formulation and coating techniques," 2021.

[45] I. Tavazzi, A. Beretta, G. Groppi, M. Maestri, E. Tronconi, and P. Forzatti, "Experimental and modeling analysis of the effect of catalyst aging on the performance of a short contact time adiabatic CH4-CPO reactor," *Catal. Today*, vol. 129, no. 3–4, pp. 372–379, Dec. 2007, doi: 10.1016/J.CATTOD.2007.06.085.

[46] A. Le Valant, F. Can, N. Bion, D. Duprez, and F. Epron, "Hydrogen production from raw bioethanol steam reforming: Optimization of catalyst composition with improved stability against various impurities," *Int. J. Hydrogen Energy*, vol. 35, no. 10, pp. 5015–5020, May 2010, doi: 10.1016/J.IJHYDENE.2009.09.008.

[47] F. Auprêtre, C. Descorme, and D. Duprez, "Bio-ethanol catalytic steam reforming over supported metal catalysts," *Catal. Commun.*, vol. 3, no. 6, pp. 263–267, Jun. 2002, doi: 10.1016/S1566-7367(02)00118-8.

[48] A. S. Bodke, S. S. Bharadwaj, and L. D. Schmidt, "The Effect of Ceramic Supports on Partial Oxidation of Hydrocarbons over Noble Metal Coated Monoliths," *J. Catal.*, vol. 179, no. 1, pp. 138–149, Oct. 1998, doi: 10.1006/JCAT.1998.2224.

[49] F. Aupretre, C. Descorme, D. Duprez, D. Casanave, and D. Uzio, "Ethanol steam reforming over MgxNi1−xAl2O3 spinel oxide-supported Rh catalysts," *J. Catal.*, vol. 233, no. 2, pp. 464–477, Jul. 2005, doi: 10.1016/J.JCAT.2005.05.007.

[50] C. Graschinsky *et al.*, "Ethanol Steam Reforming over Rh(1%)MgAl 2 O 4 /Al 2 O 3 : A Kinetic Study," *Ind. Eng. Chem. Res.*, vol. 49, no. 24, pp. 12383–12389, Dec. 2010, doi: 10.1021/ie101284k.

[51] J. G. Li, T. Ikegami, J. H. Lee, T. Mori, and Y. Yajima, "A wet-chemical process yielding reactive magnesium aluminate spinel (MgAl2O4) powder," *Ceram. Int.*, vol. 27, no. 4, pp. 481–489, Jan. 2001, doi: 10.1016/S0272-8842(00)00107-3.

[52] M. Argyle and C. Bartholomew, "Heterogeneous Catalyst Deactivation and Regeneration: A Review," *Catalysts*, vol. 5, no. 1, pp. 145–269, Feb. 2015, doi: 10.3390/catal5010145.

[53] A. Carrera, "Catalytic Partial Oxidation of Liquid Fuels: Experimental and

Modeling Analysis of a Lab-Scale Adiabatic Reformer," 2016.

[54] R. Horn, N. J. Degenstein, K. A. Williams, and L. D. Schmidt, "Spatial and temporal profiles in millisecond partial oxidation processes," *Catal. Letters*, vol. 110, no. 3–4, pp. 169–178, Sep. 2006, doi: 10.1007/s10562-006-0117-8.

[55] R. H. Perry, *Perry's Chemical Engineers' Handbook*, 7th ed. McGraw-Hill, 1999.

[56] "Chemical Equilibrium Calculation." .

[57] E. Hochkoeppler and D. Braglia, "Kinetic Study of Partial Oxidation and Steam Reforming of ethanol over Rh/Al2O3 and Pt/Al2O3 catalysts," Politecnico di Milano, 2018.

[58] D. Pierro and A. Sommariva, "OSSIDAZIONE PARZIALE CATALITICA DI ISOOTTANO, PROPILENE E ETANOLO SU CATALIZZATORI Rh/α-Al2O3: influenza dei gruppi funzionali sulla cinetica di reazione," Politecnico di Milano.

[59] L. Rosbuco, "Studio cinetico del processo di ossidazione parziale catalitica di idrocarburi C1-C8 e ossigenati su catalizzatori Rh/Al2O3," Politecnico di Milano, 2017.

[60] A. Montebelli *et al.*, "Methods for the catalytic activation of metallic structured substrates," *Catal. Sci. Technol.*, vol. 4, no. 9, pp. 2846–2870, 2014, doi: 10.1039/c4cy00179f.

[61] C. Cristiani, C. G. Visconti, E. Finocchio, P. G. Stampino, and P. Forzatti, "Towards the rationalization of the washcoating process conditions," *Catal. Today*, vol. 147, no. SUPPL., pp. 24–29, 2009, doi: 10.1016/j.cattod.2009.07.031.

[62] R. Balzarotti, C. Cristiani, and L. F. Francis, "Combined dip-coating/spin-coating depositions on ceramic honeycomb monoliths for structured catalysts preparation," *Catal. Today*, vol. 334, pp. 90–95, Aug. 2019, doi: 10.1016/J.CATTOD.2019.01.037.

[63] R. Balzarotti, C. Cristiani, S. Latorrata, and A. Migliavacca, "Washcoating of low surface area cerium oxide on complex geometry substrates," *Part. Sci. Technol.*, vol. 34, no. 2, pp. 184–193, Mar. 2016, doi: 10.1080/02726351.2015.1058872.

[64] M. Ambrosetti, R. Balzarotti, C. Cristiani, G. Groppi, and E. Tronconi, "The Influence of the Washcoat Deposition Process on High Pore Density Open Cell Foams Activation for CO Catalytic Combustion," doi: 10.3390/catal8110510.

[65] M. Valentini, G. Groppi, C. Cristiani, M. Levi, E. Tronconi, and P. Forzatti, "The deposition of γ-Al2O3layers on ceramic and metallic supports for the preparation of structured catalysts," *Catal. Today*, vol. 69, no. 1–4, pp. 307–314, 2001, doi: 10.1016/S0920-5861(01)00383-2.

[66] D. Pagani, "Catalytic Partial Oxidation of light and liquid hydrocarbons: experimental and kinetic study on Rh based catalyst."

[67] A. Beretta, P. Baiardi, D. Prina, and P. Forzatti, "Analysis of a catalytic annular reactor for very short contact times," *Chem. Eng. Sci.*, vol. 54, no. 6, pp. 765–773, 1999, doi: 10.1016/S0009-2509(98)00261-9.

[68] A. Beretta, P. Baiardi, D. Prina, and P. Forzatti, *Development of a catalytic reactor with annular configuration*, vol. 118. Elsevier Masson SAS, 1998.

[69] R. C. Reid, J. M. Prausnitz, and B. E. Poling, *The properties of Gases and Liquids*. New York, 1987.

[70] E. Tronconi and P. Forzatti, "Adequacy of lumped parameter models for SCR reactors with monolith structure," *AIChE J.*, vol. 38, no. 2, pp. 201–210, Feb. 1992, doi: 10.1002/aic.690380205.

[71] R. D. Hawthorne, "Afterburner catalysts-effects of heats and mass transfer between gas and catalyst surface," *AIChE J. Symp Ser*, vol. 70, pp. 428–438, 1974.

[72] R. K. Shah and A. L. London, *Laminar Flow Forced Convection in Ducts*. Elsevier, 1978.

[73] N. Wakao and J. M. Smith, "Diffusion in catalyst pellets," *Chem. Eng. Sci.*, vol. 17, no. 11, pp. 825–834, Nov. 1962, doi: 10.1016/0009-2509(62)87015-8.

[74] A. G. Bayram and V. Piazza, "Syngas Production from Ethanol and Formic Acid over Rh / Al 2 O 3 : a Kinetic Study in Annular Reactor," 2019, [Online]. Available: https://www.politesi.polimi.it/bitstream/10589/150149/3/2019_10_Bayram_Piazza.pdf.

[75] W. Wang and Y. Wang, "Thermodynamic analysis of hydrogen production via partial oxidation of ethanol," vol. 33, pp. 5035–5044, 2008, doi: 10.1016/j.ijhydene.2008.07.086.

[76] N. Mazzoleni and V. Spadazzeschi, "Studio cinetico del processo di ossidazione parziale di CH4 per la produzione di H2: catalizzatori Rh/α-Al2O3 ad alto carico," Politecnico di Milano, 2006.

List of Figures

List of Tables

List of Symbols

m_{Rh} [g] = mass of rhodium

m_{sup} [g] = mass of the support

$y_{Rh}[\frac{g_{Rh}}{g_{cat}}]$ = catalyst rhodium loading

$\omega_{Rh,sol}[\frac{g_{Rh}}{g_{sol}}]$ = rhodium mass fraction in the solution

$\dot{V}_{porous-specific}\ [\frac{ml}{g}]$ = specific pore volume

V_{pores}[ml] = total pore volume

$V_{i,liq}$ [ml_{liq}/min] = volumetric flow rate of liquid fuel delivered by the pump

$\dot{n}_{i,gas}$ [Nl_{gas}/min] = molar flow rate of liquid fuel delivered by the pump

MW_i [g/mol] = fuel molecular weight

k_{norm} [Nl/mol] $= \frac{R[l\cdot atm/(mol\cdot K)]\cdot T_{norm}[K]}{p\,[atm]} = 22.414\ \frac{Nl}{mol}$ = conversion coefficient

$T_{norm}[K] = 273.15$

$\rho_i[g/ml]$ = fuel density

$P[-]$ = purity of the fuel

$V(T)[V]$ = voltage difference

$\varepsilon_s[-]$ = surface emissivity

$K\ [\frac{V}{K}]$ = parameter that depends on the type of pyrometer used

$T\ [K]$ = temperature

$N\ [-] = \frac{C}{\lambda \cdot T}$

$C\ [\mu m\ \cdot K] = 1.44\ \cdot 10^4$

$\lambda[\mu m]$ = radiation wavelength

$\Delta T\ [K]$ = temperature difference between the junctions

$V\ [V]$ = electric potential

$a_n \left[\frac{K}{V_n}\right]$ = parameter depending on the materials used

N [−] = parameter depending on the desired accuracy

α_i[−] = response factor

$\dot{n}_i, \dot{n}_{N_2} [\frac{Nl}{min}]$ = molar flow of the i-species and nitrogen, respectively

$A_i, A_{N_2} [\mu V \cdot s]$ = areas under the peak of the i-species and nitrogen, respectively

F_i $[\frac{mol}{min}]$ = molar flow rate of the i-species

y_i[−] = molar fraction of the i-species

X_i[−] = conversion of the i-species

nC_i[−] = number of carbon atoms of the i-species

nH_i[−] = number of hydrogen atoms of the i-species

nO_i[−] = number of the oxygen atoms of the i-species

$\mathrm{F_{C,converted}} [\frac{\mathrm{mol}}{\mathrm{min}}]$= molar flow of carbon converted

$\mathrm{F_{H,converted}} [\frac{\mathrm{mol}}{\mathrm{min}}]$= molar flow of hydrogen converted

$\mathrm{F_{O,converted}} [\frac{\mathrm{mol}}{\mathrm{min}}]$= molar flow of oxygen converted

$\sigma_{c,i}$ [−] = carbon selectivity towards product species i

Φ_{O_2} [−] = Thiele modules for oxygen

η_{O_2}[−] = efficiency factor of oxygen

α[−] = reactor themal efficiency

Sh [−] = Sherwood number

Pe [−] = Peclèt number

Acknowledgements

I would like to thank, first of all, to professors Alessandra Beretta and Gianpiero Groppi for their support and for the knowledge transmitted during the experience in the lab.

A huge thanks to my SUPER-supervisors, Dudu and Veronica, that help me through all the thesis work. Thank to them I was able to enjoy completely this year, sure that for any question they would have been available.

Thanks to everybody in the lab and in my study group, with whom I shared this journey". The moments we spent together made this experience at Polimi more enjoyable.

Infinite thanks to my family, for allowing me to complete my studies and for always being supportive. Thanks to my girlfriend Alessandra, for cheering me on and supporting me right from the start of my studies.

Thanks to my best friends Steve, Depa and Corb, who have always believed in my abilities and always supported me. I would also like to thank all my friend in the group "Chicos en Tijuana", who made these years easier.

Last but not least, I want to thank my dog Naoki, my number one fan, always ready to comfort me when I was struggling. You're the best dog in the world.